Geometry Driven Particle Correlations in Small Collision Systems

By

Sylvia Irene Morrow

Dissertation

Submitted to the Faculty of the

Graduate School of Vanderbilt University

in partial fulfillment of the requirements

for the degree of

DOCTOR OF PHILOSOPHY

in

Physics

September 30, 2019

Nashville, Tennessee

Approved:

Julia Velkovska, Ph.D.

Senta Victoria Greene, Ph.D.

Alfredo Gurrola, Ph.D.

William Holmes, Ph.D.

Sait Umar, Ph.D.

ACKNOWLEDGMENTS

I would like to acknowledge the many people who have mentored and supported me through this journey. I am grateful to Julia Velkovska who has been an excellent advisor. Thanks to the professors, postdocs, and students in the Relativistic Heavy-Ion research group at Vanderbilt; in particular, thanks to Vicki Greene, Qiao Xu, and Weizhuang Peng. I'd also like to acknowledge the members of the PHENIX collaboration who have helped me grow as a scientist, including Jamie Nagle, Darren McGlinchey, and Ron Belmont.

Thanks to my family who have been there for me every step of the way.

TABLE OF CONTENTS

LIST OF TABLES

LIST OF FIGURES

Math Symbols

b – impact parameter
ε_n – n^{th} order eccentricity, Equation (2.1)
η – pseudorapidity, Equation (3.3)
ψ_n – event plane angle, Equation (4.2)
Ψ_P – nucleon participant plane angle
Ψ_R – reaction plane angle
p_T – transverse momentum, Equation (3.2)
$\sqrt{s_{NN}}$ – center-of-mass energy per nucleon pair
v_n – coefficients to Fourier decomposition of $dN/d\phi$, Equation (4.4)

Experiment

BBC – beam-beam counter detector
BNL – Brookhaven National Laboratory
CNT – central arm detector
FVTX – forward vertex detector
LHC – Large Hadron Collider
RHIC – Relativistic Heavy Ion Collider
PHENIX – an experiment at RHIC
STAR – an experiment at RHIC

Model Names

AMPT– A Multi-Phase Transport model
MC-Glauber – Monte Carlo Glauber
MSTV – a color-glass condensate model (eponymous[1])
SONIC – Super hybrid mOdel simulatioN for relativistic heavy-Ion Collisions
superSONIC – event-by-event generalization of SONIC
QCD – quantum chromodynamics
iEBE-VISHNU – an event-by-event hybrid hydrodynamic model

[1] Mace, Skokov, Tribedy, Venugopalan

Chapter 1

Introduction

When subject to extreme temperature and pressure, hadronic matter like protons and neutrons can melt into its constituent particles, quarks and gluons. The resultant state of matter, quark-gluon plasma, is governed by the strong interaction. A fraction of a second after the Big Bang, the entire universe was comprised of quark-gluon plasma, but this state was short lived as the universe cooled and expanded out from this concentrated form. Relativistic heavy-ion collisions have been nicknamed "mini Big Bangs" because the hot matter created in the collision evolves through a similar process.

Experiments at the Relativistic Heavy Ion Collider (RHIC) at Brookhaven National Laboratory (BNL) conducted measurements that discovered quark-gluon plasma which behaves like the most perfect liquid in nature. The collective motion of the system was measured to correspond to very low specific viscosity. It continues to be a primary experimental objective at both RHIC and the Large Hadron Collider (LHC) to characterize and understand the properties of quark-gluon plasma in detail.

A recent area of interest in the field, and the focus of this dissertation, is a class of collision experiments referred to as small systems, because one or both of the ions being collided has a small number of nucleons. The original motivation for small-system collisions was to understand nuclear effects which occurred independent of the presence of a hot quark-gluon plasma system. In large systems, hot and cold nuclear matter effects are comingled, so a measurement of just the cold nuclear matter effects was needed to help isolate effects that originate in the quark-gluon plasma and constrain models of the system. When performing the first small-system collision experiments, it was anticipated that any particle correlations measured in these systems could be entirely attributed to cold nuclear matter effects which would directly correspond (with some scaling) to cold nuclear matter

effects in large systems. This reasoning came from the assumption that even if the nuclear melting point was surpassed, the time spent in this state would be prohibitively short such that the transition into quark-gluon plasma would not occur. However, particle correlation results from both RHIC and the LHC have shown that these systems have some mechanism for driving collective behavior in a way that is reminiscent of collectivity from quark-gluon plasma in large systems. The mounting evidence that quark-gluon plasma is formed in small systems has motivated a deeper exploration of the size limits of quark-gluon plasma and has necessitated the development of a theoretical picture of how such fast melting can occur and how such a small amount of matter can exhibit fluid properties.

Two sets of small collision system experiments were conducted at RHIC to investigate this question. A beam energy scan was conducted using d+Au collisions across an order of magnitude of collision energies, and a geometry scan was performed using $p/d/^3$He+Au collisions, all with the same collision energy. Analyses of these scans have provided important constraints on the physics of a small-system collisions.

This dissertation presents analyses of PHENIX measurements from the small-system geometry scan. The results support the interpretation that quark-gluon plasma is formed in small systems. A theoretical context for these results is established in Chapter 2, followed by an experimental context in Chapter 3. Details of the analysis methods used are given in Chapter 4. Chapters 5 and 6 provide the experimental results, which are then discussed in greater detail in Chapter 7.

Chapter 2

Theory Introduction

This chapter outlines the fundamental interactions of the standard model, describes the contemporary picture of how a heavy-ion collision evolves, and introduces theoretical frameworks used to model relativistic heavy-ion collision systems.

2.1 Fundamental Forces

Each of the fundamental forces described by the standard model play a role in understanding relativistic heavy-ion collisions. Some basic properties of each force are listed in Table 2.1. General relativity, electroweak theory, quantum electrodynamics, and quantum chromodynamics are the theoretical frameworks used to describe the gravitational, weak, electromagnetic, and strong interactions, respectively. The weak and electromagnetic interactions will be discussed here in brief, and Section 2.2 is dedicated to discussing quantum chromodynamics and the strong interaction, which is dominant in the quark-gluon plasma.

Interaction	**Force Carrier**	**Coupling Constant**	**Range (m)**
Gravitational	Graviton (theorized)	10^{-39}	Infinite
Weak	W, Z bosons	10^{-6}	10^{-18}
Electromagnetic	Photon	1/137	Infinite
Strong	Gluon	see Figure 2.5	10^{-15}

Table 2.1: Basic properties of the fundamental forces.

Figure 2.1 shows Feynman diagrams of the basic interactions of the weak and electromagnetic forces. An electromagnetic force exists between any two particles carrying electric charge, and the strength of that force depends on the magnitude of the charges and the distance between the particles. As depicted by Figure 2.1(a), the force is mediated by

a photon. The weak interaction is mediated by W and Z bosons, where the W boson is electrically charged and the Z boson is electrically neutral. As depicted by Figure 2.1(b,c), these bosons can interact with each other. Additionally, the W boson facilitates the decay of an electron, muon, or tau particle into its corresponding neutrino (Figure 2.1(d)) and the decay of a quark into a differently flavored quark (Figure 2.1(e)). The Z boson can mediate an interaction between two fermions (Figure 2.1(f)).

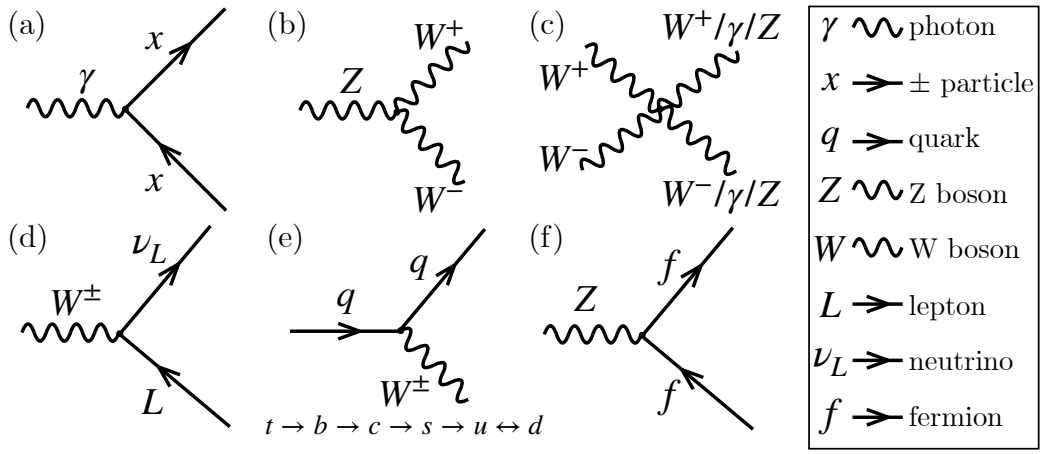

Figure 2.1: Feynman diagrams of electroweak interactions. Conservation laws must be maintained, and the diagrams can be rotated.

For all of these forces, the strength of the interaction is directly proportional to the square root of the interaction's coupling constant (see Table 2.1). The strong and electromagnetic interactions are very fast while, by comparison, the weak interaction is slow. In relativistic heavy-ion collisions, weak decays are distinguishable by their occurrence some distance away from the primary collision, when the system has had time to expand.

Measurements of photons, W bosons, and Z bosons have played an important role in inferring the properties of the quark-gluon plasma.

2.2 Quantum Chromodynamics

According to quantum chromodynamics (QCD), there exist six types or flavors of quarks (up, down, strange, charm, bottom, top) and one type of gluon. The term *par-*

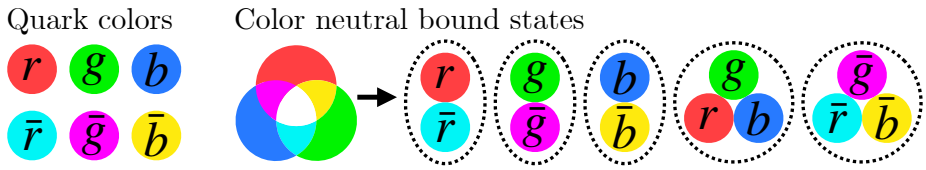

Figure 2.2: Color (QCD charge) options available to quarks and combinations of color which produce neutral bound states.

ton is used to refer to quarks and gluons collectively. As noted in the inset to Figure 2.1(e), a quark can decay into a differently flavored quark through the weak interaction. While other types of inter-quark interactions occur, the weak interaction is the only mechanism for flavor change. Quarks have color charge, a concept analogous to electric charge but associated with the strong force. Unlike electric charge, color charge has three "positives" each of which have their own "negative". As shown in Figure 2.2, this charge triad is described by the colors red (r), green (g), and blue (b) with anti-red ($\bar{r}$), anti-green ($\bar{g}$), and anti-blue ($\bar{b}$) counterparts. Every quark has one unit of color charge. Color changes between quarks occur during strong force interactions mediated by gluons (see Figure 2.3), which themselves carry color charge. Gluons always have two colors of charge associated with them, though these pairings are restricted to an octet of superimposed states which are listed in Table 2.2. When a quark is bound to another quark which has its anti-color (e.g. $r\bar{r}$), the composite particle is considered color neutral, as is familiar with electric charge. However, color can additionally be neutralized through the combination of (anti-)red + (anti-)blue + (anti-)green. The properties of the strong interaction require that all hadrons are color neutral. All quarks additionally carry some fractional electric charge, while gluons are electrically neutral.

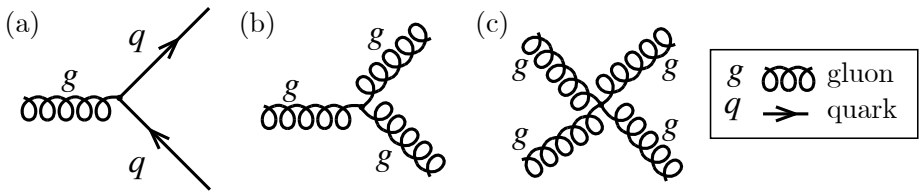

Figure 2.3: Feynman diagrams of strong interactions.

Parton	Flavor	Rest Mass (MeV)	Electric Charge (e)	Color Charge
Quark	Up	$2.2^{+0.6}_{-0.4}$	$+\frac{2}{3}$	r, b, g, $\bar{\text{r}}$, $\bar{\text{b}}$, $\bar{\text{g}}$
	Down	$4.7^{+0.5}_{-0.4}$	$-\frac{1}{3}$	r, b, g, $\bar{\text{r}}$, $\bar{\text{b}}$, $\bar{\text{g}}$
	Strange	96^{+8}_{-4}	$-\frac{1}{3}$	r, b, g, $\bar{\text{r}}$, $\bar{\text{b}}$, $\bar{\text{g}}$
	Charm	1270 ± 30	$+\frac{2}{3}$	r, b, g, $\bar{\text{r}}$, $\bar{\text{b}}$, $\bar{\text{g}}$
	Bottom	4660^{+40}_{-30}	$-\frac{1}{3}$	r, b, g, $\bar{\text{r}}$, $\bar{\text{b}}$, $\bar{\text{g}}$
	Top	$173,210 \pm 710$	$+\frac{2}{3}$	r, b, g, $\bar{\text{r}}$, $\bar{\text{b}}$, $\bar{\text{g}}$
Gluon		0	0	SU(3) color octet: $(r\bar{b}+b\bar{r})/\sqrt{2}$, $-i(r\bar{b}-b\bar{r})/\sqrt{2}$, $(r\bar{g}+g\bar{r})/\sqrt{2}$, $-i(r\bar{g}-g\bar{r})/\sqrt{2}$, $(b\bar{g}+g\bar{b})/\sqrt{2}$, $-i(b\bar{g}-g\bar{b})/\sqrt{2}$, $(r\bar{r}-b\bar{b})/\sqrt{2}$, $(r\bar{r}+b\bar{b}-2g\bar{g})/\sqrt{6}$

Table 2.2: Summary of parton properties [1].

The fact that gluons carry the charge associated with the force which they mediate distinguishes them from all other force carriers, and is the underlying reason that the strong force is much different from all other forces. Specifically, as the distance between two partons increases, the gluons mediating the interaction between them interact with each other forming a gluon flux tube with high energy density, illustrated on the left side of Figure 2.4. As a result, the potential energy between the partons *increases* with distance. If the partons continue to move away from each other, the system reaches a point where it becomes energetically favorable to create a new parton pair, instead of continuing to increase the energy concentrated between the original parton pair. This phenomenon is termed *confinement* because it prevents the partons from ever existing in isolation.

Confinement makes it difficult to study the properties of individual partons because they always exist in bounds states. In order to study quarks where the interactions between them

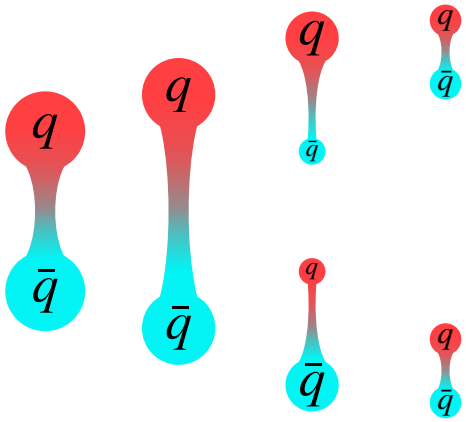

Figure 2.4: From left to right, a quark and anti-quark being being pulled apart form a color flux tube between the them which facilitates the production of two new quarks, resulting in two quark pairs.

are weakest, the energy scale must be high because that is where the coupling constant is smallest (Figure 2.5). The high energy or, equivalently, small distance boundary is called *asymptotic freedom*. Relativistic collisions are used to explore quantum chromodynamics because, as illustrated in Figure 2.6, the high energy density system produced melts the color neutral bound states to form a system of quarks and gluons that are close together. This is the quark-gluon plasma.

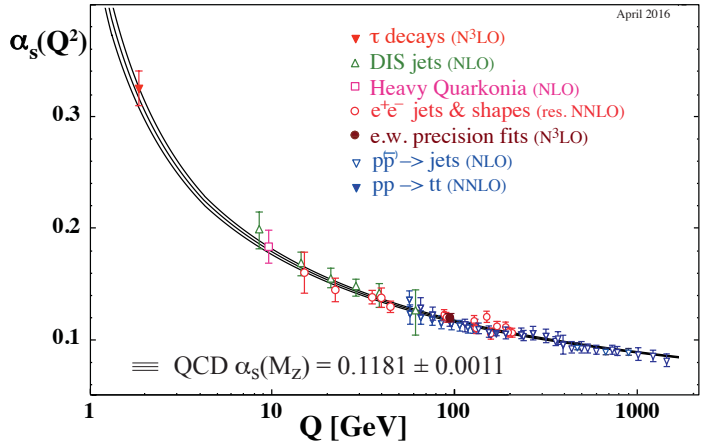

Figure 2.5: The QCD coupling constant (α_s) as a function of energy scale (Q). Image credit: Ref. [1].

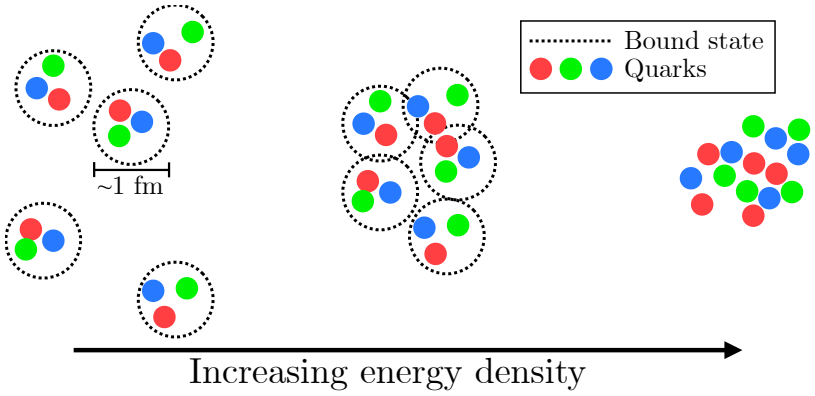

Figure 2.6: From left to right, quarks confined in color-neutral baryons become unbound in a heavy-ion collision as the energy density increases.

2.3 Quark-Gluon Plasma

In the process of formulating a theoretical description of a colliding hadronic system, Rolf Hagedorn found that conservation laws and self-consistency required some critical temperature, at which hadronic matter would boil [16]. As the substructure of hadrons came to be understood, this temperature became better known as the transition temperature required to make quark-gluon plasma. Before it was created experimentally, the quark-gluon plasma was expected to have high enough energy density, such that the partons would approach asymptotic freedom and be weakly interacting. As such, the prediction was that quark-gluon plasma would be gas-like [17]. It came as a surprise then, when it was observed to behave like a strongly interacting fluid. As it turns out, despite its extreme energy density, quark-gluon plasma does not approach asymptotic freedom. In these experiments only hard scattering processes, the instances where the highest momentum transfer occurs, are well described by perturbative QCD calculations in which deconfinement conditions are implicit due to the required assumption of a small coupling constant. The fluid quark-gluon plasma, on the other hand, is so strongly interacting that it approaches the theorized lower limit of shear viscosity over entropy density making it the most 'perfect' fluid ever.

The contemporary view of the upper limit for the temperature of hadronic matter is understood as a phase transition between hadronic and partonic matter, as depicted in Fig-

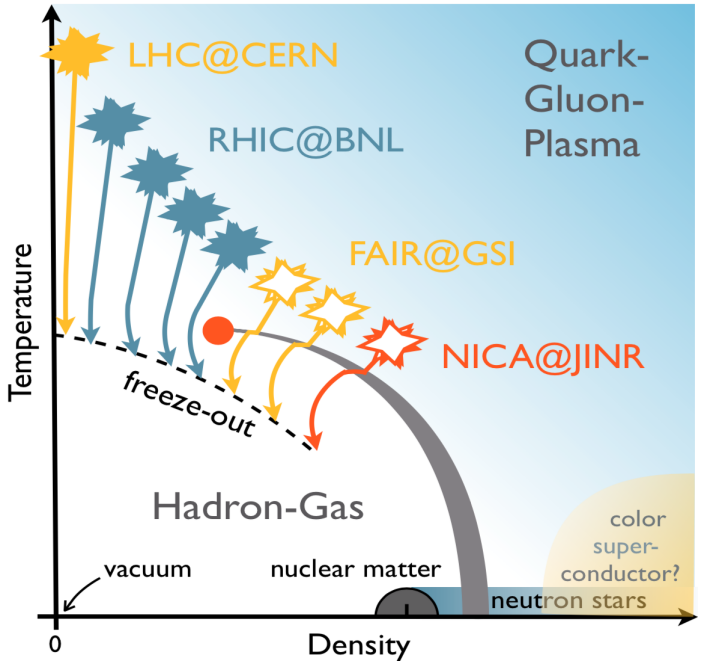

Figure 2.7: A phase diagram of nuclear matter showing the temperature and density dependence of the phase. The path followed by collisions from various experiments are drawn as curved arrows. Image credit: Ref. [9]

ure 2.7. The transition temperature is now understood to have a strong dependence on density. While it has been well established that the transition into quark-gluon plasma has been achieved, the exact position of the phase transition has yet to be well constrained by experiments and the current status of calculations from first principles have some limitations. In Figure 2.7, the transition is depicted as a dashed line at low density where it occurs as a smooth crossover between phases. The critical point is shown as a red circle connected to a curved, grey band which indicates a line of first order phase transitions [9].

One of the major ongoing aims of the field is to continue to probe the quark-gluon plasma in an attempt to clarify the fundamental mechanisms driving its properties. A theoretical understanding of how the microscopic structure of the quark-gluon plasma results in the macroscopic features which have been experimentally observed relies partially on measurements of nuclear collisions at the critical boundaries limiting quark-gluon plasma creation. This dissertation focuses on the size limitation of quark-gluon plasma production,

asking how small a droplet of quark-gluon plasma can be. Equally important studies exploring other boundaries, such as the search for a critical point in the nuclear phase diagram have been and continue to be conducted at RHIC. In order to characterize a quark-gluon plasma system, measurements have constrained values of properties such as viscosity, density, and the equation of state. Temperature dependence of each property must also be considered because quark-gluon plasma created in high energy collisions is fundamentally dynamical in nature. Chapter 3 describes some of the experimental techniques used to constrain these properties. Understanding the quark-gluon plasma from relativistic heavy-ion collision results requires developing a picture of how the system undergoes the trajectory depicted by the curved arrows in Figure 2.7.

2.4 Relativistic Heavy-Ion Collisions

The contemporary description of the evolution of a relativistic heavy-ion collision is divided into several stages, each dominated by different physics. As relativistic heavy-ion experiments become increasingly sophisticated and precise, so do the models employed to describe these results. As will be discussed in Chapter 3, different experimental probes are used to isolate the conditions of the system at different evolution times and over different length scales. Figure 2.8 shows the stages of the system evolution, where the collision itself happens at $t = 0$ and all direct measurements are restricted to after the freeze-out stage has occurred. All other stages are not directly experimentally accessible but a range of observables have been developed, which are sensitive to changes in these early evolution phases and have been used to constrain models of these stages.

2.4.1 Initial State

The initial state of a relativistic heavy-ion collision refers to the state of the system when the collision has just occurred. It describes only the static distribution of nuclear matter as determined by the collision interactions. In a full model of a relativistic heavy-

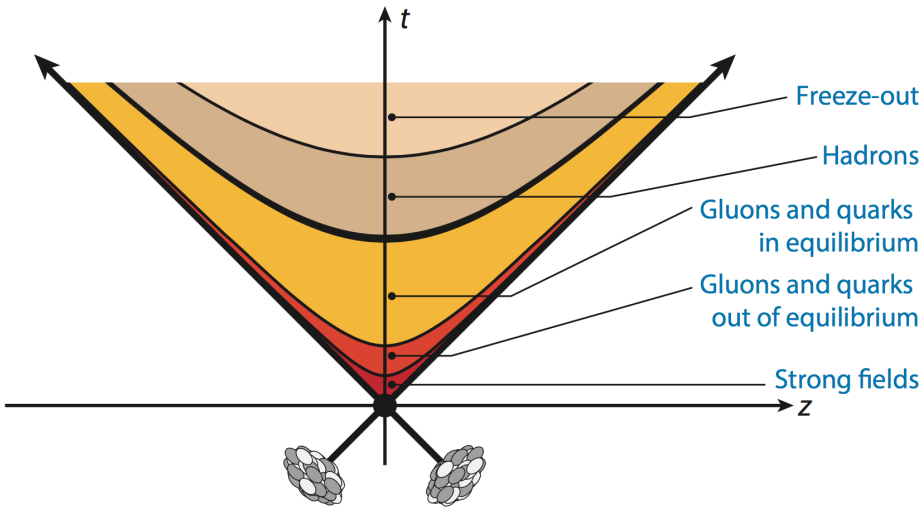

Figure 2.8: Evolution of a relativistic heavy-ion collision. Image credit: Ref. [10]

ion collision, the results of an initial state calculation are used as starting conditions for a calculation which describes the dynamic evolution of the system as it cools and expands, as will be discussed in Section 2.4.2. Many models of the initial state exist. This section will discuss two approaches: Monte Carlo Glauber (MC-Glauber) and initial state momentum correlations.

MC-Glauber models are a straightforward approach to describing the initial state at the nucleon level. For a given simulated collision event, the target and the projectile nuclei are each described in terms of two dimensional distributions of nucleons. These are constructed based on the probability distribution relevant for the particular nuclear species. The collision is assigned some impact parameter (b) which determines how the two nuclei are overlaid. Some nucleon-nucleon interaction criterion is established, a simple example being some minimum distance between the centers of the nucleons. Nucleons which fulfill this condition are marked as participants, while nucleons that do not are marked as spectators. MC-Glauber calculations assume that spectator nucleons continue along their trajectories undeflected, while participant nucleons undergo one or more interactions, forming the initial state.

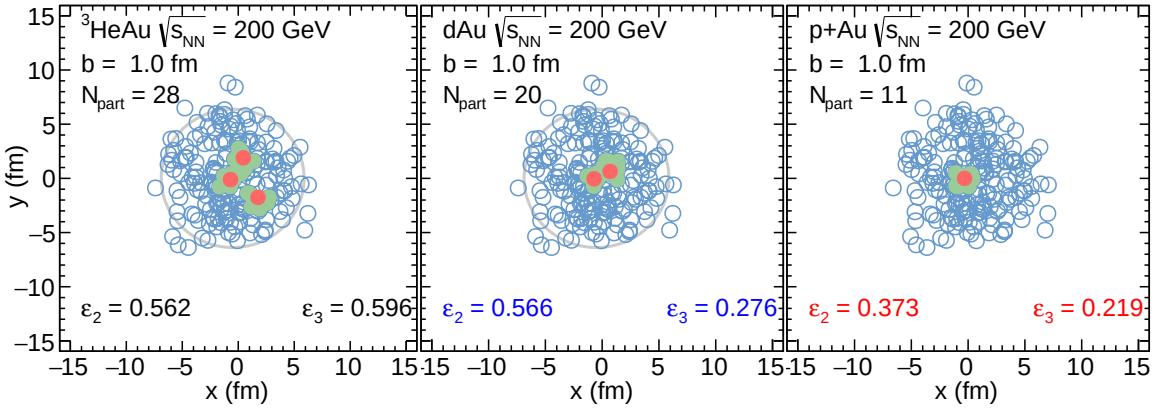

Figure 2.9: Spatial distribution of nucleons according to a MC-Glauber model depiction of a characteristic central ^{3}He+Au (left), d+Au (middle), and p+Au (right) collision at $\sqrt{s_{NN}}$ = 200 GeV. Participating nucleons are filled green (target) and red (projectile) circles; spectator nucleons are open blue circles.

Figure 2.9 shows a single MC-Glauber collision event example for each of the three collision systems analyzed in this dissertation, $p/d/^3$He+Au, with center-of-mass energy per nucleon pair ($\sqrt{s_{NN}}$) of 200 GeV. For each event, the projectile nucleons are shown as red circles, participant nucleons from the target are shown as green circles, and spectator nucleons are shown as open blue circles. This procedure forms an array of participant nucleons with known spatial coordinates, so a useful function of this approach is that it provides the ability to parameterize the initial-state energy density in terms of this distribution. This is also one of the most straightforward ways of gaining insight into collision features which are not directly measurable, such as the number of participants (N_{part}) or geometry features, such as the eccentricity:

$$\varepsilon_n = \frac{\sqrt{\langle r^n \cos(n\phi)\rangle^2 + \langle r^n \sin(n\phi)\rangle^2}}{\langle r^n \rangle}, \tag{2.1}$$

where r and ϕ are polar coordinates of participating nucleons [13]. The spatial distribution (sometimes referred to as *geometry*) of the initial state has been shown to be a significant factor in determining final state particle distributions when quark-gluon plasma is produced, so a theoretical approach to quantifying the geometry is essential to understanding

the properties of quark-gluon plasma. Initial state calculations for characterizing geometry are performed on an event-by-event basis and then averaged over many events of a particular class, which matches the event selection of the analysis. The MC-Glauber approach is utilized in the discussion and interpretation of the results presented in this dissertation.

The color-glass condensate is an effective theory of gluons under the specific condition of saturation. The momentum of a hadron is distributed among its constituent partons whose fraction of the total momentum is called x. At small x, gluon occupancy begins to increase at a high rate, but some limit to this increase is required by the necessity for unitarity of the wave function. In the gluon saturation domain (high energy, small x), gluons continuously recombine in order to limit their numbers. Partons in the dense (saturated) regime have momenta less than Q_s, and partons in the dilute (unsaturated) regime have momenta much greater than Q_s, where Q_s is the saturation momentum scale.

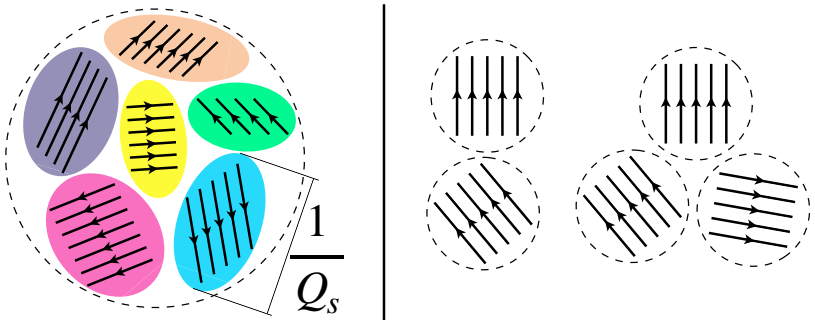

Figure 2.10: Cartoon depiction of color domain correlations in a nucleon (left) and the combined effect of multi-nucleon combinations (right).

One implementation of the color-glass condensate is a description the initial state of a heavy-ion collision in terms of color domains which are analogous to ferromagnet domains. The left side of Figure 2.10 shows a nucleon with some number of uncorrelated color domains whose size depends on Q_s. Depending on the value of Q_s, there is some probability that the color domains will combine such that the nucleon has some net momentum correlation. In p+A collisions these initial state momentum correlations may directly translate to final state momentum correlations. As the number of nucleons in the projectile increases

the net momentum correlation in the initial state is expected to dilute (see Figure 2.10, right).

2.4.2 Evolution of Hot, Dense System

It has been well-established that quark-gluon plasma behaves as a relativistic fluid, so this section focuses on the general assumptions of hydrodynamical models [18]. The overall purpose of hydrodynamical models is to take the energy density distribution output from an initial state model, evolve it with relativistic hydrodynamics, and calculate how the macroscopic system changes up until the point where the system has cooled enough that it transitions into a hadronic phase. A range of models exist which calculate the hadronization process itself by describing how the bulk fluid forms hadrons in a way that obeys conservation laws. Most contemporary hydrodynamical models use a hybrid approach, which couples the hadronized system to a microscopic hadronic scattering model wherein some continued evolution will occur, as described in Section 2.4.3. The results presented in this dissertation include comparisons to three hydrodynamical calculations from the models, SONIC [19], superSONIC [20], and iEBE-VISHNU [21], which include a hadronic rescattering stage. Additional calculations from the iEBE-VISHNU model will be shown, which do not utilize hadronic scattering but instead treat the system macroscopically throughout the entire evolution, hadronizing only at the very end to determine the final state particle distribution. This approach is quantitatively inaccurate, but it is useful to consider as a way of isolating the influence of the hadronic scattering stage.

Figure 2.11 shows the time evolution of a characteristic collision for each of the three collision systems analyzed in this dissertation, $p/d/^3$He+Au at $\sqrt{s_{NN}}$ = 200 GeV, as calculated by a hydrodynamical model called SONIC [19]. Each panel displays the temperature profile of the collision event as a function of its spatial distribution. Consecutive panels, going from left to right, show this profile for a series of time points over the course of which the collision system cools and expands into a dynamical distribution depicted by

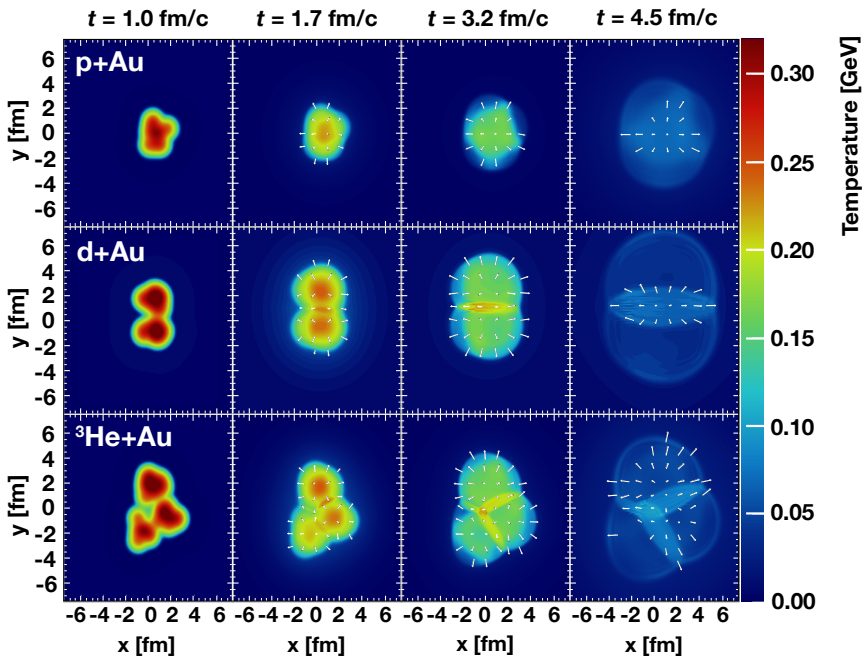

Figure 2.11: Evolution of a characteristic central p+Au (top row), d+Au (middle row), and ^{3}He+Au (bottom row) collision at $\sqrt{s_{NN}}$ = 200 GeV as calculated by hydrodynamical model SONIC. Each panel shows the spatial distribution of the temperature of the nuclear matter at a given time point. The velocity field of the fluid cells is depicted by arrows, with the longest arrow plotted corresponding to a magnitude of 0.82 c.

arrows, which represent the velocity field of the nuclear matter. Note that the shape of the velocity field depicted corresponds roughly to the shape of the distribution of matter from which it evolved. Within the hydrodynamical framework, this transference of azimuthal anisotropy from the initial state spatial distribution to the final state velocity (or momentum) distribution is the primary mechanism responsible for the momentum anisotropy in the particle distribution at the time of measurement. In order to understand how this transference occurs, consider the middle row which depicts a d+Au collision. At $t = 1.0$ fm/c the d+Au collision roughly forms an elliptical matter distribution with a short axis which is parallel to the x-axis. This results in there being more pressure exerted along the x-axis and, correspondingly, the velocity field at $t = 4.5$ fm/c being oriented such that the average magnitude of the velocity is greater along the x-axis than the y-axis. The distribution of the velocity anisotropy is essentially an ellipse perpendicular in orientation to the ellipse

formed by the initial matter distribution. In other words, the shape of the velocity field corresponds inversely to the initial matter distribution which set the pressure gradient. This transference can be seen in all three systems with dominantly radial, elliptic, and triangular velocity distributions in p+Au, d+Au, and ^{3}He+Au, respectively.

A prevalent assumption in hydrodynamical models is that the system reaches local thermal equilibrium, but when the system is small and short-lived, it is unclear how this condition could physically come about. However, there is an increasing body of evidence, including the results that follow, which strongly suggest that hydrodynamical models are the best descriptors of the class of events in small systems where the multiplicities of the produced particles are highest. As such, hydrodynamics outside of equilibrium is an ongoing area of study, as is the examination of mechanisms which could bring about very fast thermalization.

Hydrodynamical models utilizing a quark-gluon plasma equation of state have had significant success in describing and predicting large systems results [18]. As this dissertation shows, measurements in small systems are also well-described by these calculations utilizing the same parameters that have been used in large systems. This is strong evidence that quark-gluon plasma droplets are being created in small systems.

It should be noted that there are ongoing efforts to described the evolution of this hot partonic matter microscopically through partonic scattering models. These calculations use an initial state model to determine the parton distribution of the system just after the collision has occurred. This distribution is evolved through a series of parton-parton interactions. When partons stop scattering, hadronization occurs which requires some description of how the partons combine into hadrons in a way that obeys conservation laws. The results presented in this dissertation include a comparison to one partonic scattering model, A Multi-Phase Transport (AMPT) model [22], which uses a parton-parton cross section determined from leading order QCD calculations. At this point in time, comparisons to partonic scattering models must be interpreted with the understanding that, unlike hydro-

dynamical models, it is not yet clear if a simultaneous description of both small and large collision systems is possible while using the same model parameters governing the particle interactions.

2.4.3 Hadronic Rescattering

As has been discussed, modern models of relativistic heavy-ion collisions utilize a multi-stage approach. Both hydrodynamical and partonic scattering models can be stopped at the transition temperature in order to convert the system into hadrons. The resulting hadronic distribution can then be sent to a hadronic cascade model to determine late stage dynamics. Rescattering can have a significant impact on the final state particle distribution.

The general prescription followed by hadronic cascade codes is that the hadrons follow straight-line trajectories until they encounter another hadron, at which point the result of the interaction is determined by hadronic scattering cross sections. Direct measurements of these cross sections are limited and only well understood for specific cases such as a pion gas. A major source of uncertainty in this procedure is the utilization of extrapolations or estimates to determine hadronic cross sections, the specifics of which differ by hadronic cascade code.

When inelastic collisions between hadrons cease, the system is considered to be in chemical freeze-out [23], at which point the particle abundances are fixed. Final particle production ratios are well-described by a statistical model utilizing the grand canonical ensemble of an ideal hadron gas in thermal equilibrium, dependent only on the temperature and baryochemical potential at chemical freeze-out. Elastic collisions may continue to occur up until kinetic freeze-out, at which point all hadronic rescattering becomes negligible, leading to frozen transverse momenta.

Measurements of the temperatures associated with the onset of chemical and kinetic freeze-out are useful for constraining models of the hadronic scattering stage. In general, understanding the temperature dependence is especially critical to hybrid multi-stage mod-

els, which use temperature as a boundary condition for determining when each stage is complete. The relative length of the evolution stages may yield different results, so an experimental constraint of the temperature is essential.

Chapter 3

Relativistic Heavy-Ion Experiments

Section 3.1 presents an overview of some classic results from heavy-ion experiments that have led to the contemporary understanding of the properties of quark-gluon plasma. Section 3.2 gives an overview of the small-system results which have motivated the analyses presented in this dissertation. Section 3.3 describes the PHENIX detector which was used to collect the data which were analyzed.

3.1 Large Collision System

The majority of experimental results exploring quark-gluon plasma come from *large systems*, heavy-ion collisions in which both collision species are large ions (see Figure 3.1 top row). At the LHC, the large-system results are all symmetric A+A collisions and are primarily Pb+Pb, while at RHIC the A+A program is primarily Au+Au. The versatility of RHIC has allowed it to additionally collide asymmetric systems which create unique geometries in the initial state, such as collisions between uranium nuclei that are intrinsically deformed, and collisions between differently sized large ions. Overall, analyses from large-system collisions have developed a rich landscape of observables which collectively support the conclusion that quark-gluon plasma is being formed in these systems.

A basic tool for characterizing the medium produced in a collision is the measurement of the multiplicity of the produced particles and the distributions of their transverse momenta (p_T) and transverse energy (E_T). These observables are used to extract information about the collision geometry and can be related to the initial energy density using the Bjorken relation [23, 24]. Similarly, the system's temperature at chemical freeze-out has been constrained by measurements of hadronic yields including identified particle spectra. The extracted temperature and energy density values are near or above the critical lim-

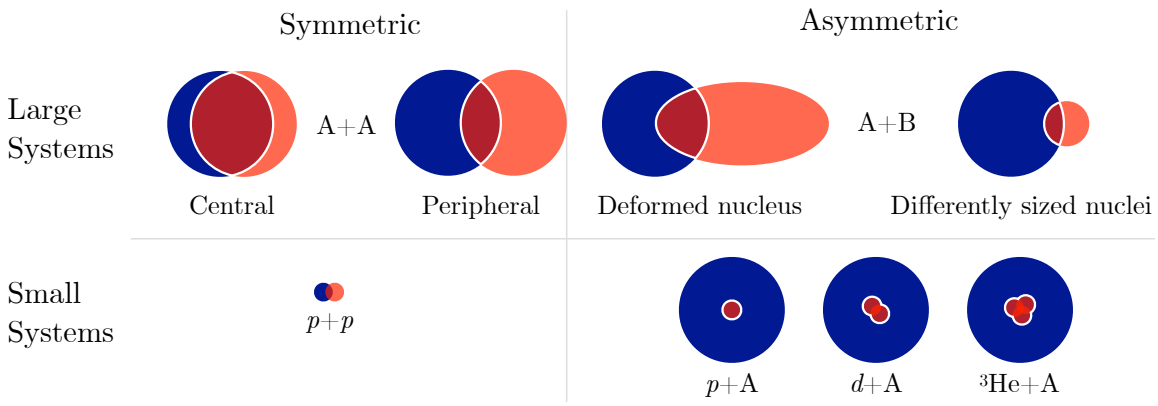

Figure 3.1: Cartoon illustration of (top) large and (bottom) small collision systems. The overlap region, outlined in white, roughly corresponds to the average initial state geometry.

its calculated using lattice QCD, suggesting that a transition to quark-gluon plasma has occurred.

Jets are clusters of particles originating from high momentum scattering early in the collision process. Momentum conservation causes jets to frequently occur in back-to-back pairs. Many measurements have observed a significant energy imbalance between the two jets, a phenomenon which is referred to as jet suppression. The origin of jet suppression has been found to be a difference in the path length travelled through the medium by the scattered partons from which the jets originate. The longer a parton's path length through the medium, the more likely it is to have more interactions with the medium, causing more of its energy to disperse. Measurements of the degree to which a jet was suppressed compared to its counterpart have been used to constrain the density of the medium. Jets in general have proved a fruitful observable with many more intricate analyses of their specific structures and subtypes leading to additional model constraints.

The suppression or enhancement of particular types of particles produced in heavy-ion collisions as compared to p+p collisions has been measured. At high p_T, all particles are suppressed to a similar level, including particles containing heavy quarks such as bottom and charm, as a result of traveling through the hot medium created in heavy-ion collisions. There is an ongoing effort to measure the energy loss of heavy quarks precisely, since they

are expected to lose less energy through gluon radiation than the light quarks. Measurements of the magnitude of the suppression are important for constraining properties of the medium. It has been shown that particles which do not participate in the strong interaction such as photons, W bosons, and Z bosons are unsuppressed - further evidence that the produced medium is quark-gluon plasma.

The azimuthal distribution of particles produced in heavy-ion collisions has been measured to be anisotropic. As with jet suppression, high p_T particles can form an anisotropic distribution due to energy loss that is dependent on the path length through the medium. For low p_T particles, this anisotropy is a feature of the bulk fluid properties of the medium which develops pressure gradients, as was described in Section 2.4.2. Measurements of azimuthal anisotropy have been made in a wide range of collision systems and energies. These results have been used to constrain the viscosity and equation of state of the medium.

A reaction plane, defined by the beam direction and the impact parameter of the colliding nuclei, makes an angle Ψ_R with the experiment coordinate system, as shown in Figure 3.2 (left). In A+A collisions, Ψ_R is naturally related to the initial geometry as the reaction plane bisects the short axis of the elliptic overlap region. One method of measuring azimuthal anisotropy estimates the reaction plane angle and measures the azimuthal distribution of the final state particles, $dN/d\phi$, with respect to it. A Fourier decomposition of $dN/d\phi$ can be taken to break the distribution down into components. The n^{th} order component (or harmonic) has an associated amplitude, v_n, which is sometimes referred to as the *flow coefficient*. The specific analysis techniques used to extract flow coefficients will be discussed in Section 4.2.

Measurements of flow coefficients have been a pillar of heavy-ion analysis. Each order of flow coefficient represents the amplitude of a specific feature of the distribution; for example, v_2 represents elliptic flow and v_3 represents triangular flow. As was discussed in Section 2.4.2, a defining feature of quark-gluon plasma is its ability to translate the initial state spatial anisotropy to final state momentum anisotropy. Correspondingly, collisions

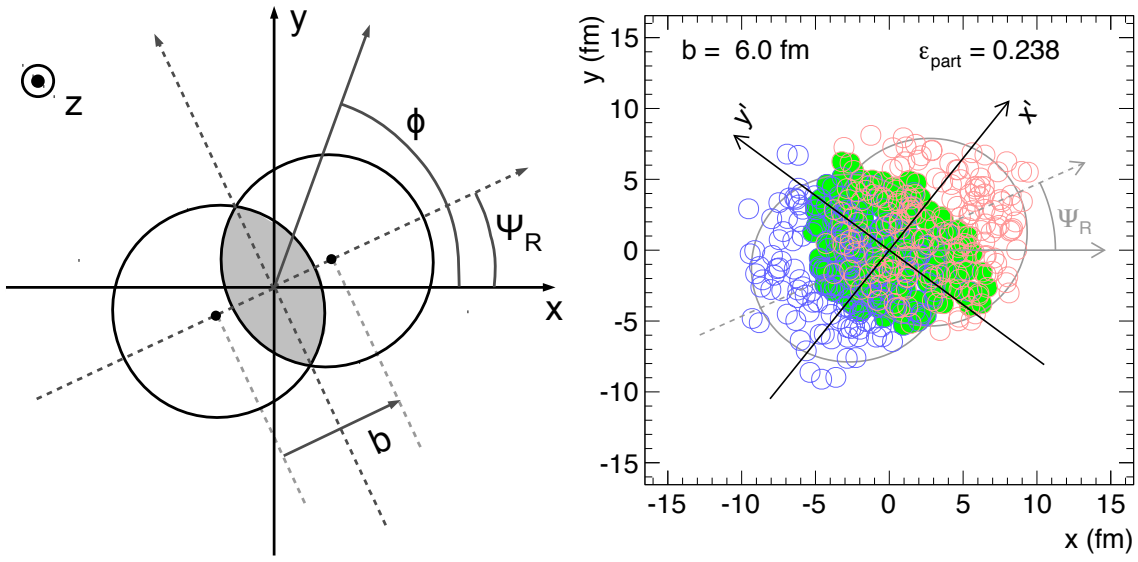

Figure 3.2: (Left) A cartoon A+A collision where the nuclei are moving along the z-axis and the overlap between the nuclei is shaded grey. The reaction plane angle, Ψ_R, is defined by the direction of the impact parameter, b. (Right) A MC-Glauber calculation of a Pb+Pb collision where the filled green circles represent nucleons which participate in the collision and empty circles represent spectating nucleons. The primed axes represent the frame defined by the elliptic anisotropy of the participant distribution. Image credit: Ref. [11]

which produce a highly elliptic system of quark-gluon plasma have been measured to have large v_2. The collective origin of v_2 has been highlighted in measurements of this observable for identified particles, where the magnitude exhibits a dependence on the mass of the particle that is consistent with the particles having emerged from a constant velocity field.

Figure 3.2 (right) shows a MC-Glauber calculation of the nucleon distribution of a Pb+Pb collision event. The primed axes represent the frame defined by the elliptic anisotropy of the participant distribution which, contrary to the smooth nucleus picture, does not neatly align with Ψ_R. The angle between the x- and x'-axes is the nucleon participant angle, Ψ_P.

While the average initial state geometry over many events conforms to the smooth picture, event-by-event fluctuations in the nucleon participant distribution have a major impact on the final state momentum distribution. Unlike the smooth nucleus picture, which produces an entirely elliptic initial state, the nucleon participant distribution has more irregular asymmetry. Figure 3.3 shows two nucleon participant distributions from A+A collision

events, as calculated by a MC-Glauber model, which have vastly different nucleon participant distributions despite having the same impact parameter. Event-by-event fluctuations in the nucleon participant distribution are responsible for the formation of triangular momentum anisotropy which has been measured in A+A collisions. Asymmetric large systems can have intrinsic triangularity in the initial state (Figure 3.1, top right) which has been measured to correspond to a modest increase in v_3 [8].

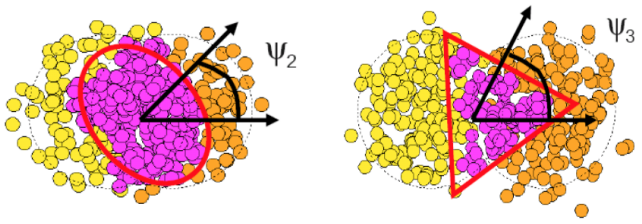

Figure 3.3: Nucleon distributions from two MC-Glauber events where the participants (magenta) have largely elliptic (left) and triangular (right) distributions, where ψ_2 (ψ_3) is the second (third) order symmetry plane angle. Image credit: Ref. [12, 13]

Figure 3.3 also introduces another symmetry angle, the event plane angle (ψ_n) which is defined in terms of the n^{th} harmonic, just as the flow coefficients v_n were and which similarly corresponds to a particular component of anisotropy. As will be discussed in Section 4.2, the event plane angle is determined from the final state particle distribution.

The term *collective flow* is used as shorthand to describe the part of the azimuthal correlations which originates from bulk characteristics of the hot system. This is in contrast to correlations which emerge among a few particles through process like jets and particles decays, whose contribution to the measured azimuthal correlations is termed *nonflow*. It is the combined effects of flow and nonflow that produce the measured $dN/d\phi$ distribution. Most studies of collectivity use analysis techniques to identify and, when possible, remove the nonflow component. This facilitates a more straightforward interpretation of results and allows for comparison to models which do not include background processes. Section 4.4 describes the method of nonflow estimate applied to the presented results.

3.2 Small Collision Systems

Small systems are defined as collisions where one or both ions have very few nucleons. The small ion is generally a proton (A=1), deuteron (A=2), or Helium-3 (A=3), all of which have much fewer nucleons than the commonly used large ions such as gold (A=197) or lead (A=208). Data from small-system collisions has been collected at both RHIC and LHC for many years, though historically these data have been used primarily as a baseline for A+A collisions.

The study of collectivity in small systems is still a somewhat recent development. It was previously thought to be impossible for quark-gluon plasma to form in small systems, so there was no expectation that azimuthal anisotropy would be measured beyond that produced by nonflow effects. The LHC experiments were first to observe features in small-system collisions, which were reminiscent of quark-gluon plasma signatures. This first measurements where of a near-side ridge in high multiplicity events from p+p and p+Pb collisions [25, 26, 27, 28], followed by measurements of v_n in these systems extracted using a many different analysis techniques [29, 30]. The mass dependencies of identified particle flow, which were observed in A+A collisions, have also been observed in small systems [31]. These results motivated the reanalysis of previously recorded d+Au data from PHENIX, which observed similar signals [4, 32]. Further PHENIX analyses have found signs of collectivity in many different small systems [2, 3, 5, 6, 15, 33, 34]. These unexpected results highlighted the need to explore size and duration limits of quark-gluon plasma formation. This has motivated the production of a set of results that will clarify whether these small-system collectivity measurements are strongly dependent on the initial state geometry, as is the case in systems where quark-gluon plasma is produced.

While in large systems the geometry of the initial state is strongly dependent on centrality, this is not the case to first order in small systems (Figure 3.1, bottom) where, in most collision events, all of the projectile nucleons interact with the target. Instead, a series of experiments was proposed to explore the geometry dependence of collectivity in small

systems [35]. It was shown that by comparing final state momentum correlations from three small-system species - proton+gold, deuteron+gold, and either helium-3+gold or tritium+gold - the contribution of the initial spatial anisotropy of the system to the production of final state momentum anisotropy could be evaluated, where a geometry-driven final state would be considered strong evidence for the presence of quark-gluon plasma.

The average initial spatial anisotropy of $p/d/^3$He+Au collisions at $\sqrt{s_{NN}}$ = 200 GeV was quantified utilizing MC-Glauber calculations (Section 2.4.1) of the participant nucleon distributions. The calculations utilized Equation (2.1) to produce n^{th} order eccentricities where ε_2 (ε_3) corresponds to the ellipticity (triangularity) of the initial state. Some assumptions are made about the energy density of nucleons, the effect of which will be examined in Section 7.2. Within this framework, the relationships between the average second and third order eccentricities in these collision systems were calculated to be

$$\begin{aligned} \langle\varepsilon_2\rangle^{p\text{+Au}} &< \langle\varepsilon_2\rangle^{d\text{+Au}} \approx \langle\varepsilon_2\rangle^{^3\text{He+Au}}, \\ \langle\varepsilon_3\rangle^{p\text{+Au}} &\approx \langle\varepsilon_3\rangle^{d\text{+Au}} < \langle\varepsilon_3\rangle^{^3\text{He+Au}}, \end{aligned} \tag{3.1}$$

with the exact values given in Table 3.1.

	$\langle\varepsilon_2\rangle$	$\langle\varepsilon_3\rangle$
p+Au	0.23 ± 0.01	0.16 ± 0.01
d+Au	0.54 ± 0.04	0.18 ± 0.01
^{3}He+Au	0.50 ± 0.02	0.28 ± 0.02

Table 3.1: Average second and third order eccentricities of the initial state of central (0-5%) $p/d/^3$He+Au collisions with $\sqrt{s_{NN}}$ = 200 GeV calculated by a MC-Glauber model.

If the medium created in the collision is quark-gluon plasma, these spatial anisotropies will create pressure gradients, which in turn would produce an anisotropic momentum distribution in the final state as measured by flow coefficients, v_n, which would be expected to exhibit magnitude ordering which exactly follows the initial state eccentricity ordering. As such, measurements of both second and third harmonic flow would provide a powerful

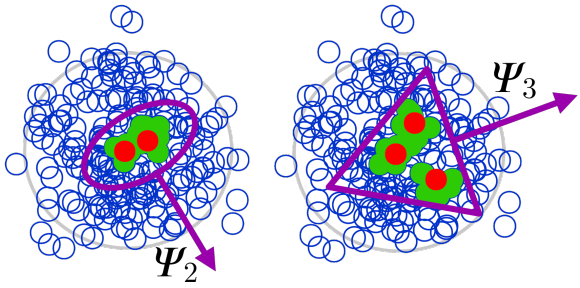

Figure 3.4: Nucleon distributions from a d+Au collision (left) and a ^{3}He+Au collision (right) as calculated by a MC-Glauber model. Participating nucleons are filled green (target) and red (projectile) circles, spectating nucleons are open blue circles. The intrinsic shape of the projectile dominates the geometry determination of the initial state. The second (third) order symmetry plane angle, ψ_2 (ψ_3), is drawn. Image credit: Ref. [6]

model constraint. Figure 3.4 depicts the symmetry plane angles which were introduced in Section 3.1 in a MC-Glauber calculation of a d+Au collision on the left and a ^{3}He+Au collision on the right. In these two systems the intrinsic shape of the nucleus is the dominant source of initial state anisotropy.

This proposed geometry engineering was carried out by RHIC from 2014-2016. This dissertation presents PHENIX measurements of inclusive charged hadron v_2 and v_3 as a function of transverse momentum in $p/d/^3$He+Au collisions with a nucleon-nucleon center-of-mass energy $\sqrt{s_{NN}}$ = 200 GeV.

3.3 PHENIX Detector

The PHENIX (Pioneering High Energy Nuclear Interaction eXperiment) collaboration was established as part of the development of RHIC at BNL. The PHENIX detector was initially designed to be complementary to three other experiments that were established at RHIC around the same time - STAR, PHOBOS, and BRAHMS - which shared PHENIX's physics goal of studying quark-gluon plasma. PHENIX collected data for sixteen years, during which time the detector underwent substantial upgrades. The detector was disassembled in 2016, but the PHENIX collaboration continues to work on extracting physics results from the wealth of data that was collected.

The subdetectors of PHENIX work together to build a picture of the particles that emerge from a heavy-ion collision event. In order to identify particles and measure their characteristics, several different types of detectors are used in conjunction. The geometry conventions of PHENIX are similar to other comparable experiments and are summarized in Figure 3.5. The z-axis is oriented along the beam pipe, and the orthogonal (x-y) plane is called the transverse plane. Final state particles with nonzero transverse momentum,

$$p_T \equiv \sqrt{p_x^2 + p_y^2}, \tag{3.2}$$

must originate from particle production, since the original colliding ions have $p_T = 0$. One can also measure particle pseudorapidity,

$$\eta \equiv -\ln\left(\tan\frac{\theta}{2}\right), \tag{3.3}$$

where the region near $\eta = 0$ is called midrapidity and the large $|\eta|$ region is described as forward or backward rapidity (see Figure 3.5). PHENIX convention refers to the positive (negative) η side of the detector as *north* (*south*). In $p/d/^3$He+Au collision experiments the gold ion always enters the interaction region traveling from north to south.

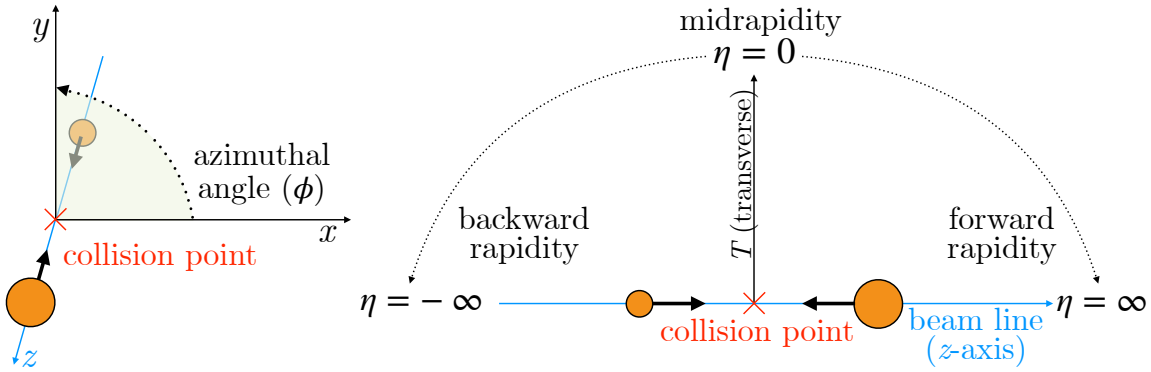

Figure 3.5: The beam axis, along which the nuclei travel is defined as the z-axis. The transverse direction (T) is in the $x-y$ plane which is also where the azimuthal angle (ϕ) is measured. Pseudorapidity (η) is defined orthogonally to the transverse direction with midrapidity describing the region where $|\eta|$ is small and forward/backward rapidity describing the region where $|\eta|$ is large.

The collision point depicted in Figure 3.5 should be considered the nominal interaction point, as the collisions actually occur over a range of points along the z-axis. The z-coordinate of the actual collision interaction for a given event is called the z-vertex and is determined experimentally.

A schematic showing the locations of the various PHENIX subdetectors is given in Figure 3.6. The analysis presented in this dissertation utilizes particle tracking performed by two central arms at midrapidity, each covering $|\eta| < 0.35$ and $\frac{\pi}{2}$ in azimuth [36]. The central arms are made up of several subdetectors, which include drift chambers and pad chambers. Charged particle trajectories are determined in these subdetectors and algorithmically matched to determine the particle's *track*. This matching model takes hits in the drift chamber, the innermost subsystem, and projects the particle trajectory out to the location of the pad chambers, where it looks for a hit measurement which could correspond to the same particle. As will be described in Section 4.1, some cut must be set to determine the statistical confidence of this matching assignment.

Beam-beam counters located at forward and backward rapidities ($3.1 < |\eta| < 3.9$), each consist of an array of 64 quartz Cherenkov radiators read out by photomultiplier tubes [7]. These detectors provide event triggering, collision vertexing, and event-plane angle determination (see Section 4.2). Additionally, forward vertex detectors covering $1.0 < |\eta| < 3.0$ and composed of high efficiency silicon mini-strips [37] provide an independent event-plane angle determination. A complete description of the PHENIX detector can be found in Ref. [38].

In order to analyze the data, it is useful to subdivide the collision events in terms of certain categories. Centrality is an experimental variable that roughly corresponds to impact parameter. A collision is described as being more central if the impact parameter is small and more peripheral if the impact parameter is large. Centrality is expressed in bins that are labeled in percentage from the total inelastic cross section with 0% centrality representing the most central events of a data set and 100% representing the most peripheral.

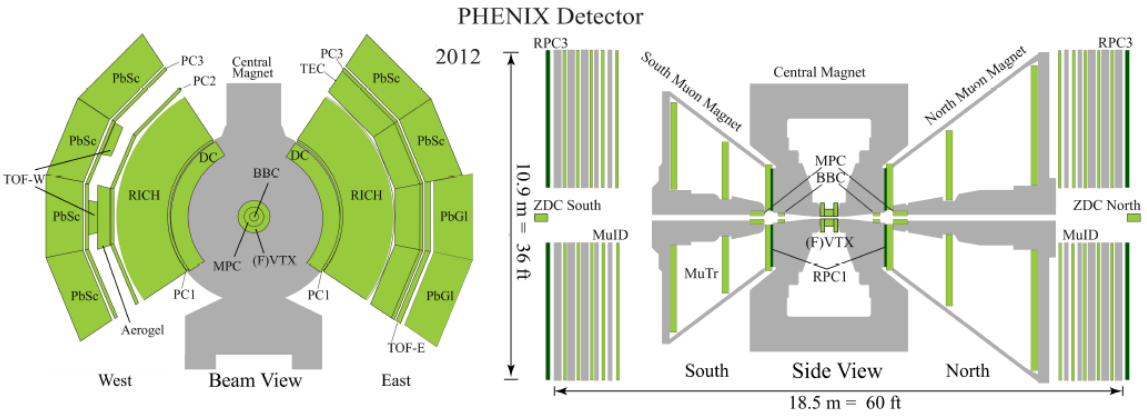

Figure 3.6: (Left) The PHENIX detector viewed such that the beam is traveling in/out of the page through the center. (Right) The PHENIX detector viewed such that the beam is traveling right/left through the center. Image credit: PHENIX

For the results presented here, event centrality is determined using the total charge collected in the south BBC [7].

Chapter 4

Data Analysis Methods

The results presented in this dissertation focus on the measurement of azimuthal momentum anisotropy of the particles produced in several small collision systems, in order to investigate the collective flow effect. This observable has been shown to be a robust in testing model predictions with regards to quark-gluon plasma [39]. It has been measured in a wide range of collision systems and energies at many different experiments. Several methods exist for extracting this observable including the event plane method, pairwise correlations between particles, and correlations between multiplets.

This chapter refers to specific PHENIX subdetectors and geometry conventions, all of which were defined in Section 3.3. Section 4.1 describes triggers and cuts that were applied. Sections 4.2 and 4.3 describe the event plane method and the two-particle correlation method, respectively, for determining final state correlations. The methods used to estimate associated uncertainties are described in Section 4.4.

4.1 Event and Particle Selection

Two triggers were utilized to determine online event selection. A minimum bias trigger was used to identify the presence of a collision in the interaction region. As is standard in the PHENIX experiment, the minimum bias trigger required at least one hit in both the north and south beam-beam counter. This minimum bias trigger additionally required that the collision occur within $|z_{\text{vertex}}| < 10$ cm of the nominal interaction region. The specific analysis discussed here utilizes only the most central events, so an online high multiplicity trigger requiring a certain number of hits (dependent on the collision system) in the south beam-beam counter was developed to prioritize the storage of these events.

This analysis also performed several offline cuts to select events. Occasionally, multiple nucleus-nucleus collisions occur during a single bunch crossing. These events, referred to as double interaction events or pileup, were rejected using an algorithm based on beam-beam counter charge and timing information [5]. Centrality categorization was performed [7] and a cut retaining only the 5% most central events was applied.

As described in Section 3.3, particle tracks are determined according to matching criteria which combine information collected by the drift chamber and pad chambers. In order to reduce background from tracks originating from sources other than the primary interaction or uncertainty introduced from incorrect track reconstruction, some track selections were applied. The quality of the utilized tracks was found to be improved when the track was required to contain hits in both the drift chamber and the outermost pad chamber layer with three standard deviations of agreement [2, 3, 5].

4.2 Event Plane Method

The event plane method was developed by A. M. Poskanzer and S. A. Voloshin in 1998. It is used to estimate the participant plane, which was introduced in Section 3.1. It identifies an event plane angle (ψ_n) as corresponding to the n^{th} order symmetry plane and then finds the azimuthal distribution of all particles in an event with respect to the event plane angle [40, 41]. This process produces a correlation function, the Fourier decomposition of which yields the flow parameters or v_n coefficients. Specifically, the Fourier decomposition of $dN/d\phi$ distribution is studied,

$$\frac{dN}{d\phi} \propto 1 + \sum_n 2v_n(p_T)\cos(n(\phi - \psi_n)), \tag{4.1}$$

where p_T and ϕ are the transverse momentum and the azimuthal angle of a particle and ψ_n is the n^{th} order event plane angle. The analysis presented here measures elliptic and triangular flow, which correspond to the second and third order expansion coefficients in Equa-

tion (4.1), represented symbolically as v_2 and v_3. The event plane angle is defined as

$$\psi_n = \frac{1}{n} \arctan \frac{\sum_i^N \cos n\phi_i}{\sum_i^N \sin n\phi_i}, \tag{4.2}$$

where N is the number of particles and ϕ_i is the azimuthal angle of each particle.

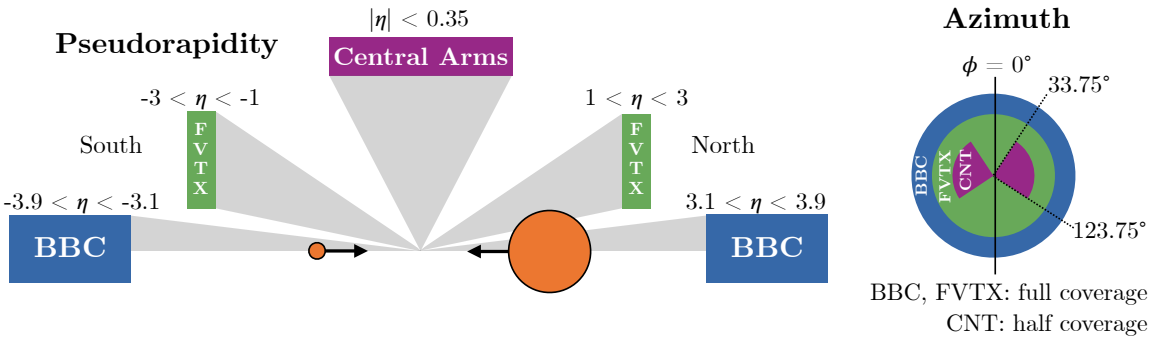

Figure 4.1: PHENIX azimuthal and pseudorapidity coverage in the beam-beam counter, forward vertex detector, and central arm subdetectors.

Figure 4.1 shows the coverage of the PHENIX subdetectors used in this analysis. In PHENIX, ψ_n is measured using either the south beam-beam counter or the south forward vertex detector. The orientation of ψ_n is random on an event-by-event basis, so the measured distribution of these angles should be flat. In reality, there is some nonuniformity in the azimuthal acceptance of the detectors used to measure ψ_n, so a flattening procedure is applied as a correction. The measurement of ψ_n has some associated precision, which is affected by the resolution of the detector and the number of particles that were used to determine ψ_n. This precision was quantified using a resolution term, $R(\psi_n)$, which was calculated using the three-subevent method that correlates measurements in the south beam-beam counter, south forward vertex detector, and central arms (represented as A, B, and C, respectively):

$$R(\psi_n^A) = \sqrt{\frac{\langle \cos n(\psi_n^A - \psi_n^B) \rangle \langle \cos n(\psi_n^A - \psi_n^C) \rangle}{\langle \cos n(\psi_n^B - \psi_n^C) \rangle}} \tag{4.3}$$

The v_n values are measured to be

$$v_n = \frac{\langle \cos(n(\phi - \psi_n) \rangle}{R(\psi_n)}, \tag{4.4}$$

where ϕ is the azimuthal angle of particles emitted at $|\eta| < 0.35$, as measured by the central arm. This establishes a large η separation between these midrapidity particle tracks and the event plane angle measurement (at backward rapidity), which has the effect of significantly reducing the nonflow contribution.

4.3 Two-Particle Correlation Method

The two-particle correlation method is similar to the event plane method in that it is a way to measure momentum correlations in the final state particle distribution. Instead of correlating to a particular symmetry angle, the two-particle correlation method assess azimuthal correlations between long-range particle pairs. In the context of this dissertation, this method is used in the procedure for estimating the contribution of nonflow correlations (see Section 4.4) and, in some cases, as a cross-check for results obtained using the event plane method.

For PHENIX analyses, the two-particle correlation method is implemented by constructing a normalized correlation function between midrapidity tracks and signals from the beam-beam counter photomultiplier (PMT) tubes,

$$S(\Delta\phi, p_T) = \frac{d(Q_{\mathrm{PMT}} N_{\text{same event}}^{\text{track}(p_T)-\mathrm{PMT}})}{d\Delta\phi}, \tag{4.5}$$

$$C(\Delta\phi, p_T) = \frac{S(\Delta\phi, p_T)}{M(\Delta\phi, p_T)} \frac{\int_0^{2\pi} M(\Delta\phi, p_T)}{\int_0^{2\pi} S(\Delta\phi, p_T)}, \tag{4.6}$$

where Q_{PMT} is the charge detected in the PMT and $N_{\text{same event}}^{\text{track}(p_T)-\mathrm{PMT}}$ is the number of track–PMT pairs from the same event. $M(\Delta\phi, p_T)$ is identical to $S(\Delta\phi, p_T)$, except that the two particles in the pair are each taken from different events. This is called the mixed event

technique and it produces a correlation function of order unity. The weighting used accounts for acceptance effects.

The correlation function $C(\Delta\phi, p_T)$ is fit with a Fourier expansion,

$$C(\Delta\phi) = 1 + \sum 2c_n(p_T)\cos(n\Delta\phi), \tag{4.7}$$

in order to extract the Fourier coefficients, c_n.

4.4 Uncertainty Estimation

There are many possible sources of and corrections for uncertainty. Each detector in the PHENIX experiment has sources of background noise, possible physical misalignment, variations in the detector performance with time, and variations in the detector performance between different detector sectors. When possible, background sources are identified and removed. For the remainder, an estimate of their effect is included in the systematic error bars. When possible, correlations between uncertainties are assessed during the process of estimating the magnitude of the uncertainties. Correlations can impact the ways in which uncertainties are combined, and they are important to the statistical analysis which was performed (described in Chapter 6). PHENIX convention is to categorize uncertainties into three types:

1. Type A: point-to-point uncorrelated;
2. Type B: point-to-point correlated;
3. Type C: global scale uncertainties.

As described in Section 4.1, some collision events were excluded from analysis as determined by an algorithm design to identify double interaction events. In addition, a tracking cut was applied to reduce the contribution of particle tracks from background

sources. Systematic uncertainties associated with these cuts were determined by varying the selection criterion and evaluating the corresponding change in the measured v_n.

Two sources of uncertainty corresponding to the calculation of the event plane resolution were included, the inherent statistical uncertainty and a systematic uncertainty estimated by changing the p_T range of central arm tracks used in the calculation.

An uncertainty due to the choice of event plane detector was also included. In most cases, this was determined by comparing the v_n measured using event planes determined by the south beam-beam counter and south forward vertex detector. In d+Au collisions, v_n was additionally calculated using the two-particle correlation method. The specific values of systematic uncertainty assigned were based on a ratio of the v_n values calculated using the two-particle correlation and event plane methods.

As described in Section 3.1, nonflow must be considered. A ratio of correlation functions is taken to an appropriately scaled p+p reference, constructed using minimum bias collisions with the same center-of-mass energy. This method conservatively assumes that any correlations present in these p+p measurements are entirely due to nonflow processes.

The two-particle correlation method described in Section 4.3 was used to perform this estimate. The procedure to extract the c_n coefficients from Equation (4.7) was executed for the system for which nonflow was being evaluated ($p/d/^3$He+Au) and for the p+p reference. The nonflow contribution to the correlations, which was treated as a systematic uncertainty, was directly evaluated from the ratio of the c_n terms,

$$\text{nonflow ratio} = \frac{c_n^{p+p}(p_T)\frac{\langle Q^{p+p}\rangle}{\langle Q^{\text{system}}\rangle}}{c_n^{\text{system}}(p_T)} \tag{4.8}$$

where differences in multiplicity were accounted for through a term dependent on $\langle Q\rangle$, the corresponding average beam-beam counter charge. The assumption used to justify this scaling is that the nonflow processes being estimated by the p+p correlations also occur in the system being compared to at a rate proportional to (diluted by) the number of nucleon-

		$n=2$		
Source	Type	p+Au	d+Au	^{3}He+Au
Track background	B	$\pm 2\%$	$\pm 2\%$	$\pm 2\%$
Event selection	B	$+4\%$	$\pm 1\%$	$\pm 5\%$
$R(\psi_2)$	C	$\pm 3\%$	$\pm 0.3\%$	n/a
ψ_2 determination	B		$\pm 2.5\%$	$\pm 5\%$
Detector alignment	B	$\pm 5\%$	$\pm < 1\%$	$\pm 2\%$
Nonflow (p_T dependent)	B	$-12\% \rightarrow -23\%$	$-5\% \rightarrow -14\%$	$-3\% \rightarrow -7\%$
Combined		$^{+7\%}_{-13.5\%} \rightarrow ^{+7\%}_{-24\%}$	$^{+3\%}_{-6\%} \rightarrow ^{+3\%}_{-14\%}$	$^{+7.5\%}_{-8\%} \rightarrow ^{+7.5\%}_{-10\%}$

		$n=3$		
Source	Type	p+Au	d+Au	^{3}He+Au
Track background	B	$\pm 4\%$	$\pm 7\%$	$\pm 5\%$
Event selection	B	$\pm 3\%$	$\pm 2\%$	$\pm 5\%$
$R(\psi_3)$ (sys.)	C	$\pm 7\%$	$\pm 34\%$	n/a
$R(\psi_3)$ (stat.)	C	$\pm 13\%$	$\pm 17\%$	n/a
ψ_3 determination	B	$< 1\%$	$\pm 17\%$	$\pm 15\%$
Detector alignment	B	$\pm 8\%$	$\pm 5\%$	$\pm 15\%$
Nonflow (p_T dependent)	B	$+21\% \rightarrow +114\%$	$+18\% \rightarrow +27\%$	$+4\% \rightarrow +15\%$
Combined		$^{+27\%}_{-18\%} \rightarrow ^{+115\%}_{-18\%}$	$^{+46\%}_{-42\%} \rightarrow ^{+50\%}_{-42\%}$	$^{+23\%}_{-22\%} \rightarrow ^{+27\%}_{-22\%}$

Table 4.1: Systematic uncertainties in the v_n measurements as a function of p_T in 0-5% central $p/d/^3$He+Au collisions at $\sqrt{s_{NN}}$ = 200 GeV [2, 3, 4, 5, 6].

nucleon collisions, as estimated by $\langle Q \rangle$. If there is no nonflow contribution, then $c_n^{p+p} = 0$ and the nonflow ratio equals zero; if all correlations in the system come from elementary processes, then the absolute value of the scaled c_n^{p+p} equals $|c_n^{\text{system}}|$ and the absolute value of the ratio equals unity.

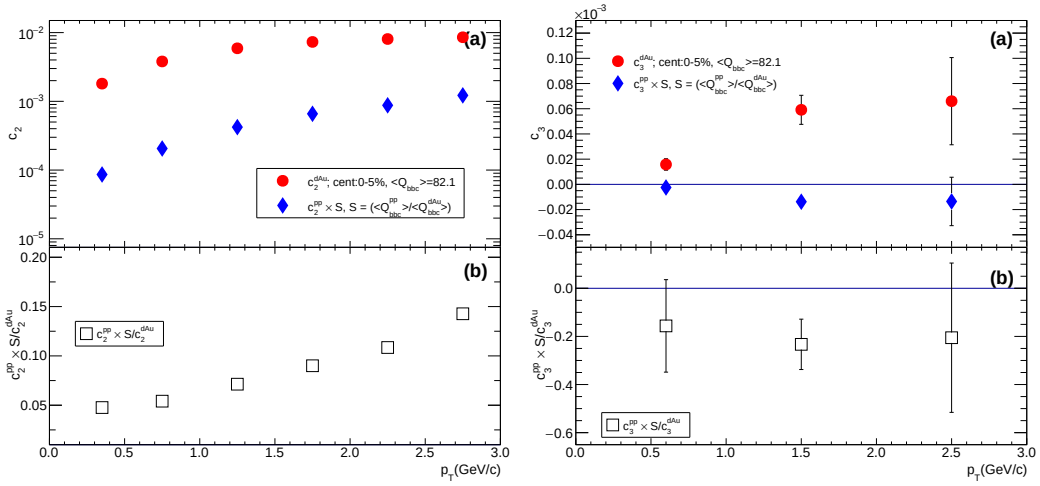

Figure 4.2: Second and third order measurements of correlation coefficients, c_n, and scaled ratios, $c_n^{pp} S / c_n^{dAu}$, for central (0-5%) d+Au collisions at $\sqrt{s_{NN}}$ = 200 GeV. Nonflow estimates are determined by the ratios. The multiplicity scale factor, S, is equal to $\langle Q_{p+p} \rangle / \langle Q_{d+Au} \rangle$ where $\langle Q_{p+p} \rangle = 5.02$ and $\langle Q_{d+Au} \rangle = 82.1$.

Figure 4.2 shows $c_n(p_T)$ for p+p and d+Au collisions at $\sqrt{s_{NN}}$ = 200 GeV as well as the ratio described in Equation (4.8). The second order measurement shown on the left side of Figure 4.2 has a positive value for the ratio indicating that nonflow contributions cause an enhancement in the v_2. As such, a p_T dependent systematic uncertainty corresponding to the deviation of the ratio from zero is applied only to the lower systematic error bar of $v_2(p_T)$. In contrast, the third order measurement shown on the right side of Figure 4.2 has a negative ratio indicating that the nonflow contribution decreases the amplitude of the measured v_3. As such, the uncertainty is applied only to the upper systematic error bars of $v_3(p_T)$. This is the only asymmetric contribution to the systematic uncertainties in this measurement. The nonflow estimates for p+Au and ^{3}He+Au collisions, published in Refs. [3, 42, 2], show the same anticorrelation between the nonflow contribution to the second and third harmonics.

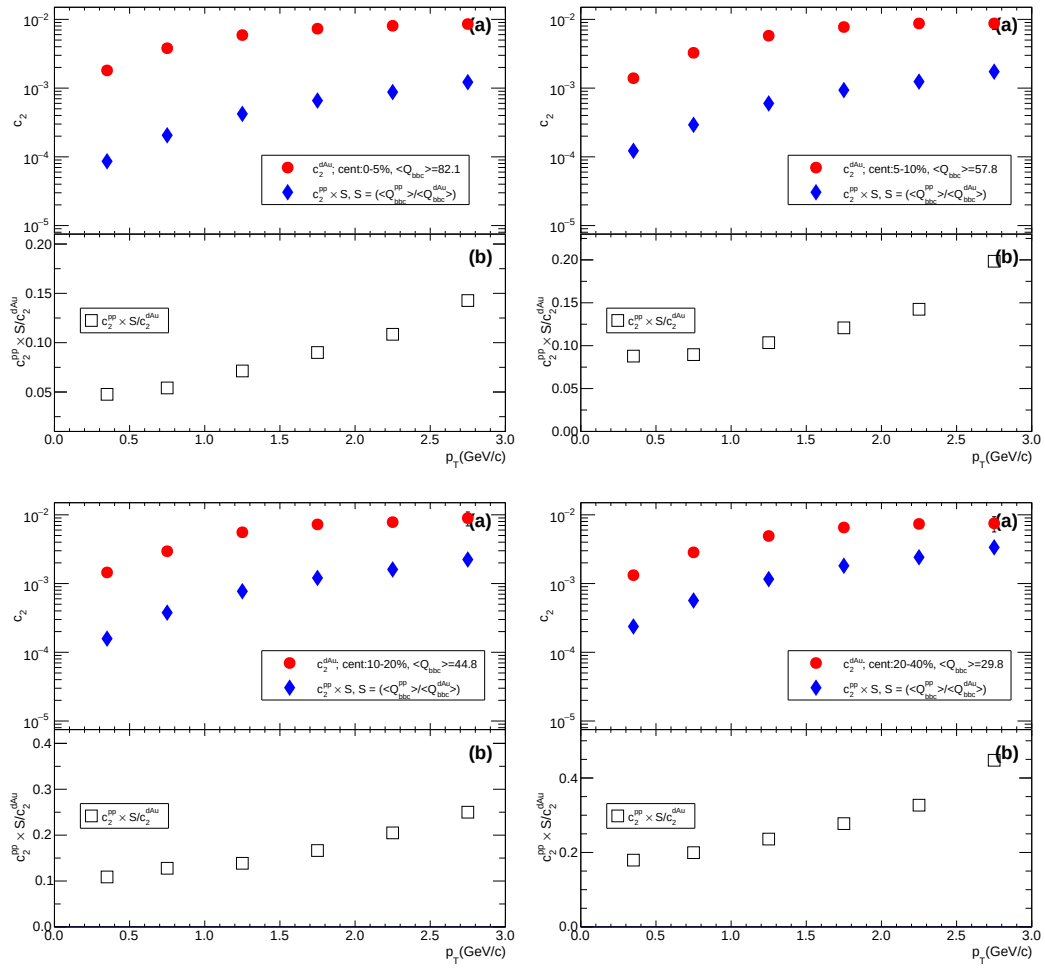

Figure 4.3: Second order measurements of correlation coefficients, c_n, and scaled ratios, $c_n^{pp}S/c_n^{dAu}$, for four centralities of d+Au collisions at $\sqrt{s_{NN}}$ = 200 GeV. The centrality bins shown are (top, left) 0-5%, (top, right) 5-10%, (bottom, left) 10-20%, and (bottom, right) 20-40%. Nonflow estimates are determined by the ratios. The multiplicity scale factor, S, is equal to $\langle Q_{p+p}\rangle/\langle Q_{d+Au}\rangle$ where $\langle Q_{p+p}\rangle = 5.02$ and $\langle Q_{d+Au}\rangle = 82.1$, 57.8, 44.8, and 29.8 for the different centrality bins going from most to least central.

Several additional centrality bins are shown in Figure 4.3. The nonflow contribution systematically increases as the selection becomes more peripheral.

A summary of the values assigned for each type of systematic uncertainty associated with v_2 and v_3 measurements in $p/d/^3$He+Au collisions with $\sqrt{s_{NN}}$ = 200 GeV is given in Table 4.1.

Chapter 5

Small-Systems Geometry Scan

This chapter presents PHENIX measurements of $v_2(p_T)$ and $v_3(p_T)$ in $p/d/^3$He+Au collisions at $\sqrt{s_{NN}} = 200$ GeV. These analyses were the combined effort of many individuals over many years; leading up to this,

- $v_2(p_T)$ and $v_3(p_T)$ in ^{3}He+Au collisions were published by PHENIX in 2015 [2],
- $v_2(p_T)$ in p+Au collisions was published by PHENIX in 2017 [3],
- $v_2(p_T)$ in d+Au collisions was published by PHENIX as two independent results in 2015 [4] and 2017 [5].

This chapter details the combination of these results, with the addition of $v_3(p_T)$ measured in p+Au and d+Au collisions as published by PHENIX in Ref. [6]. My contribution was primarily to the analysis of the d+Au collision data that was collected by PHENIX in 2016. In addition, I played a significant role in performing a statistical analysis over the combination of all of the described measurements, the results of which are detailed in Chapter 6. The results of the statistical analysis were included in Ref. [6], to which I made significant contributions as co-chair of the Paper Preparation Group.

The small-systems geometry scan at RHIC consisted of three collision species, p+Au, d+Au, and ^{3}He+Au, all run at the same center-of-mass energy per nucleon pair, $\sqrt{s_{NN}} =$ 200 GeV. As introduced in Section 3.2, the primary goal of comparing this set of collisions was to systematically vary the spatial distribution of the initial state in a way that is well understood, on average. This choice of collision systems creates intrinsically circular, elliptic, and triangular initial geometries for p+Au, d+Au, and ^{3}He+Au, respectively. Calculations in the MC-Glauber framework found the initial state eccentricities to have the relationship described in Equation (3.1), visualized in Figure 5.1. This ordering of the ec-

centricities is unique and unambiguous, highlighting the utility of comparing this particular set of small-systems collisions: final state correlations that emerge directly from this initial state anisotropy should mimic this specific ordering.

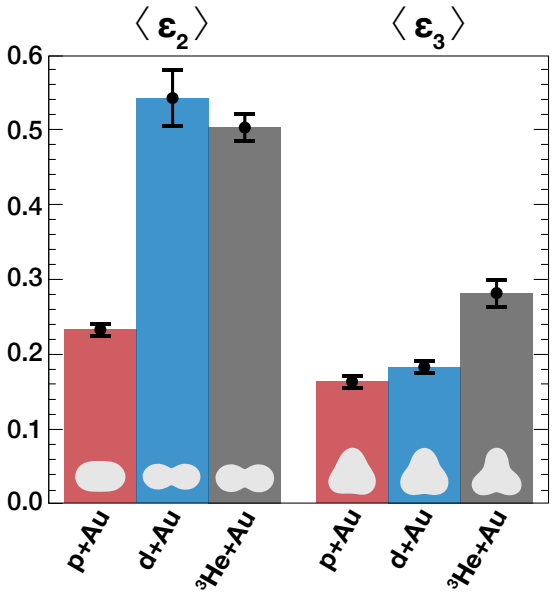

Figure 5.1: Average second (third) order eccentricities, $\langle\varepsilon_2\rangle$ ($\langle\varepsilon_3\rangle$), shown for 0-5% central p+Au (red), d+Au (blue), and ^{3}He+Au (grey) collisions with $\sqrt{s_{NN}}$ = 200 GeV as calculated from a MC-Glauber model using nucleons with Gaussian energy density distributions. The inset shapes represent the geometry associated with the corresponding amplitude and harmonic.

This analysis measures the final state momentum distributions in these collision systems and assesses whether, as is the case in large systems which create quark-gluon plasma, they could have originated from the initial state geometry. The role of the initial state is not yet well understood in collision systems of this size.

A range of theory assumptions have been utilized to calculate how these initial spatial anisotropies may affect the final state momentum distribution being measured. Relativistic viscous hydrodynamical models are most prevalent because they have a history of successfully describing a wide range of observables in A+A collisions. Increasingly, measurements of high multiplicity events in small-system collisions point to the possibility that hydrodynamical models are also the best description in this regime. The results will be compared to calculations from both hydrodynamical and non-hydrodynamical frameworks.

As described in Section 2.4.2, relativistic viscous hydrodynamics calculations efficiently transfer initial state spatial anisotropy into final state momentum anisotropy. With this in mind, a straightforward prediction of hydrodynamical models is that ordering of final state momentum anisotropy between these three systems should exactly follow the eccentricity ordering given in Equation (3.1), that is,

$$\begin{aligned} v_2^{p\text{+Au}} &< v_2^{d\text{+Au}} \approx v_2^{^3\text{He+Au}}, \\ v_3^{p\text{+Au}} &\approx v_3^{d\text{+Au}} < v_3^{^3\text{He+Au}}, \end{aligned} \tag{5.1}$$

where v_2 and v_3 are the second and third order flow coefficients which were introduced in Section 3.1.

Measurements of this observable using the event plane method (Section 4.2) are shown in Figure 5.2. The left panel shows the second harmonic measurement, where v_2 in d+Au and ^{3}He+Au collisions have similar magnitudes, and are much larger than v_2 in p+Au collisions. The right panel shows the third harmonic measurement, where v_3 in p+Au and d+Au collisions have similar magnitudes, and are much smaller than v_3 in ^{3}He+Au collisions. These trends are most distinct at low p_T, where the nonflow contribution is small. This ordering exactly matches the hydrodynamic prediction given in Equation (5.1). This suggests that the initial spatial anisotropy is the primary driver of azimuthal momentum anisotropies in particle emission. A full summary of the systematic uncertainty estimates included in the box errors of Figure 5.2 was given in Table 4.1.

A direct comparison to two hydrodynamical predictions is shown in Figure 5.3. The hydrodynamical models shown are SONIC [19] [1] (which was used to calculate the distributions shown in Figure 2.11) and iEBE-VISHNU [21]. The models are similar in that they

[1] There is some discrepancy between what Ref. [6] refers to as "SONIC " compared to its original definition in Ref. [19]. Historically, SONIC did not implement event-by-event initial condition fluctuations. Figure 2.11, which presents a single event from each collision system, conforms with this original usage. Strictly speaking the "SONIC " calculations shown in Figure 5.3 are superSONIC [20, 43], an event-by-event generalization of SONIC, where the preflow stage has been turned off. What is later referred to as "superSONIC " is the same framework where preflow has been turned on.

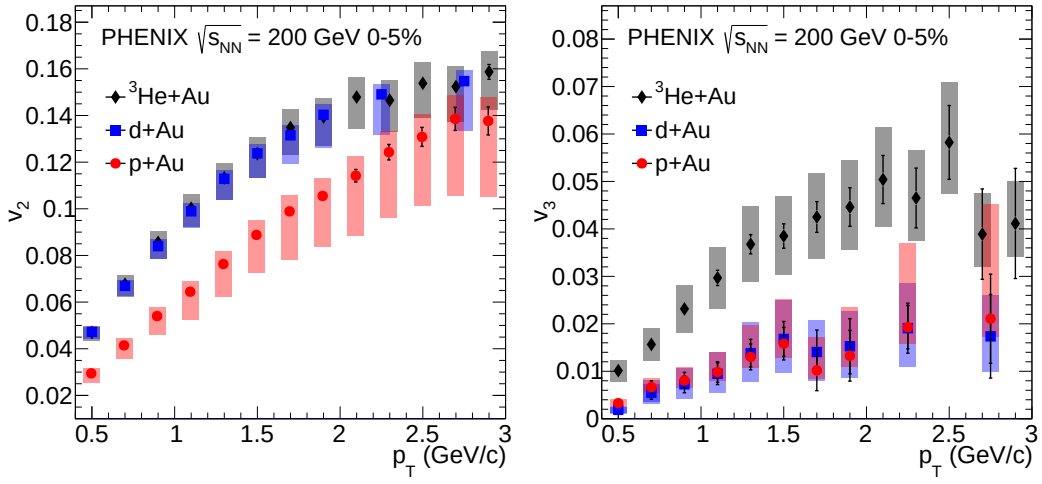

Figure 5.2: Measurements of $v_2(p_T)$ (left) and $v_3(p_T)$ (right) for $p/d/^3$He+Au collisions with $\sqrt{s_{NN}}$ = 200 GeV, depicted as red circles, blue squares, and black diamonds, respectively. Each point represents an average over p_T bins of width 0.2 - 0.5 GeV/c. One standard deviation statistical (systematic) uncertainties are represented as line (box) errors.

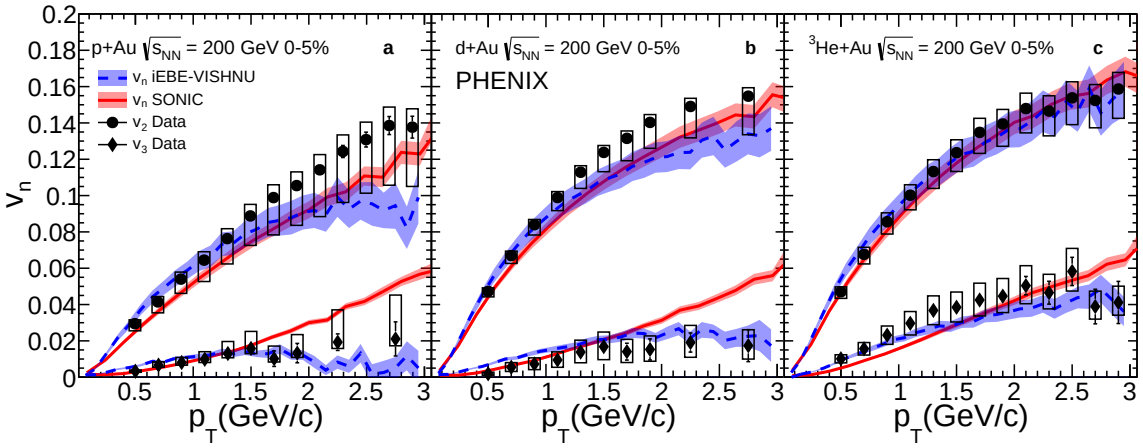

Figure 5.3: Measured $v_2(p_T)$ (black circles) and $v_3(p_T)$ (black diamonds) in (a) p+Au, (b) d+Au, and (c) ^{3}He+Au collisions with $\sqrt{s_{NN}}$ = 200 GeV compared to hydrodynamic predictions of v_n from SONIC (solid red) and iEBE-VISHNU (dashed blue).

both evolve a given set of MC-Glauber initial conditions using viscous hydrodynamics, hadronize the resulting fluid distribution, and then allow hadronic scattering to occur. The key transport parameter, specific shear viscosity (η/s), is set to $0.08 \approx \frac{1}{4\pi}$ in both models, corresponding to the conjectured lower limit in QCD [44]. The differences in the resulting calculations can be attributed to the specific choice of initial conditions and the hadronic

rescattering software, which are different in these models. By eye, both model calculations are consistent with the v_2 measurement and capture the magnitude difference of v_3 compared to v_2 in all three systems.

A closer look at available hydrodynamic calculations offers insight into how specific parts of the system evolution contribute to the azimuthal anisotropy measured in the final state momentum distribution. Figure 5.4 shows the iEBE-VISHNU calculations compared to calculations run using the same code, where no hadronic rescattering stage has been implemented [21]. The observed difference suggests that hadronic rescattering does not substantially change low p_T correlations, but produces some enhancement of high p_T correlations that brings the calculations closer to the measured magnitude.

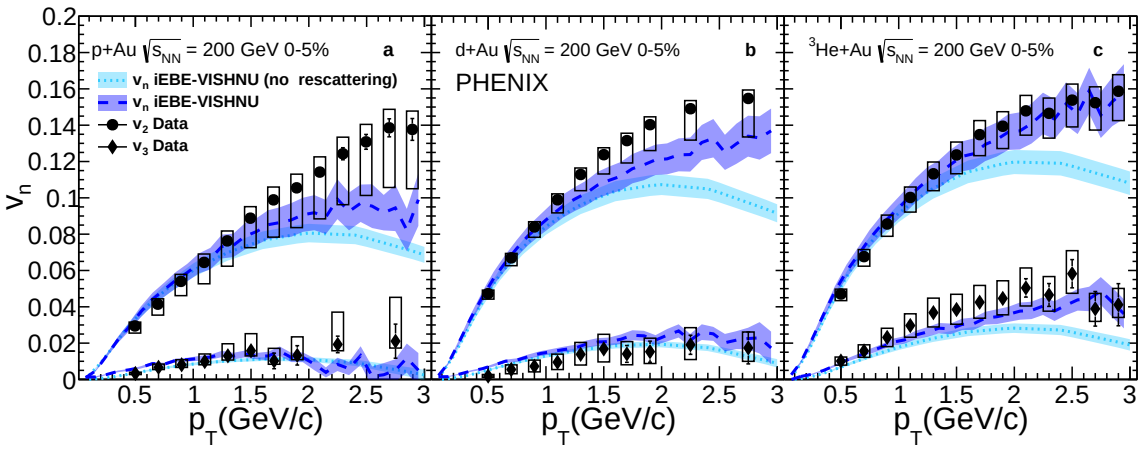

Figure 5.4: Measured $v_2(p_T)$ (black circles) and $v_3(p_T)$ (black diamonds) in (a) p+Au, (b) d+Au, and (c) ^{3}He+Au collisions with $\sqrt{s_{NN}}$ = 200 GeV compared to hydrodynamic predictions of v_n from iEBE-VISHNU with (blue, dashed) and without (cyan, dotted) hadronic rescattering.

Figure 5.5 compares the SONIC calculations to hydrodynamical model superSONIC, which includes an additional stage in the beginning of the system evolution that models pre-equilibrium dynamics. The affect of this stage appears most substantial in the $v_3(p_T)$ calculations causing superSONIC to significantly overestimate v_3 in p+Au and d+Au collisions. The tendency of superSONIC to overestimate the signal in both v_2 and v_3 (compared to SONIC which tends to underestimate v_2 and overestimate v_3) leads to an overall less

robust simultaneous description of these values, because the uncertainties due to nonflow correlations are in anti-correlated between the second and third flow harmonic. This is discussed in greater detail in Chapter 6.

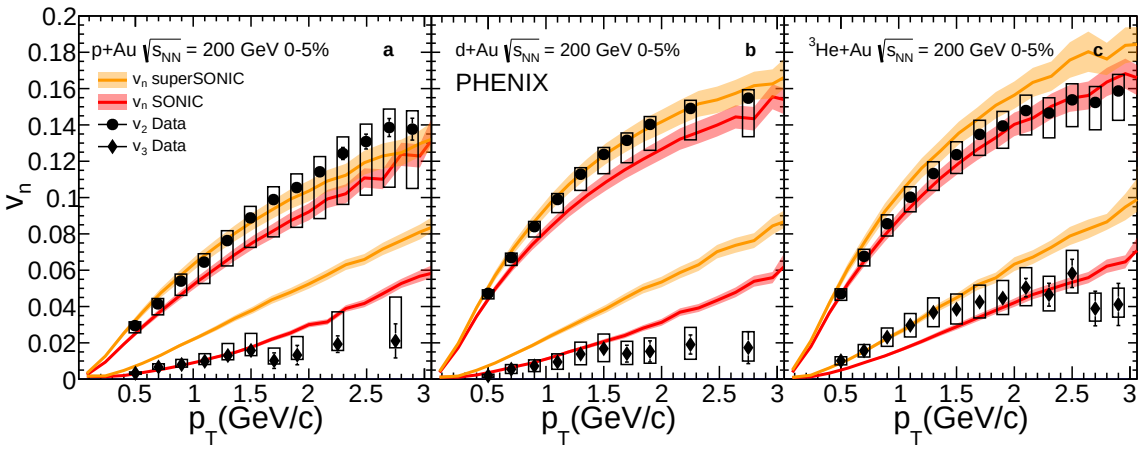

Figure 5.5: Measured $v_2(p_T)$ (black circles) and $v_3(p_T)$ (black diamonds) in (a) p+Au, (b) d+Au, and (c) ^{3}He+Au collisions with $\sqrt{s_{NN}}$ = 200 GeV compared to hydrodynamic predictions of v_n from SONIC (solid red) and superSONIC (solid orange).

While so far only hydrodynamical predictions have been discussed, calculations from models based on other theory frameworks can be similarly evaluated. MSTV is a model which utilizes the initial state momentum domain framework described in Section 2.4.1. In these calculations, the primary mechanism driving azimuthal anisotropy in the final state momentum distribution is anisotropy in the initial state momentum distribution [14]. As discussed in Section 2.4.1, this prescription predicts that

$$v_n^{p\text{+Au}} > v_n^{d\text{+Au}} > v_n^{^3\text{He+Au}}, \tag{5.2}$$

which is exactly opposite to the ordering seen in the measurement (Figure 5.2). An MSTV postdiction of the gluon correlations (which represent a maximum value, as hadronic processes would be expected to dilute the signal) is compared to the data in Figure 5.6, which

shows that these calculations are not consistent with the measurement[2]. These results eliminate the viability of initial state momentum correlations as the dominant mechanism driving small-systems collectivity. An overview of the open questions regarding these calculations was given in Ref. [45], which additionally includes calculations from an independent color saturation model called IP-JAZMA. This study shows that key features of the MSTV calculations actually come from parts of the calculation that are outside the color-glass condensate framework. For additional comparison, a direct test of an MSTV prediction is discussed in Chapter 7.

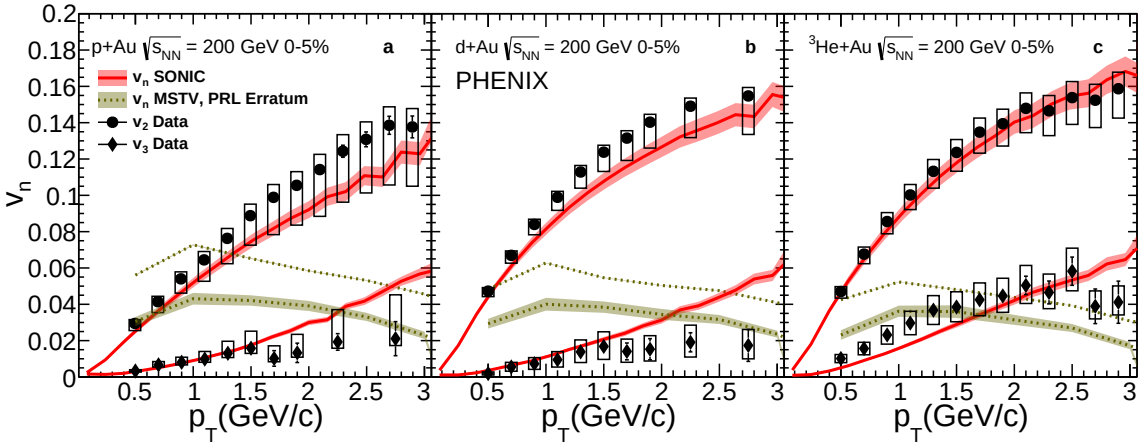

Figure 5.6: Measured $v_2(p_T)$ (black circles) and $v_3(p_T)$ (black diamonds) in (a) p+Au, (b) d+Au, and (c) ^{3}He+Au collisions with $\sqrt{s_{NN}}$ = 200 GeV compared to a prediction from SONIC (solid red) and a postdiction from MSTV (dotted brown).

Finally, a partonic cascade model is considered. As introduced in Section 2.4.2, these models implement a microscopic evolution of the system driven by parton-parton scattering. Like hydrodynamical models, this framework is dependent on initial state geometry, but in this case the mechanism driving translation is parton escape probabilities that are dependent on geometry. Figure 5.7 shows predictions from A Multi-Phase Transport (AMPT) model which demonstrates modest agreement with the measurement at low p_T, but not at high p_T. The AMPT curves used here were taken from Ref. [46], where v_2 and v_3 are cal-

[2]The main PHENIX publication of these results (Ref. [6]) showed a different MSTV comparison; however, recently MSTV have published an erratum amending errors in their initial results. The comparison shown here reflects the most recent MSTV calculations.

culated relative to the initial participant nucleon plane (see Section 3.1), utilizing a *string melting* mechanism and a parton interaction cross section of $\sigma = 1.5$ mb. A cautionary consideration when interpreting AMPT calculations is that the framework has not demonstrated the ability to describe small systems and large systems simultaneously, using a single set of transport parameters.

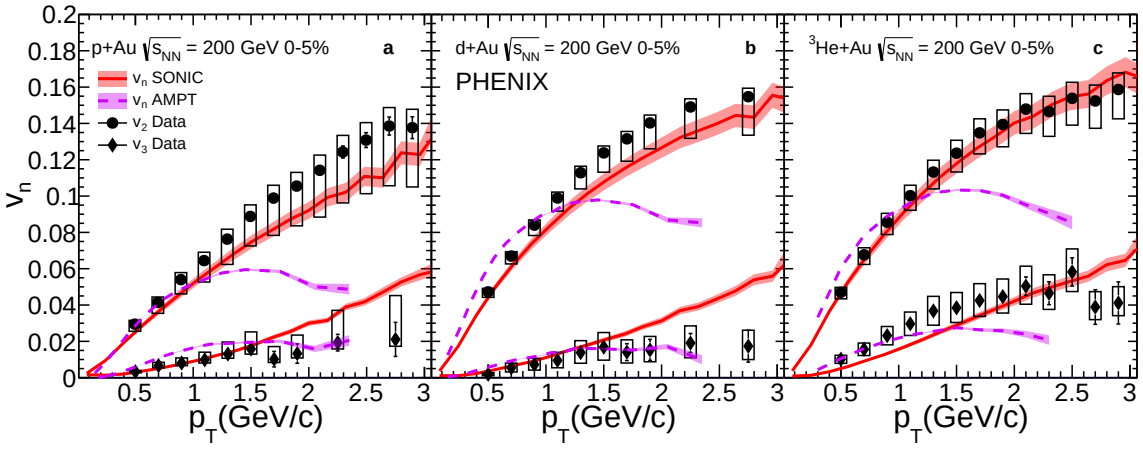

Figure 5.7: Measured $v_2(p_T)$ (black circles) and $v_3(p_T)$ (black diamonds) in (a) p+Au, (b) d+Au, and (c) ^{3}He+Au collisions with $\sqrt{s_{NN}}$ = 200 GeV compared to predictions from SONIC (solid red) and AMPT (dashed magenta).

Six model calculations have been discussed, all shown together in Figure 5.8. In order to objectively compare the ability of the many available model calculations to describe all six measurements simultaneously, a method of quantitative assessment should be employed. As such, Chapter 6 provides a statistical analysis of this comparison.

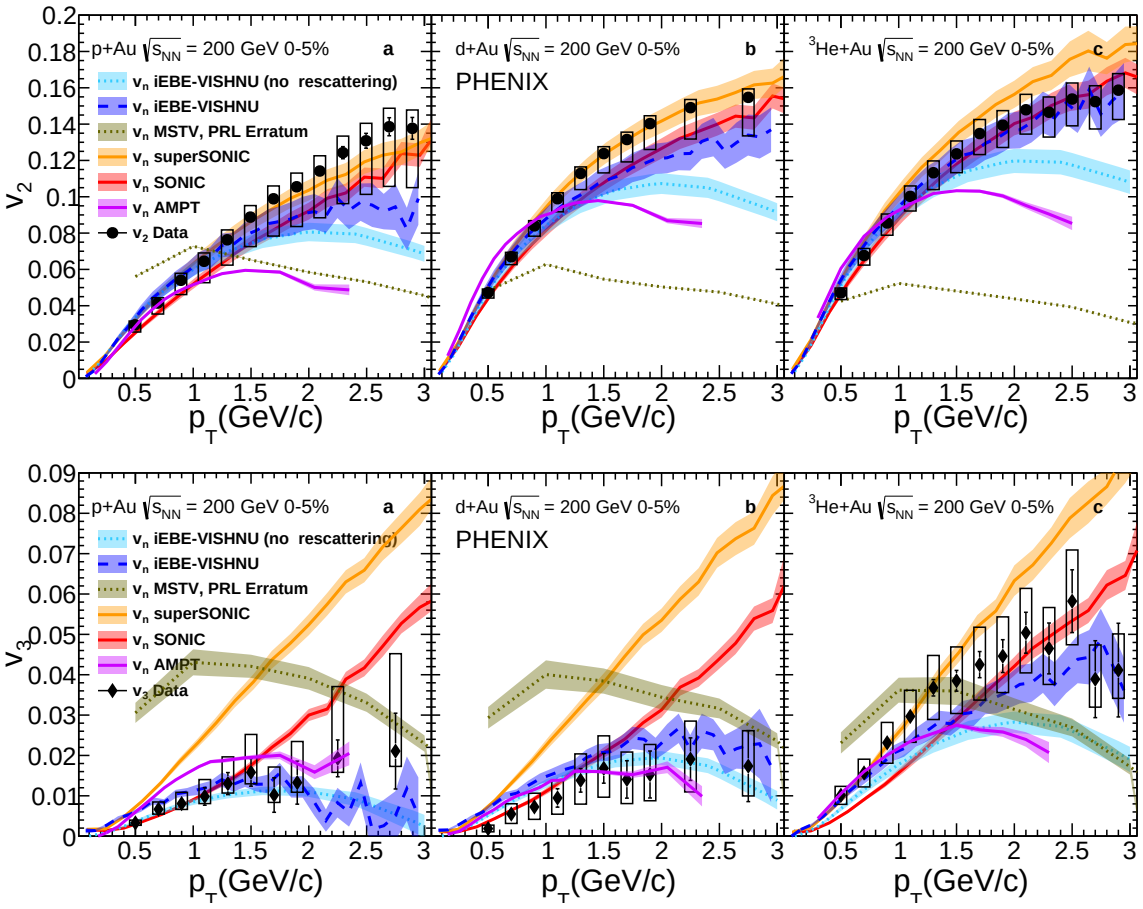

Figure 5.8: Measured (top) $v_2(p_T)$ and (bottom) $v_3(p_T)$ in (a) p+Au, (b) d+Au, and (c) ^{3}He+Au collisions compared to six models. Hydrodynamic predictions of v_n are shown for SONIC (solid red), iEBE-VISHNU with (dashed blue) and without (dotted cyan) hadronic rescattering, and superSONIC (solid orange). Parton cascade predictions are shown from AMPT (dashed magenta), and and momentum domain postdictions are shown from MSTV (dotted brown).

Chapter 6

Statistical Analysis of Data to Model Agreement

The results presented in Chapter 5 provide the best model constraints when requiring that a theory calculation describes not just each measurement individually, but all six measurements, $v_2(p_T)$ and $v_3(p_T)$ in p+Au, d+Au, and ^{3}He+Au collisions, simultaneously. Visual assessment was used in Chapter 5 to identify that the MSTV and AMPT calculations are clear outliers in their inability to describe the data, but an objective assessment of the relative strength of the three hydrodynamical calculations shown requires a quantitative approach. As such, a statistical analysis in the form of a p-value calculation from a modified χ^2 minimization was employed. Sections 6.1 to 6.4 provide a detailed description of the steps used to perform this calculation, and Section 6.5 describes the results.

6.1 Overview of Reduced $\tilde{\chi}^2$ and p-value Calculation

The purpose of this procedure is to take a measurement with an associated statistical and systematic uncertainty and a theory calculation of the measured observable with its own associated uncertainty and calculate a numerical value that reflects the degree to which they agree. This study extracts a p-value with some magnitude between zero and one, with one representing perfect agreement between data and theory.

The p-value calculation used in this analysis is calculated using the minimized $\tilde{\chi}^2$ and the number of degrees of freedom. The $\tilde{\chi}^2$ calculation uses the difference in the nominal values of the measurement compared to the theory, while also accounting for the cited uncertainties. A $\tilde{\chi}^2$ minimization procedure was performed for each data to model comparison. The calculation was done once for each measurement that makes up the data – $v_2(p_T)$ and $v_3(p_T)$ in p+Au, d+Au, and ^{3}He+Au – with some interdependencies between the v_2 and v_3 calculations performed for a given collision system.

The $\tilde{\chi}^2$ minimization procedure scales and tilts the data and theory curves by amounts determined by the allowed parameter space, identifying what minimum change can be made to create maximum agreement. These parameters are additionally applied as penalties to $\tilde{\chi}^2$, so moving the curves by some number of standard deviations would decrease the $\tilde{\chi}^2$ value only if doing so creates data to model agreement to a degree that exceeds the corresponding penalty. The minimum $\tilde{\chi}^2$ was found by systematically calculating $\tilde{\chi}^2$ for all specified parameter combinations (Table 6.1). After all parameter combinations have been tested, the set of parameters corresponding to the smallest value of $\tilde{\chi}^2$ were retained. As such, this procedure provides a set of parameters that maximize the data to model agreement while moving the points as little as possible, and a $\tilde{\chi}^2$ value that can be used to calculate an associated p-value.

For this analysis, measurements of the flow coefficients, v_n, as a function of transverse momentum, p_T, were considered. This procedure uses the symbol $v_n(i)$, to refer to the measurement of the n-th order flow coefficient in p_T bin i. These data have a measured statistical uncertainty, $\sigma^{stat}(i)$, and an estimated systematic uncertainty. For these data, the systematic uncertainty was split into two parts, the nonflow contribution, $\sigma^{nf}(i)$, and all remaining systematic uncertainty, $\sigma^{sys}(i)$. Typically the total systematic error quoted is the combination of these two terms in quadrature ($\sqrt{\sigma^{nf}(i)^2 + \sigma^{sys}(i)^2}$). They are separated in this procedure in order to account for the known anti-correlation between the nonflow uncertainties (σ^{nf}) in v_2 and v_3. As was discussed in Section 4.4, the nonflow uncertainty contributes asymmetrically, namely it systematically reduces the measured v_2 and increases the measured v_3. The covariance matrix for the remaining systematic uncertainty (σ^{sys}) is not determined for the full set of v_2 and v_3 measurements across all collision systems so this lack of knowledge is accounted for by assuming σ^{sys} is divided among three types [1] :

1. Type A: point-to-point uncorrelated uncertainties

2. Type B: point-to-point correlated where the points have a tilt uncertainty

[1] This definition of Type B and C uncertainties is different from conventional PHENIX definitions.

3. Type C: point-to-point correlated where the points all move coherently by a certain standard deviation of σ^{sys}

Fraction parameters (F_A, F_B, F_C) allow the relative contribution of each Types A, B, and C to vary over a range specified in Table 6.1. Note that this introduces only two free parameters, as the total of the three fraction parameters must always equal unity ($F_A + F_B + F_C = 1$). The conservative approach is taken, and these fractions are allowed to vary independently between data sets within reasonable limits.

For a given theory formalism, the calculation that is being compared the measured flow coefficient is denoted as $v_n^{theory}(i)$, representing the n^{th} order flow coefficient calculated in p_T bin i. The uncertainty associated with the theory calculation, $\sigma^{th}(i)$, is treated as one standard deviation. In reality, the uncertainties associated with the theoretical calculations used in this specific comparison indicate some subset of theoretical uncertainties which differ between the models. The full covariance matrices for these uncertainties are not available, so for this calculation we assume that the dominant contribution is a Type C uncertainty, which is correlated between v_2 and v_3. That said, given the relatively small uncertainty bands on the theory calculations, which do not fully represent the theoretical uncertainty, this inclusion has a relatively small effect on $\tilde{\chi}^2$.

$^{Super}_{Sub}$**script**	**Definition**	**Specific Details**
theory	Associated theory calculation	SONIC, superSONIC, iEBE-VISHNU, AMPT, MSTV
n	Associated harmonic order	$n = 2, 3$

Parameter	**Definition**	**Specific Details**
d.o.f	Number of degrees of freedom, equal to the number of data points that went into the calculation	See Table 6.2
F_A, F_B, F_C	Fraction of the systematic uncertainty (without nonflow, σ^{sys}) taken to contribute to types A, B, and C, respectively	$F_A + F_B + F_C = 1$, $F_A \in [0.1, 0.4]$, $F_B, F_C \in [0.1, 0.8]$, steps of 0.1
ε_B, ε_C	Standard deviation parameters associated with Type B and Type C uncertainties, respectively	$\varepsilon_B, \varepsilon_C \in [-4, 4]$, steps of 0.25
ε_{nf}	Standard deviation parameter associated with only the nonflow component of the systematic uncertainty used to implement anti-correlation between the nonflow systematic error of $n = 2$ versus $n = 3$	$\varepsilon_{nf} \in [0, 4]$, steps of 0.25
ε_{th}	Standard deviation parameter associated with the theoretical uncertainty bands	$\varepsilon_{th} \in [-4, 4]$, steps of 0.25
p_{tilt}	The p_T point around which a tilt is applied	$p_{tilt} \in [0.75, 2.75]$, steps of 0.25

Table 6.1: Summary of terms association with $\tilde{\chi}^2$ minimization and p-value calculation.

6.2 Steps to Minimize $\tilde{\chi}^2$ for a Single Data to Model Comparison

For a specified collision system, harmonic, and theory comparison, the steps used to minimize $\tilde{\chi}^2$ are as follows. Each parameter (F_B, F_C, ε_B, ε_C, ε_{nf}, p_{tilt}) is assigned a value corresponding to the lower limit of its specified range. These values are used to calculate the 'new' data point at p_T bin i,

$$v_n(i)' = v_n(i) + \varepsilon_B F_B \sigma^{sys}(i) \left(\frac{p_T(i) - p_{tilt}}{p' - p_{tilt}} \right) + \varepsilon_C F_C \sigma^{sys}(i) \mp \varepsilon_{nf} \sigma^{nf}(i), \tag{6.1}$$

where p' is

$$p'(\mathrm{GeV}/c) = \begin{cases} 0.5, & \text{if } |0.5 - p_{tilt}| > |3.0 - p_{tilt}| \\ 3.0, & \text{otherwise.} \end{cases} \tag{6.2}$$

This calculation takes the measured data points $v_n(i)$ and adds on some value associated with the parts of the systematic uncertainty treated as Types B and C, and the part of the systematic uncertainty corresponding to nonflow. The ε parameters correspond to the number of standard deviations. Larger values of the ε parameters move these 'new' data points further from the measured data points potentially leading to better data to model agreement and a smaller $\tilde{\chi}^2$, but larger values of ε can also increase $\tilde{\chi}^2$ as they will be applied as penalty terms in the calculation of $\tilde{\chi}^2$ (Equation (6.5)).

The fraction of $\sigma^{sys}(i)$ being treated as Type A, point-to-point uncorrelated, is added in quadrature with the statistical uncertainty, $\sigma^{stat}(i)$, yielding

$$\sigma^{stat}(i)' = \sqrt{\sigma^{stat}(i)^2 + (F_A \sigma^{sys}(i))^2}. \tag{6.3}$$

This analysis additionally requires $\sigma^{stat}(i)' \geq 4\%$ which, while ultimately an arbitrary requirement, indicates a lower limit for which the uncertainties are trusted in the comparison. Varying this 4% value has no effect on the relative ordering of the model to data comparisons discussed later, and only effects the overall $\tilde{\chi}^2$ values extracted.

The 'new' theory curves are calculated by treating the theoretical uncertainty, $\sigma^{th}(i)$, as Type C, modulated via the parameter $\varepsilon_{th} \in [-4,4]$. For a given ε_{th} the shifted theory calculation of v_n at p_T bin i is calculated to be

$$v_n^{theory}(i)' = v_n^{theory}(i) + \varepsilon_{th} \sigma^{th}(i). \tag{6.4}$$

Finally, $v_n(i)'$, $\sigma^{stat}(i)'$, $v_n^{theory}(i)'$, and each ε parameter are used to find $\tilde{\chi}^2$,

$$\tilde{\chi}^2 = \varepsilon_B^2 + \varepsilon_C^2 + \varepsilon_{nf}^2 + \varepsilon_{th}^2 + \sum_{i=0}^{N_{pt}} \frac{(v_n(i)' - v_n^{theory}(i)')^2}{\tilde{\sigma}(i)^2} \tag{6.5}$$

where

$$\tilde{\sigma}(i) = \sigma^{stat}(i)' \frac{v_n(i)'}{v_n(i)}. \tag{6.6}$$

Note that Equation (6.5) is a sum over all p_T bins, so Equations (6.1), (6.3), (6.4) and (6.6) are calculated N_{pt} times for each set of parameters.

For each data to model comparison, every possible combination of the parameters F_B, F_C, ε_B, ε_C, ε_{nf}, and p_{tilt} that is within the specified limits is used to calculate $\tilde{\chi}^2$. In principal the parameters are continuous variables, but for computational expediency they are varied over a grid of discrete values defined in Table 6.1. The grid size was analyzed to ensure that a finer grid does not produce substantially different $\tilde{\chi}^2$ values. The smallest value of $\tilde{\chi}^2$ found in this process is then used as the input to the p-value calculation.

6.3 Multiple Data to Model Comparisons Minimized Simultaneously

For completely independent data sets, a combined minimization would simply be the combination of each independent minimization[2]. However, in this case the data being compared to are not all independent – v_2 and v_3 are each extracted from the same data set of collisions. As a result, for each collision system, this calculation constrains the parameter space used for the combined minimization such that the magnitude of the nonflow term is required to be the same for both harmonics. Experimental results indicate that, for a given collision system, nonflow increases (decreases) the measured v_2 (v_3) signal, so ε_{nf} for v_2 of a given collision system is required to be equal in magnitude to that used for v_3, but applied in the opposite direction as indicated by the $\mp$ sign associated with this term in Equation (6.1). Similarly, this analysis assumes that the uncertainty in the theory

[2]Appendix A shows the results of these calculations under this assumption

calculation is correlated between the two harmonics, and ε_{th} for a system is required to be identical for v_2 and v_3. This analysis does not assume there is any correlation between different collision systems.

When calculating the combined $\tilde{\chi}^2$, the penalties associated with these constrained terms (ε_{nf} and ε_{th}) are only applied once per system instead of once for each harmonic,

$$\tilde{\chi}^2 = \varepsilon_{nf}^2 + \varepsilon_{th}^2 + \sum_{n=2}^{3}\left[\varepsilon_{B,n}^2 + \varepsilon_{C,n}^2 + \sum_{i=0}^{N}\frac{(v_n(i)' - v_n^{theory}(i)')^2}{\tilde{\sigma}(i)^2}\right]. \tag{6.7}$$

For each collision system the set of parameters that minimize the combined $\tilde{\chi}^2$ is found. The minimum $\tilde{\chi}^2$ values for each collision system are summed to get the total $\tilde{\chi}^2$ for the given model.

6.4 p-value Calculation from Reduced $\tilde{\chi}^2$

The p-value was calculated from the minimized $\tilde{\chi}^2$ in the standard way, where the number of degrees of freedom (NDOF) is simply the total number of data points (Table 6.2). This analysis utilizes the standard ROOT method `TMath::Prob(min_chisq,NDOF)` [47].

Collision system	Harmonic	Number of data points
p+Au	2	13
	3	10
d+Au	2	10
	3	10
^{3}He+Au	2	13
	3	13

Table 6.2: The number of p_T bins (in the range $p_T \leq 3$ GeV) for v_2 and v_3 in central $p/d/^3$He+Au collisions at $\sqrt{s_{NN}}$ = 200 GeV.

6.5 Results of Statistical Analysis for Small-Systems Geometry Scan

As a reminder of the specific theory calculations that were introduced in Chapter 5, Figures 6.1 and 6.2 show $v_2(p_T)$ and $v_3(p_T)$ in all three systems compared to each model.

Broadly, the hydrodynamical calculations (SONIC, superSONIC, iEBE-VISHNU) do a better job of describing the p_T dependence of the distribution and, therefore, might be expected to be minimized with smaller values of ε_B, which modulates the tilt adjustments in the minimization process. It is also notable that while several theory calculations do a reasonable job describing the magnitude of $v_2(p_T)$ (Figure 6.1), none do nearly as well in describing $v_3(p_T)$ (Figure 6.2). By eye, SONIC provides the best agreement to the v_3 measurements with a very good description of the v_3 values at low p_T in p+Au and d+Au collisions.

Figures 6.3 to 6.5 show how the v_2 and v_3 values may change to achieve a *combined* minimization. As a note, the result can sometimes appear counter intuitive because it may be favorable to make, for example, the v_3 agreement a *little worse* in order to make the v_2 agreement *much better*, with the net effect of decreasing the combined $\tilde{\chi}^2$.

Figure 6.3 shows how the p+Au v_n data points and model calculations are shifted to become closer together in the minimization process for each of the five model comparisons to which this process was applied. For each model, the top panel is $v_2(p_T)$ and the bottom panel is $v_3(p_T)$. The experimental data, $v_n(i)$, are shown as filled blue circles, and the 'new' data points, $v_n(i)'$, are shown as open black circles. As such, the blue circles are identical in each of the five figures shown in Figure 6.3, while the open circles are not the same and may even be drastically different depending on what shift must occur to make the data better agree with the corresponding theory calculation. The original theory curves ($v_n^{theory}(i)$) are shown as dashed black lines, and the 'new' theory curves ($v_n^{theory}(i)'$) are shown as solid orange lines. As was shown in Equation (6.4), $v_n^{theory}(i)'$ is moved by ε_{th} standard deviations. Figure 6.3 can be used to surmise what type of adjustment minimizes $\tilde{\chi}^2$ in v_2 and v_3 in p+Au collisions simultaneously, how it corresponds to the resulting p-values, and how the minimization differs from theory to theory for a given collision system. All of the shifting to create the 'new' data points and 'new' theory curves was done using the inset parameters which are also summarized in Appendix A. Figure 6.4 and Figure 6.5 show the same information for d+Au and ^{3}He+Au collisions, respectively.

A concise summary of the of the extracted values for the minimum $\tilde{\chi}^2$ and the associated p-values is given in Table 6.3.

SONIC provides a very good description of the data with an overall p-value of 0.896. iEBE-VISHNU and superSONIC give a slightly worse overall p-values of 0.138 and 0.281, respectively. Both MSTV and AMPT yield a very poor description with p-values of effectively zero.

	SONIC	iEBE-VISHNU	superSONIC	AMPT	MSTV Erratum
p+Au	0.9659	0.08624	0.2428	2.088E-7	8.331E-182
d+Au	0.689	0.3131	0.2624	1.578E-18	6.11E-88
^{3}He+Au	0.465	0.4317	0.5492	1.558E-22	6.419e-281
	0.8956	0.1389	0.2809	1.943e-43	0

Table 6.3: p-values for combined v_2 and v_3 in $p/d/^3$He+Au collisons. The granularity is 0.25 for ε_b and ε_c; 0.25 for ε_{nf}; 0.25 for ε_{th}; 0.1 for F_b and F_c; and 0.25 for p_{tilt}.

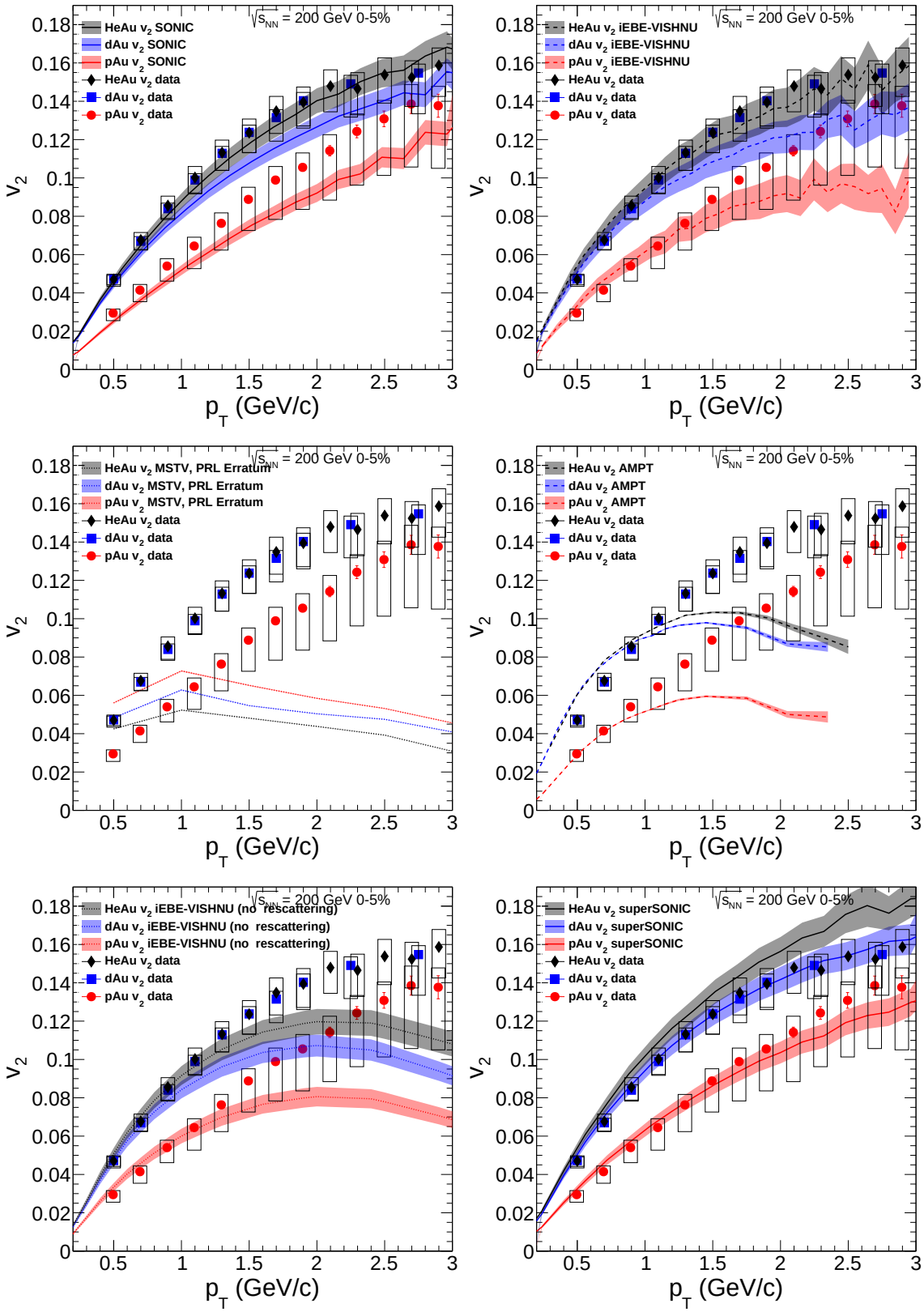

Figure 6.1: Measured $v_2(p_T)$ in $p/d/^3$He+Au collisions compared to six model calculations.

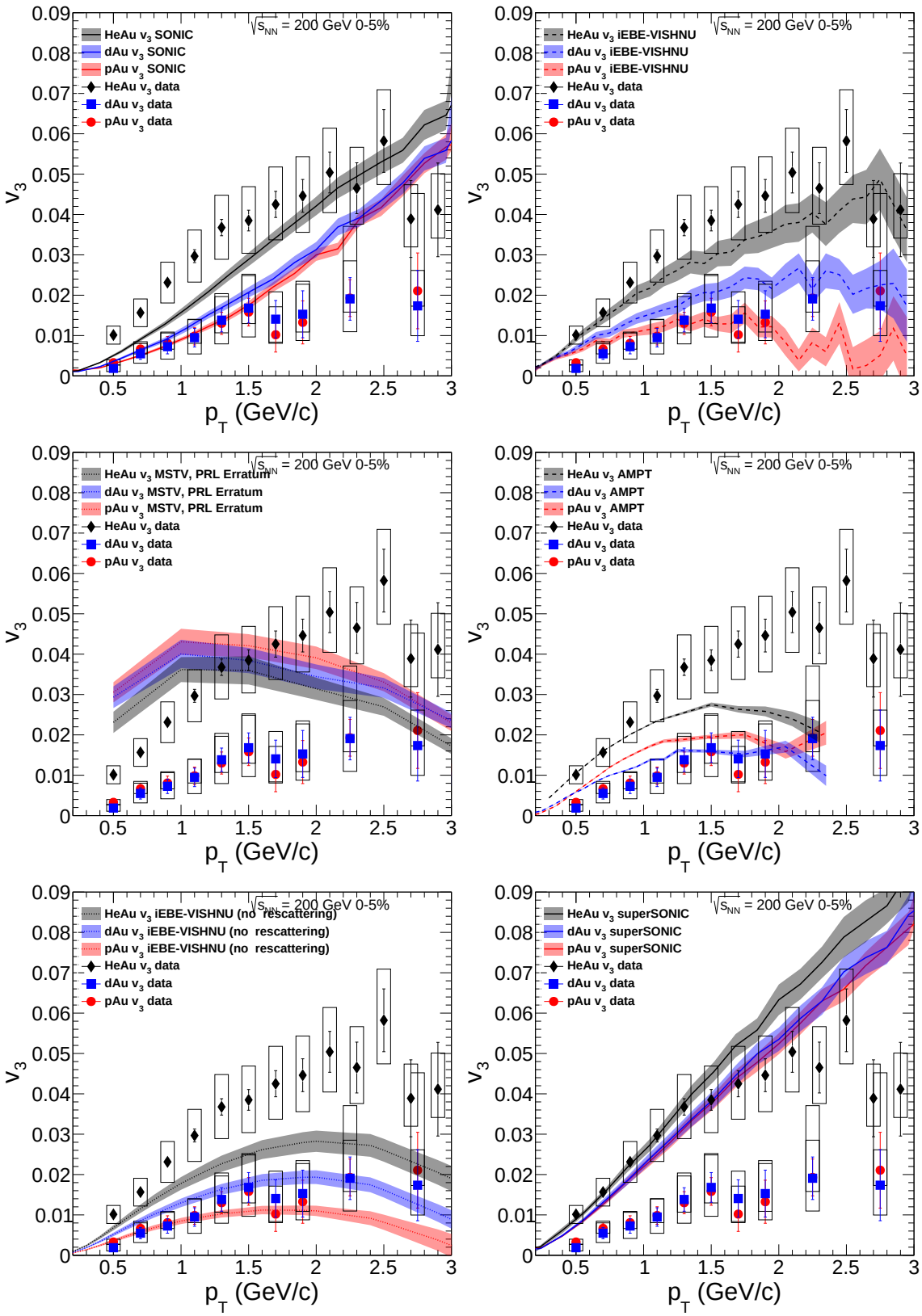

Figure 6.2: Measured $v_3(p_T)$ in $p/d/^3$He+Au collisions compared to six model calculations.

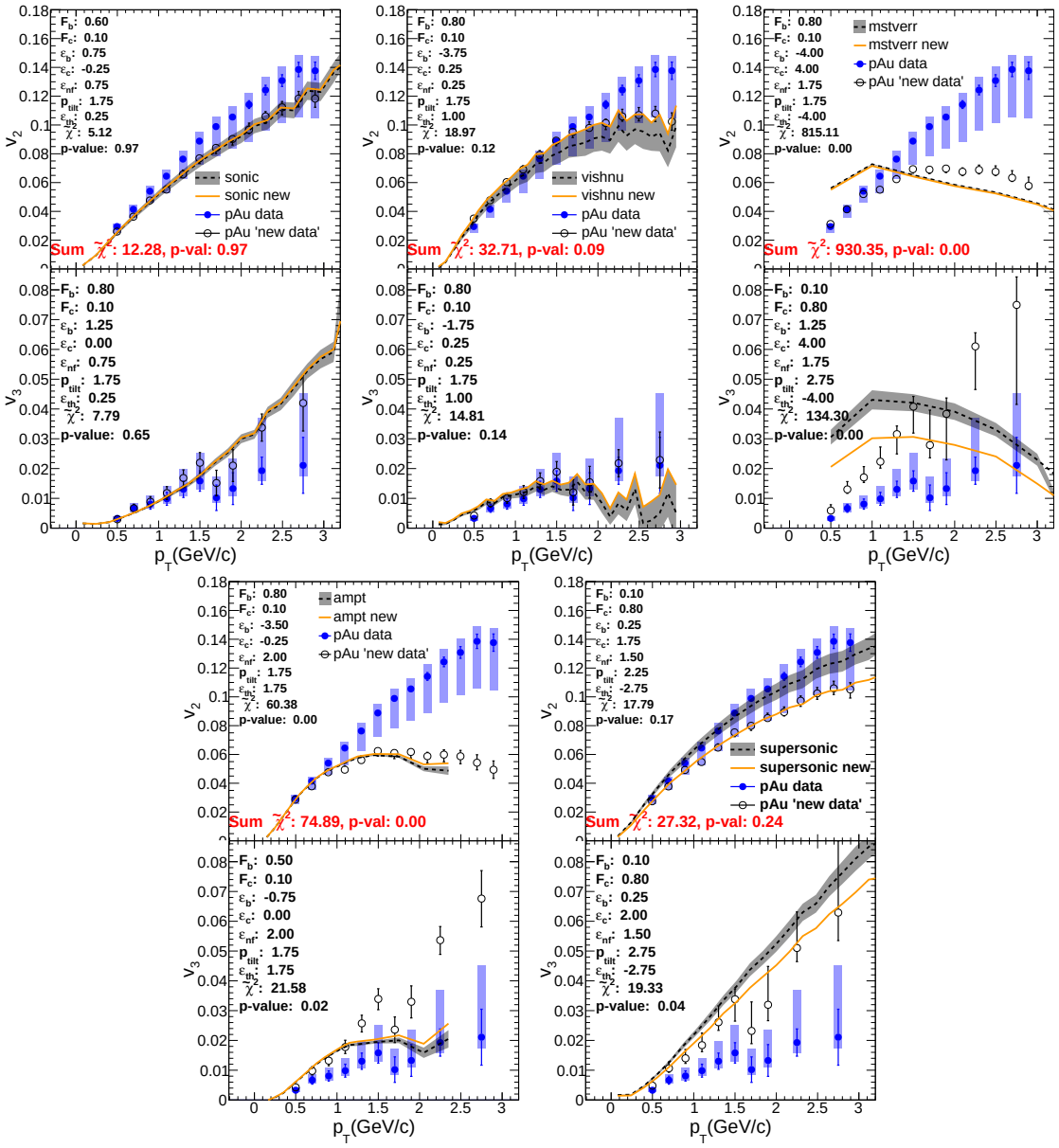

Figure 6.3: Measured and calculated $v_n(p_T)$ in p+Au collisions before and after simultaneous $\tilde{\chi}^2$ minimization

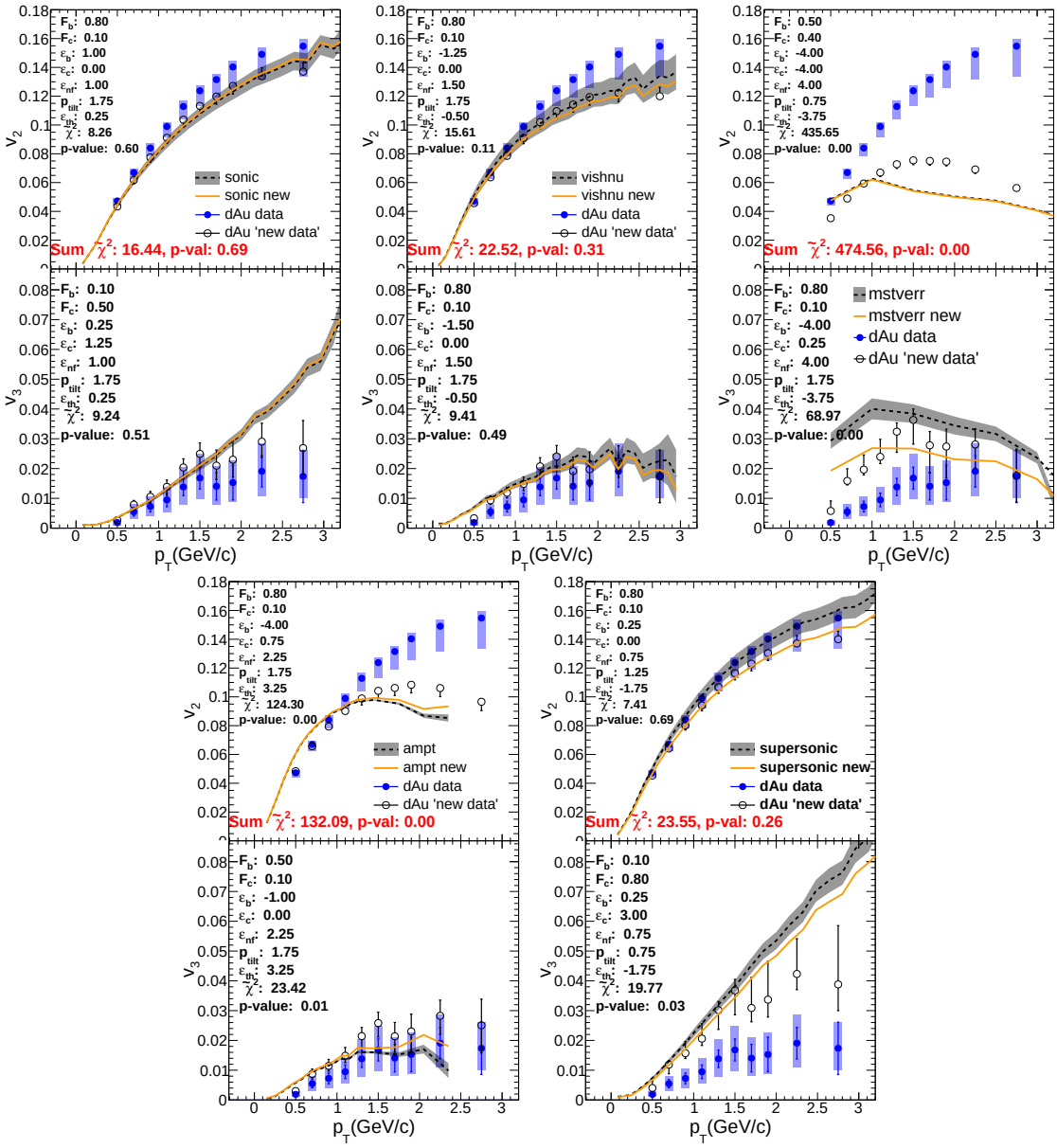

Figure 6.4: Measured and calculated $v_n(p_T)$ in d+Au collisions before and after simultaneous $\tilde{\chi}^2$ minimization

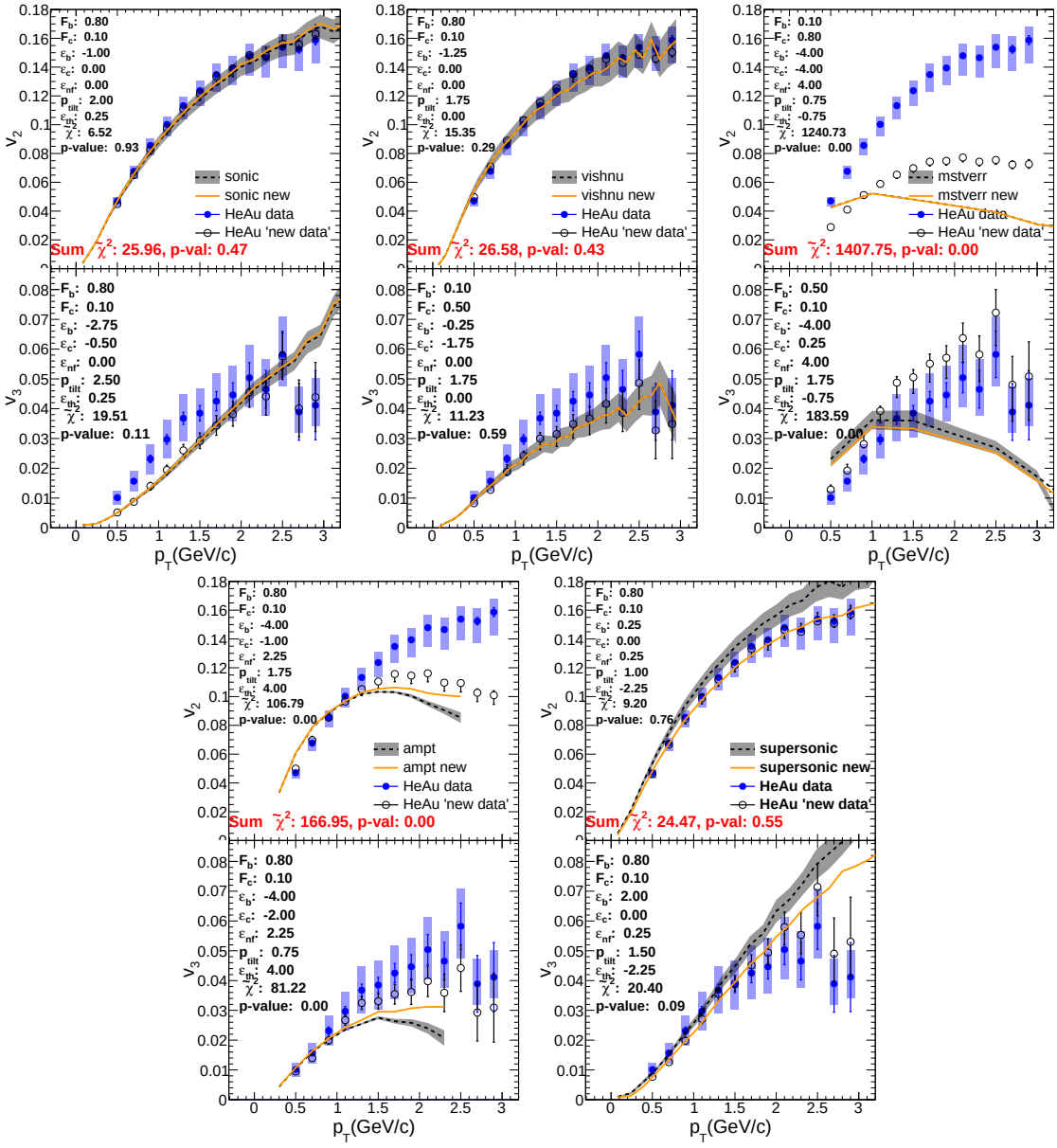

Figure 6.5: Measured and calculated $v_n(p_T)$ in ^{3}He+Au collisions before and after simultaneous $\tilde{\chi}^2$ minimization

Chapter 7

Discussion

Chapter 5 primarily focused on the sensitivity of the flow coefficients, v_n, to the spatial distribution of the system at the time of collision. However, this observable is also known to be sensitive to the multiplicity of the particles produced in the collision. While p+Au, d+Au, and ^{3}He+Au collisions are all considered small systems, there is still a distinct difference in the size of the systems with the projectiles containing one, two, and three nucleons, respectively. This translates to a difference in multiplicities, and for a given centrality class, the average number of participant nucleons in the three systems are

$$\langle N_{part} \rangle^{p\text{+Au}} < \langle N_{part} \rangle^{d\text{+Au}} < \langle N_{part} \rangle^{^3\text{He+Au}}. \tag{7.1}$$

Understanding the relative roles of multiplicity and geometry is important to the interpretation of these results, because some descriptions of the system are more dependent on one or the other. As has been discussed, hydrodynamical models are strongly dependent on initial state geometry, but multiplicity also plays a role in this framework through its relationship to the entropy and pressure of the system. Parton scattering models also have a geometry response, though the underlying physics mechanism is different. On the other hand, calculations of v_n from initial state momentum correlations models such as MSTV supposedly have no geometry dependence.

In an attempt to isolate the contributions of geometry and multiplicity, Section 7.1 takes a closer look at multiplicity differences in $p/d/^3$He+Au. Section 7.2 compares the second harmonic measurements in small systems to published large-system results, which have multiplicities that are up to two orders of magnitude larger. Since the characterization of the initial state geometry is necessarily model dependent, Section 7.3 discusses the assumptions present in the geometry parameters that have been used and considers alter-

native assumptions. Section 7.4 explores the roles of eccentricity and multiplicity in small and large systems for the third harmonic.

7.1 Comparison with Constant Multiplicity

Before the full set of second and third order flow coefficients were extracted, a question was raised as to whether to observed ordering of v_2 measured in $p/d/^3$He+Au collisions (Figure 5.2, a) could be dominated by event multiplicity rather than the initial state geometry [2, 3, 4]. The addition of v_3 measurements paints a picture that exactly follows the expectation of geometry ordering, which is difficult to reconcile with a multiplicity ordering interpretation. This section shows an additional comparison that further solidifies this conclusion.

Figure 7.1 compares p+Au and d+Au collisions in centrality classes that have the same average $dN_{\rm ch}/d\eta$, which is related to multiplicity [1]. As such, it is assumed that the contribution from multiplicity is identical in both measurements. Below $p_T = 1$ GeV/c, where nonflow contribution is smallest, the measurements do not overlap within one standard deviation of the estimated uncertainty. The systematic difference observed between the two systems, therefore, can be attributed to differences in geometry. The ordering of the v_2 values in the two systems, where v_2 is larger in d+Au collisions than in p+Au collisions, is consistent with the interpretation that this difference is the direct result of the more elliptic initial state in d+Au collisions. At higher p_T the uncertainties are large and overlap, and a measurement with smaller uncertainty would be needed to better constrain this relationship. Figure 7.1 additionally shows calculations from both a hydrodynamical model SONIC and a initial state momentum correlations model MSTV. Both models account for system multiplicity, but only SONIC results are affected by initial state eccentricity. The data are

[1] This specific comparison was first motivated by the MSTV prediction that same multiplicity small systems would yield the same v_n and that their calculation of multiplicity matched d+Au and p+Au collisions would be identical [14]. For context, the initial (erroneous) MSTV calculations reasonably described $v_2(p_T)$ in p+Au collisions.

fairly consistent with the SONIC curves, which describe the observed separation between the two systems. The exact magnitude is slightly below the nominal data points for both systems, which can be attributed to the nonflow enhancement in the measurement which is not accounted for in the SONIC calculation. In contrast, the MSTV calculation does not describe the data, and the measurements in the two systems do not fall along a universal curve as MSTV predicted they would. As was discussed in Chapter 5, there are many open questions about how to interpret these MSTV results.

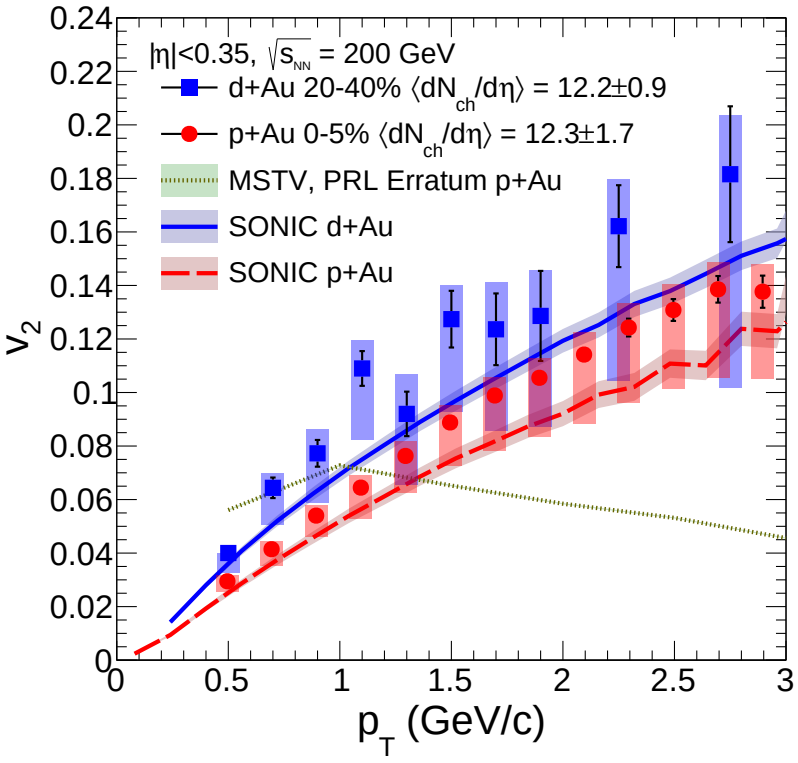

Figure 7.1: Measured v_2 in the 0-5% most central p+Au collisions (red circles) and 20-40% central d+Au collisions (blue squares) compared to corresponding SONIC predictions (red dashed and blue solid, respectively) and MSTV Erratum (brown dotted). The MSTV Erratum calculation is for 0-5% central p+Au collisions, which the authors state yield an identical v_2 to d+Au collisions at the same multiplicity [14]. The vertical lines (boxes) represent one standard deviation statistical (systematic) uncertainties. $dN_{\mathrm{ch}}/d\eta$ values are taken from Ref. [15].

7.2 Comparison of Second Harmonic Flow in Small and Large Systems

As was discussed in Chapter 3, the translation of initial geometry to final state momentum anisotropy as a direct result of the hydrodynamical evolution of a strongly coupled medium has been well established in large systems. One technique for showing the contribution of geometry has been to scale the data by geometry parameters. Many large systems have been found to fall on a universal curve when differences in geometry and multiplicity are accounted for [32, 48]. Under the assumption that the way in which a hydrodynamic system translates initial state spatial anisotropy to final state momentum anisotropy is linear, v_n/ε_n scaling normalizes for geometry contribution, and isolates the multiplicity contribution. When calculating the eccentricity, some assumption must be applied about the energy density of the nucleons. In this case, the calculations for large systems assumed the nucleons were point-like with all of the energy located at the nominal center of each nucleon. This assumption is non-physical, but it has been shown to be a reasonable approximation when the system size is large. For small systems, a more physical approach was taken by assuming the nucleon energy density is Gauss-like [7]. The ability to use the same assumption across all systems was limited by the availability of published data, but some cross checks will be shown that indicate that confirm that the difference between these two assumptions is negligible for the A+A systems shown.

Using PHENIX measurements of v_2 as a function of pseudorapidity, η, and $dN_{\rm ch}/d\eta(\eta)$ [5, 15], an integrated v_2 was extracted for $p/d/^3$He+Au and p+Al collisions at $\sqrt{s_{NN}}$ = 200 GeV and for d+Au collisions at two additional collision energies, $\sqrt{s_{NN}}$ = 62.4 GeV and 39 GeV. All measurements are for the 5% most central events except for the d+Au collisions at $\sqrt{s_{NN}}$ = 39 GeV for which the high centrality bin was expanded to included the 10% most central events in order to improve statistical precision. These results are shown in the left panel of Figure 7.2. The black points show the v_2 for charged particles measured in different collision systems with nucleon-nucleon center-of-mass energy, $\sqrt{s_{NN}}$ = 200 GeV; the magnitude increases with $dN_{\rm ch}/d\eta$. The v_2 results for d+Au collsions at different col-

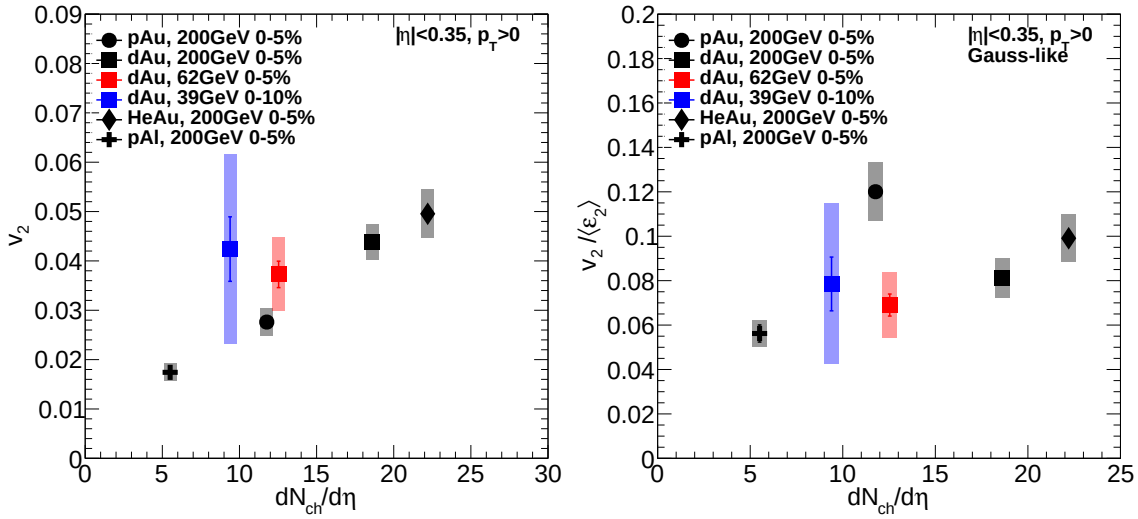

Figure 7.2: Measured $v_2(dN_{\mathrm{ch}}/d\eta)$ (left) and $v_2/\langle\varepsilon_2\rangle(dN_{\mathrm{ch}}/d\eta)$ (right) in $p/d/^3$He+Au and p+Al at $\sqrt{s_{NN}}$ = 200 GeV and d+Au at $\sqrt{s_{NN}}$ = 62.4 GeV and 39 GeV.

lision energies are shown in Figure 7.2 as square markers with different colors. They are measured to have similar magnitudes, though the substantial size of the uncertainties makes it difficult to conclusively interpret their place in the trend.

The right panel of Figure 7.2 shows these data where v_2 has been scaled by the average second order eccentricity, $\langle\varepsilon_2\rangle$, as calculated using a MC-Glauber model. The systematic uncertainties from the geometry parameters were folded into the box error bars. These geometry parameters were calculated with the assumption that the nucleons have a Gaussian energy density distribution. The scaling decreases the dependence of v_2 on $dN_{\mathrm{ch}}/d\eta$, though the distribution is not entirely flat. While it has been well established that eccentricity scaling is dominantly linear in large systems, such that $v_2 \propto \langle\varepsilon_2\rangle$, it is possible that nonlinear terms have a larger contribution in small systems.

These small-system results are shown with comparable large-system results [11, 12] in Figure 7.3. The A+A results appear to line up along a single curve when collision energy is constant. The small-systems results generally line up with the overall trend of the large systems, supporting the interpretation that the mechanism driving v_2 in small systems is the same as that in large systems. As mentioned previously, this is an inherently simplified

scaling relationship, which is not always applicable. It is possible that this is the case for small systems.

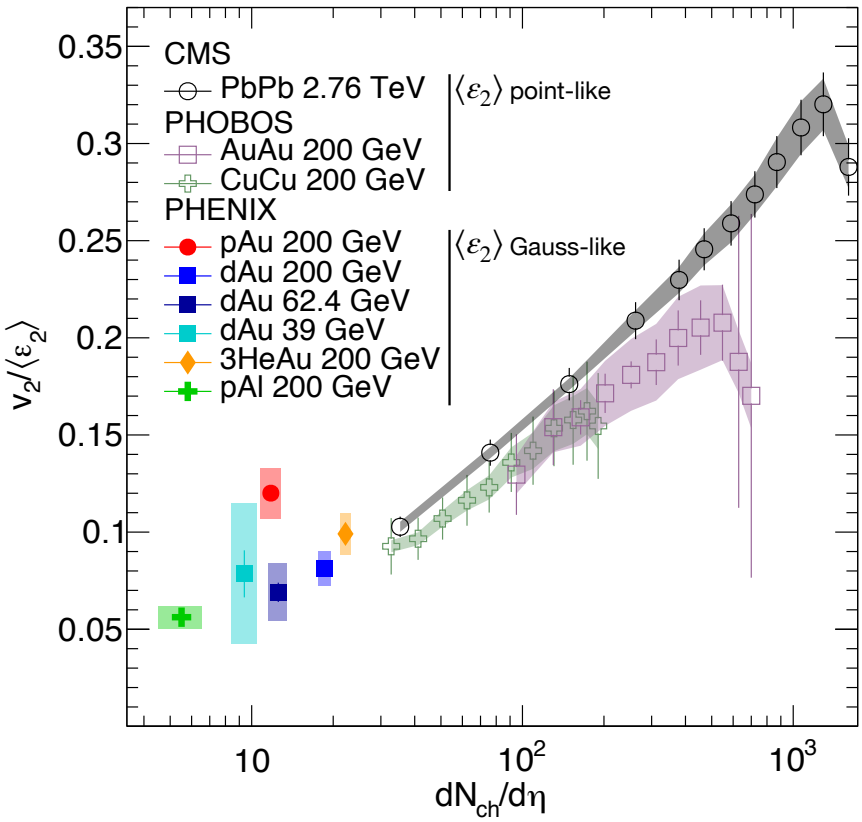

Figure 7.3: Measured $v_2/\langle\varepsilon_2\rangle(dN_{\rm ch}/d\eta)$ in $p/d/^3$He+Au, p+Al, Au+Au, and Cu+Cu collisions at $\sqrt{s_{NN}}$ = 200 GeV, d+Au collisions at $\sqrt{s_{NN}}$ = 62.4 GeV and 39 GeV, and Pb+Pb collisions at $\sqrt{s_{NN}}$ = 2.76 TeV [5, 15, 12, 11]. Eccentricity calculations utilized the point-like (Gauss-like) assumption for large (small) systems.

7.3 Geometry Assumptions

As discussed in Section 2.4.1, initial state models are essential for understanding the evolution of the collision system. Parameters from these models are used to characterize collisions in ways which cannot be done directly through experiment. The initial state parameters used in this dissertation are all from a Monte-Carlo Glauber model, and the specific values used are summarized in Table 7.1. This section will continue to expand on

the value and limitations of these parameters and how that impacts the interpretation of these results.

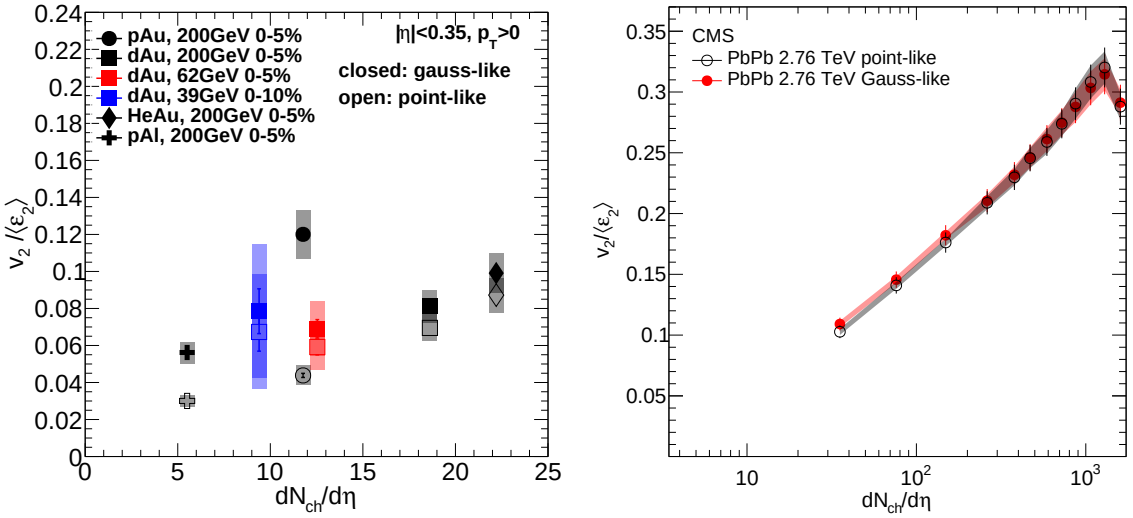

Figure 7.4: $v_2/\langle\varepsilon_2\rangle(dN_{\rm ch}/d\eta)$ in small systems (left) and Pb+Pb (right) with the Gauss-like assumption as closed points and the point-like assumption as open points.

The values quoted so far have used the point-like assumption for large systems and the Gauss-like assumption for small systems, where these types of nucleon energy density distributions were described in Section 7.2. Here the effect of using different assumptions is explored. Figure 7.4 shows how $v_2/\langle\varepsilon_2\rangle(dN_{\rm ch}/d\eta)$ changes in small systems (left) and Pb+Pb (right) when the eccentricity is point-like (open) versus Gauss-like (closed). The effect is substantial in small systems, most notably in p+Au and p+Al. In Pb+Pb the difference is minimal. Figure 7.5 shows the comparison that was given in Figure 7.3 of small and large systems with eccentricity scaling, but where the eccentricities for small systems were calculated using the nonphysical point-like assumption in order to directly match what was done in large systems. In terms of understanding the trend as a whole, the choice of assumption does not make a substantial difference.

More work is needed to determine the best description of the nucleons, so two additional possibilities are considered, disk-like and diskNBD-like [7], as shown in Figure 7.6. The disk-like assumption treats the energy density of the nucleon as uniform across the

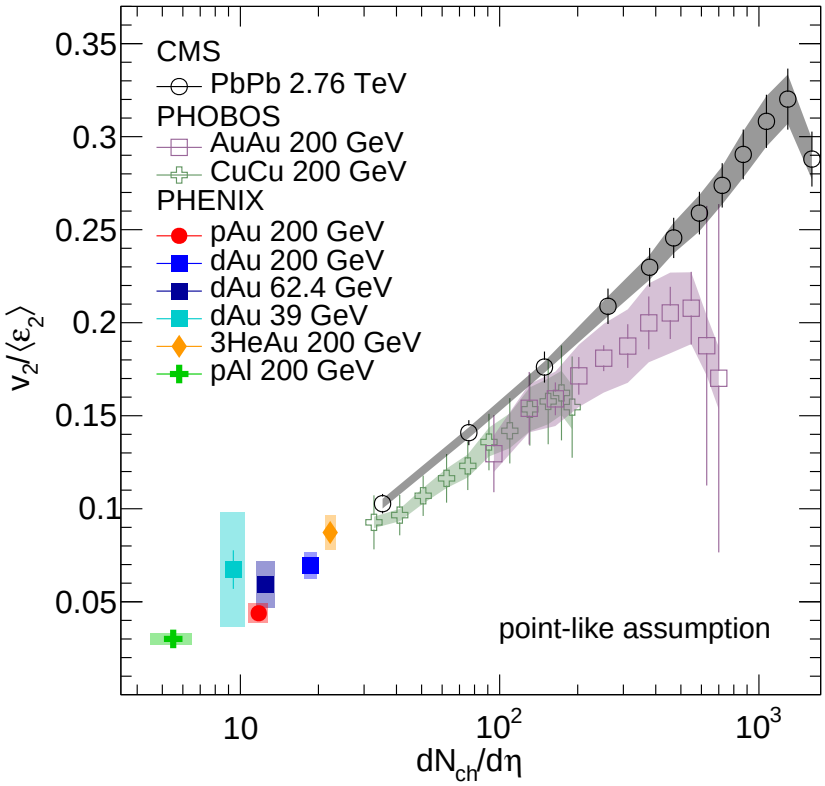

Figure 7.5: Measured $v_2/\langle\varepsilon_2\rangle(dN_{\rm ch}/d\eta)$ in $p/d/^3$He+Au, p+Al, Au+Au, and Cu+Cu collisions at $\sqrt{s_{NN}}$ = 200 GeV, d+Au collisions at $\sqrt{s_{NN}}$ = 62.4 GeV and 39 GeV, and Pb+Pb collisions at $\sqrt{s_{NN}}$ = 2.76 TeV [5, 15, 12, 11]. All eccentricities were calculated using the point-like assumption.

entire nucleon area. The diskNBD-like assumption uses this same treatment of the individual nucleons, but additionally applies a weighting factor to nucleons depending on their relative position in the distribution. This weight is determined from the negative binomial distribution (NBD) fit to the particle multiplicity. Calculations using the disk-like and diskNBD-like assumptions are not substantially different from the Gauss-like assumption.

7.4 Comparison of Third Harmonic Flow in Small and Large Systems

At this point in time, the p_T integrated v_3 have not been measured for $p/d/^3$He+Au collisions, so an alternate approach is taken to investigate the relative contributions of multiplicity and eccentricity to the third harmonic flow. Figure 7.7 shows $v_3(p_T)$ in five colli-

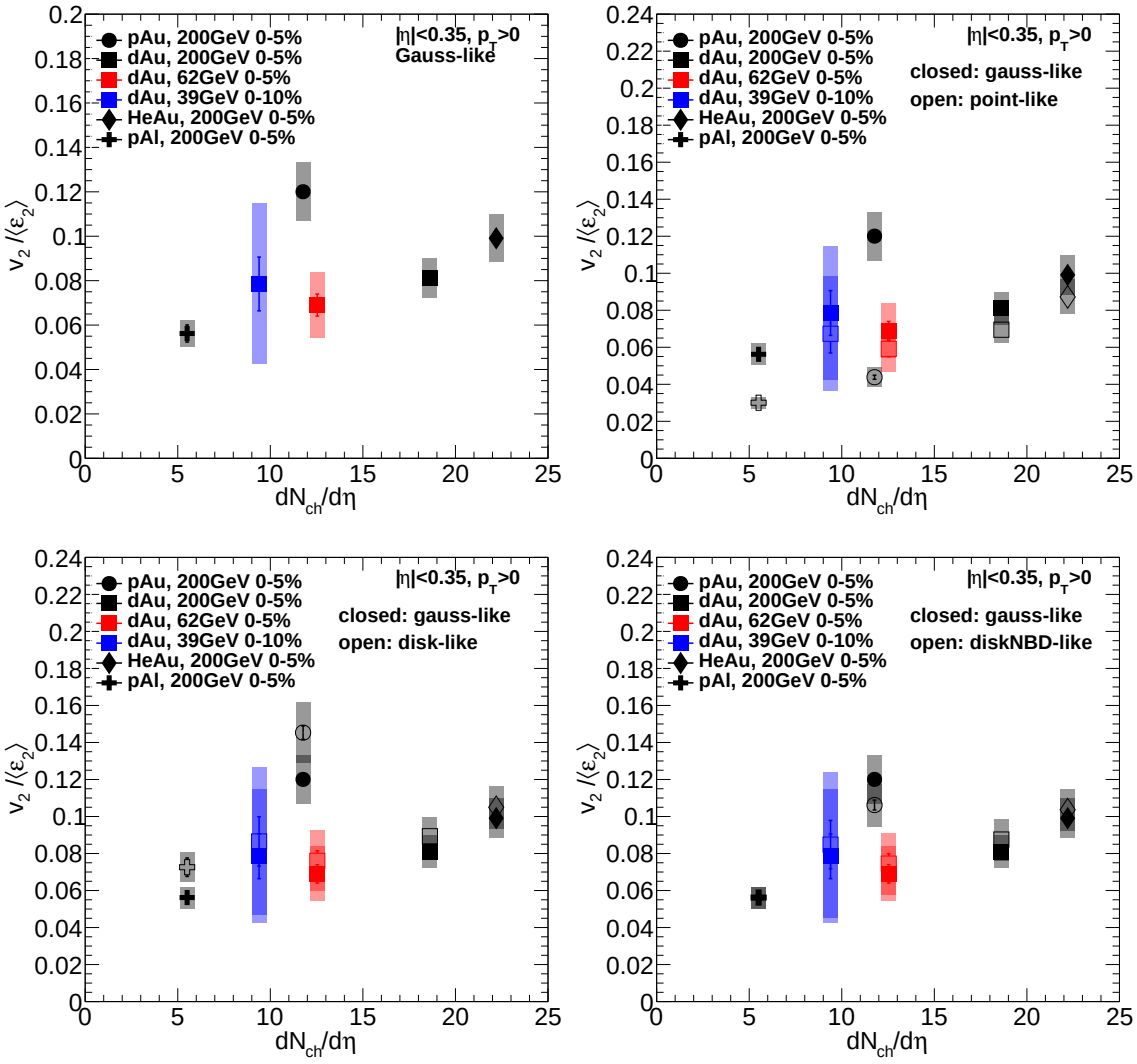

Figure 7.6: Measured $v_2/\langle\varepsilon_2\rangle(dN_{ch}/d\eta)$ in small systems. Each panel shows the points with Gauss-like geometry parameters in closed points. Panels with open points show how the distribution changes if the calculation assumes the nucleons are point-like (top right), disk-like (bottom left), or diskNBD-like (bottom right).

sion systems of varying sizes, all with $\sqrt{s_{NN}}$ = 200 GeV. As a result of the availability of published data, the centrality bins are not identical, with the A+A collisions having wider bins. Third harmonic measurements in these systems are only weakly dependent on centrality [8]. Even without any scaling, there is some overlap between the direct measurement of v_3 in small and large systems.

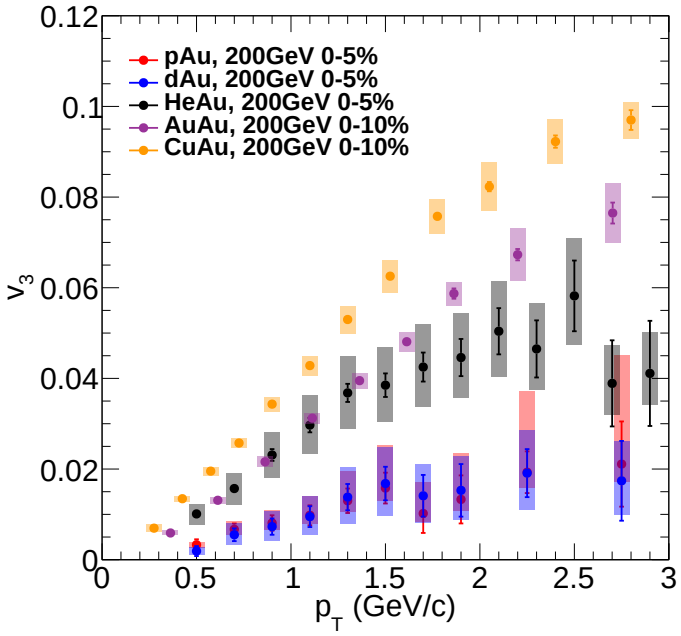

Figure 7.7: Measured $v_3(p_T)$ in $p/d/^3$He+Au, Au+Au, and Cu+Au collisions at $\sqrt{s_{NN}}$ = 200 GeV.

The first type of scaling which is applied is the same linear eccentricity scaling as was used for the second harmonic. As shown in Figure 7.8 (left), scaling by only eccentricity results in the data roughly clustering into two bands: an upper band of large systems and a lower band of small systems. This matches the expectation that linear geometry scaling is not enough to account for differences in the measured v_3 between different systems, and it suggests a system-size dependent effect. A second type of scaling is shown in Figure 7.8 (right) in which v_2 is scaled by $\sqrt[3]{\langle N_{part}\rangle}$. The cubed root of the number of participants, $\sqrt[3]{\langle N_{part}\rangle}$, is used because it is proportional to the transverse particle density. This scaling causes the ordering to change such that the intrinsically triangular systems moving to the top, but the systematic uncertainties are quite large, so it is hard to say anything conclusive from this.

When both scaling relationships are applied together, shown in Figure 7.9, the data still appear to have some multiplicity separation with the Au+Au and Cu+Au data remaining systematically above the $p/d/^3$He+Au data. Because these are very simple scaling rela-

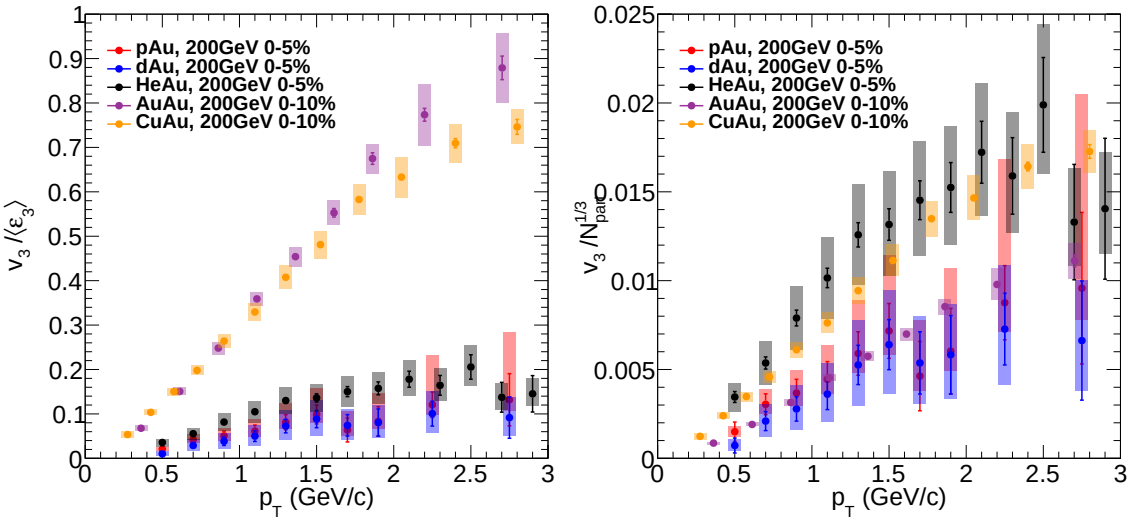

Figure 7.8: Measured $v_3/\langle\varepsilon_3\rangle(p_T)$ and $v_3/\sqrt[3]{\langle N_{part}\rangle}$ in $p/d/^3$He+Au, Au+Au, and Cu+Au collisions at $\sqrt{s_{NN}}$ = 200 GeV.

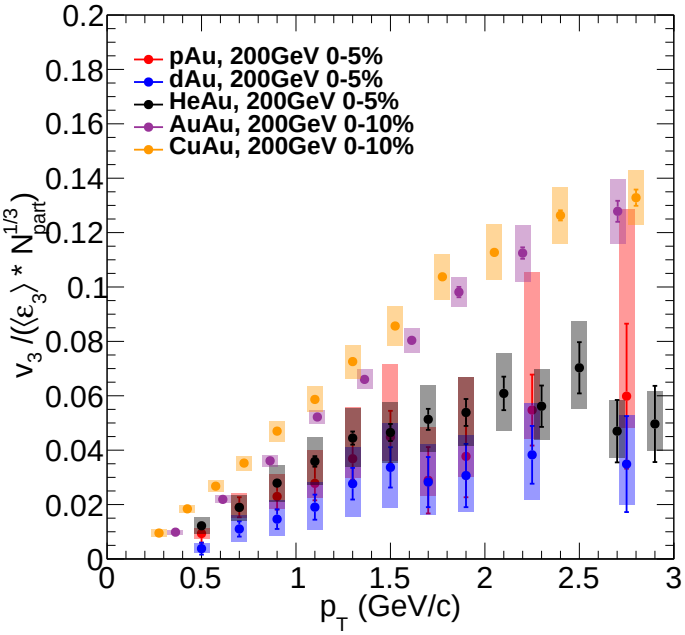

Figure 7.9: Measured $v_3/(\langle\varepsilon_3\rangle\sqrt[3]{\langle N_{part}\rangle})(p_T)$ in $p/d/^3$He+Au, Au+Au, and Cu+Au collisions at $\sqrt{s_{NN}}$ = 200 GeV.

tionships, it is not entirely surprising that this does not produce a universal curve for all systems. Further analysis of these types of scaling relationships in small systems could be insightful.

	p+Au	d+Au	^{3}He+Au	p+Al	Au+Au	Cu+Au
$\langle\varepsilon_2\rangle$ (Gauss-like)	0.23 ± 0.01	0.54 ± 0.04	0.5 ± 0.02	0.31 ± 0.01		
$\langle\varepsilon_2\rangle$ (point-like)	0.63 ± 0.04	0.63 ± 0.04	0.568 ± 0.022	0.58 ± 0.02	0.103 ± 0.003	0.138 ± 0.011
$\langle\varepsilon_2\rangle$ (disk-like)	0.19 ± 0.01	0.49 ± 0.04	0.472 ± 0.02	0.24 ± 0.01		
$\langle\varepsilon_2\rangle$ (diskNBD-like)	0.26 ± 0.01	0.5 ± 0.05	0.478 ± 0.019	0.31 ± 0.01		
$\langle\varepsilon_3\rangle$ (Gauss-like)	0.16 ± 0.01	0.19 ± 0.01	0.283 ± 0.024	0.17 ± 0.01		
$\langle\varepsilon_3\rangle$ (point-like)	0.35 ± 0.01	0.26 ± 0.02	0.349 ± 0.024	0.48 ± 0.03	0.087 ± 0.002	0.13 ± 0.004
$\langle N_{part}\rangle$	10.7 ± 0.6	18.1 ± 1.2	25.043 ± 1.579	5.1 ± 0.3	325.2 ± 3.3	177.2 ± 5.2

Table 7.1: Summary of MC-Glauber geometry calculations utilized in the comparisons discussed in this chapter. All calculations are for $\sqrt{s_{NN}}$ = 200 GeV. The calculations for $p/d/^3$He+Au and p+Al were performed for 0-5% centrality [7], and the calculations for Au+Au and Cu+Au were performed for 0-10% centrality [8].

Chapter 8

Conclusion

In summary, azimuthal particle correlations have been shown for three small collision systems with different intrinsic initial geometries. The simultaneous constraints of v_2 and v_3 in $p/d/^3$He+Au collisions definitively demonstrates that the v_n values are correlated to the initial geometry, removing any ambiguity related to event multiplicity or the concrete implementations in various initial geometry models. The ordering of the $v_2(p_T)$ and $v_3(p_T)$ measurements between the three collision systems is inconsistent with that expected from initial-state momentum correlation models, ruling this out as the dominant mechanism behind the observed collectivity. Hydrodynamical models, which include quark-gluon plasma formation, were found to provide a simultaneous and quantitative description of the data in all three systems.

Studies from both theory and experiment could be done in the future to expand on these results. The ongoing exploration of characterizing the initial state is important to understanding the system as a whole, both in the form of more constrained initial state models and in the development of the methods of calculating geometry parameters within initial state models. A promising frontier in this realm are models that are not nucleon-based but parton-based, a consideration which one might expect is increasingly important as the size of the system decreases.

The small collision system data shown here were all collected using the PHENIX detector, which has some coverage and efficiency limitations. Analyses utilizing the recently installed event-plane detector at the STAR experiment could be performed as a cross check.

The conclusion that quark-gluon plasma was being produced in large systems was supported by the combined evidence from many observables. A more complete picture of the

medium produced in small systems will rely on the ongoing analysis of a broad range of observables.

This dissertation has presented results from small collision systems which are consistent with a hydrodynamic description, providing the most conclusive and comprehensive evidence to date that the collectivity, which occurs in a subset of small-system nuclear collisions, is the direct result of quark-gluon plasma production.

Appendix A

Additional Materials from the Statistical Analysis

A.1 Minimization of $\tilde{\chi}^2$ for Individual Harmonics

Figure A.1 shows how the v_2 data points from p+Au collisions and model calculations are shifted to become closer together with the parameter set that minimizes $\tilde{\chi}^2$. Unlike the results presented in Section 6.5, which shows combined minimization, this minimization is independent of v_3. Comparing the $\tilde{\chi}^2$ values yielded in this minimization to those which were yielded for combined minimization highlights which models are most affected by the correlation that was enforced in the combined minimization process. Appendix A.2 has tables that detail all of these values for both individual and combined minimization. Figures A.2 and A.3 show individual minimization for v_2 in d+Au and ^{3}He+Au collisions, and Figures A.4 to A.6 show individual minimization for v_3 in $p/d/^3$He+Au collisions.

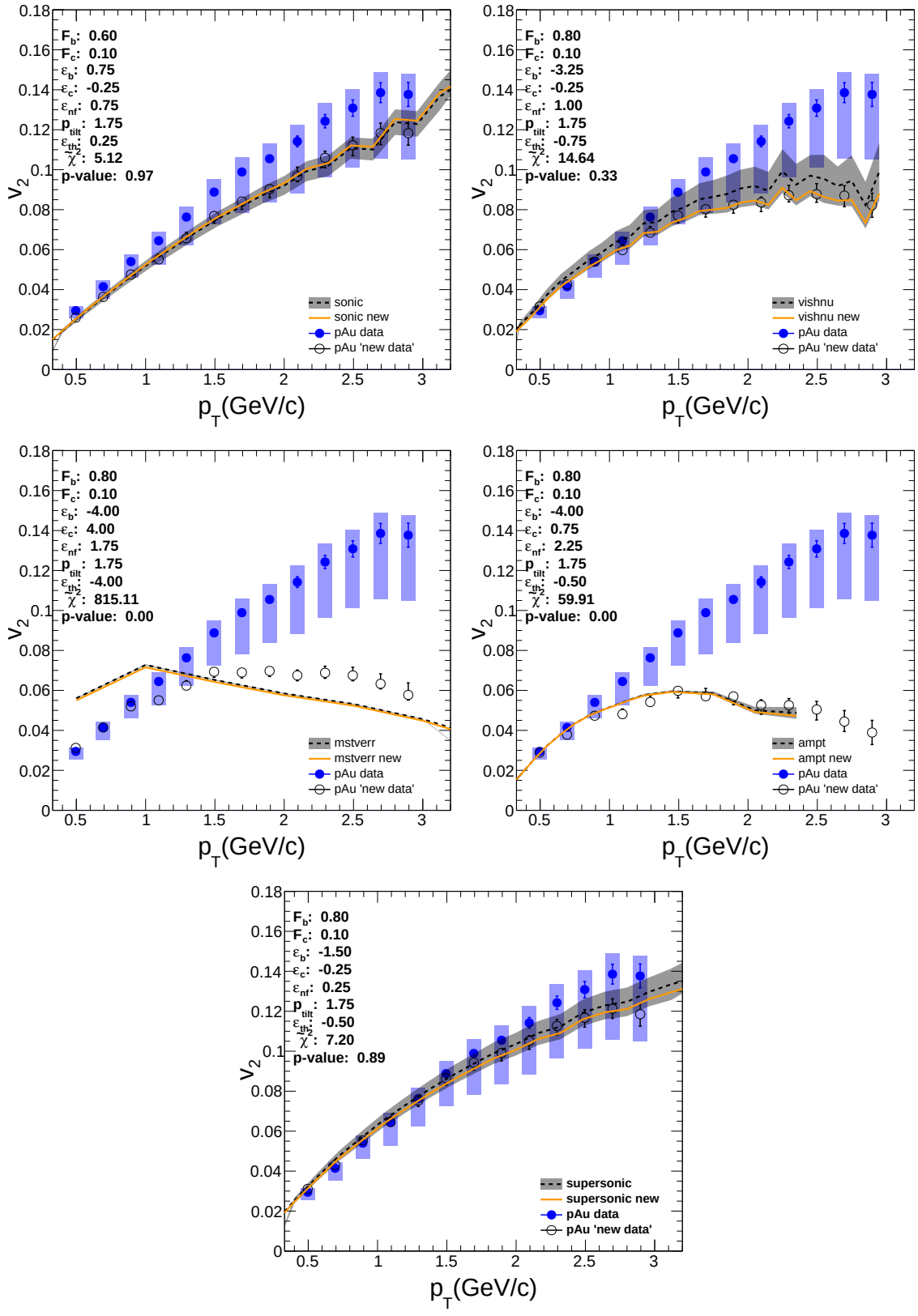

Figure A.1: Measurements and calculations of $v_2(p_T)$ in p+Au collisions before and after $\tilde{\chi}^2$ minimization.

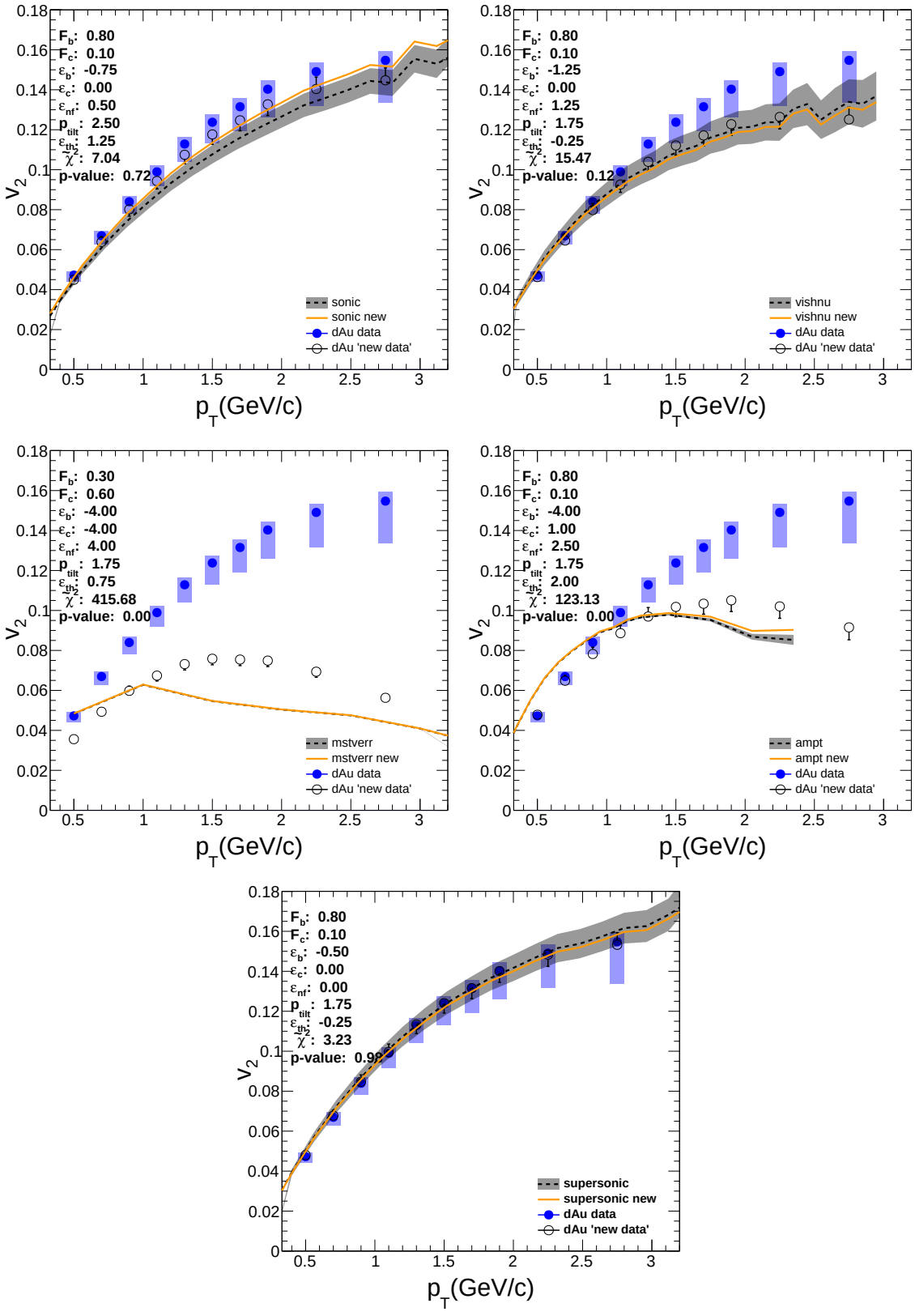

Figure A.2: Measurements and calculations of $v_2(p_T)$ in d+Au collisions before and after $\tilde{\chi}^2$ minimization.

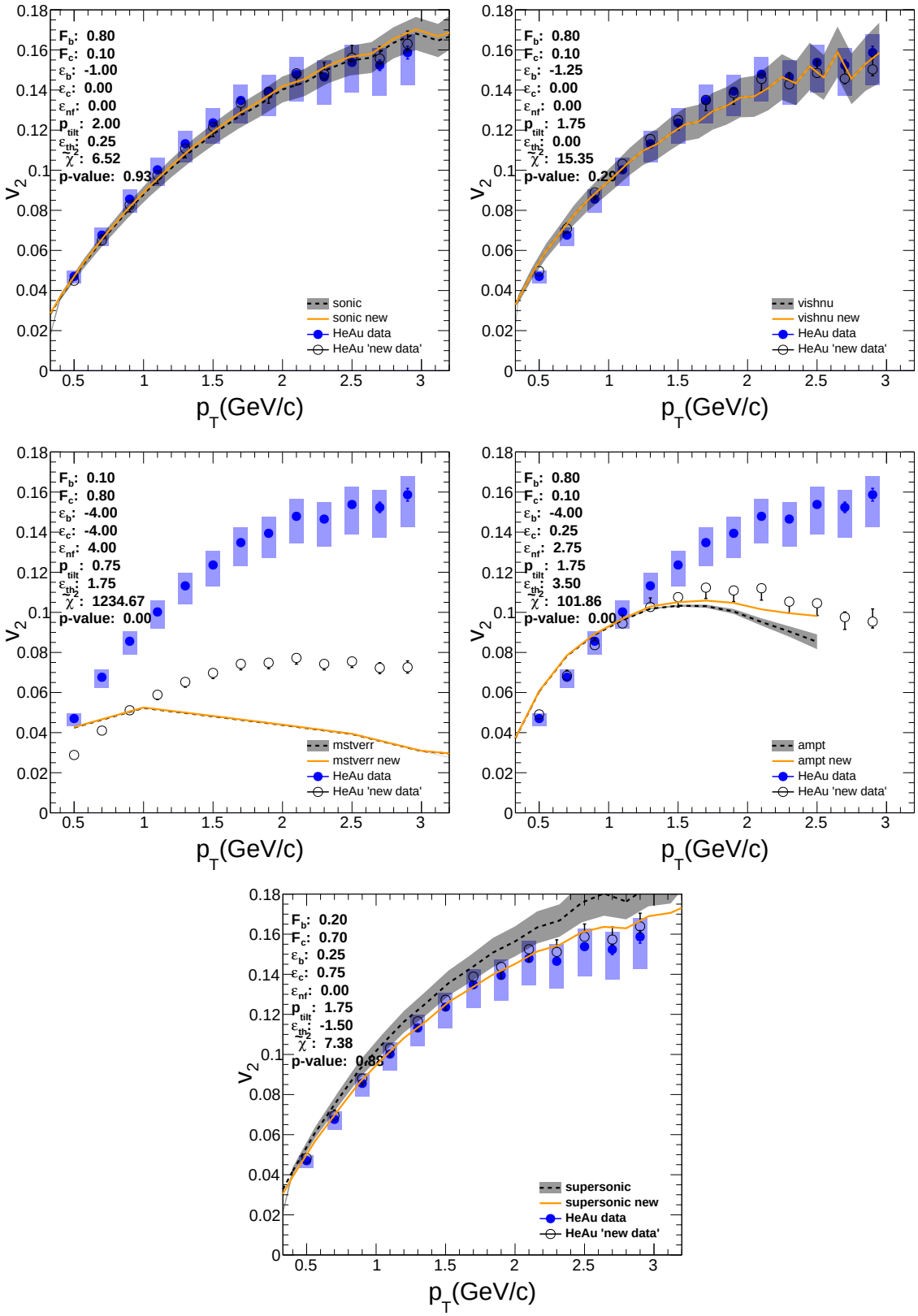

Figure A.3: Measurements and calculations of $v_2(p_T)$ in ^{3}He+Au collisions before and after $\tilde{\chi}^2$ minimization.

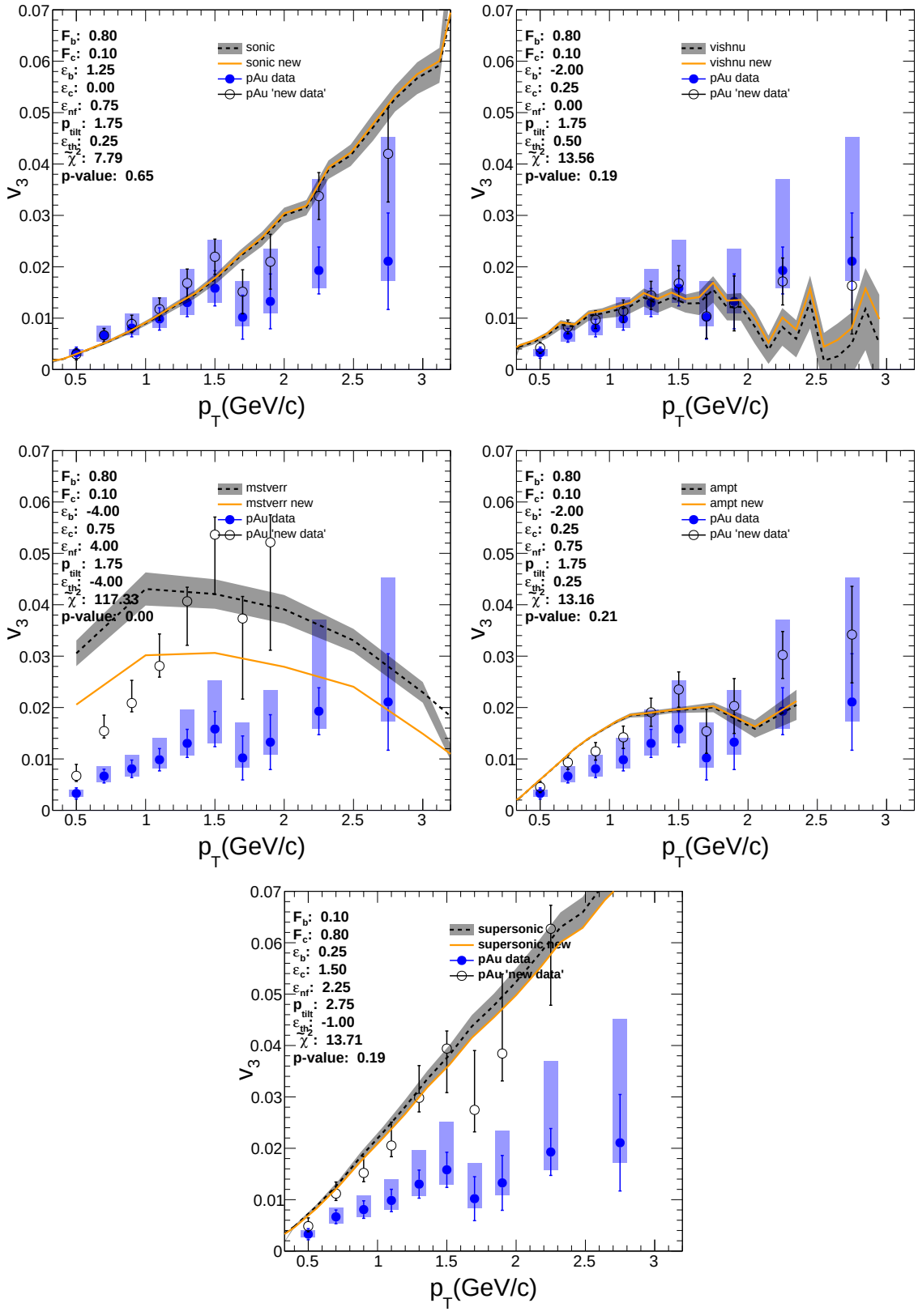

Figure A.4: Measurements and calculations of $v_3(p_T)$ in p+Au collisions before and after $\tilde{\chi}^2$ minimization.

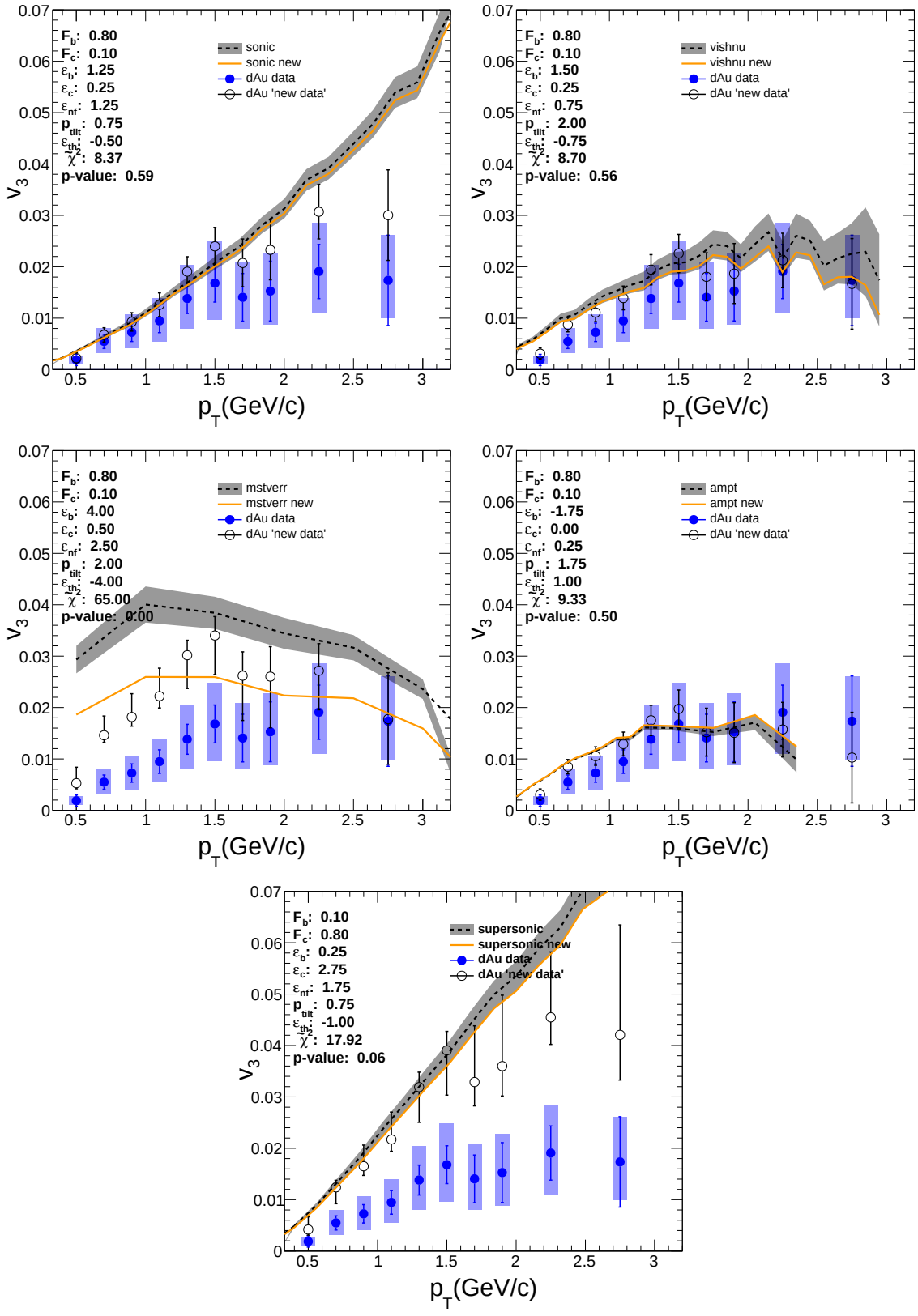

Figure A.5: Measurements and calculations of $v_3(p_T)$ in d+Au collisions before and after $\tilde{\chi}^2$ minimization.

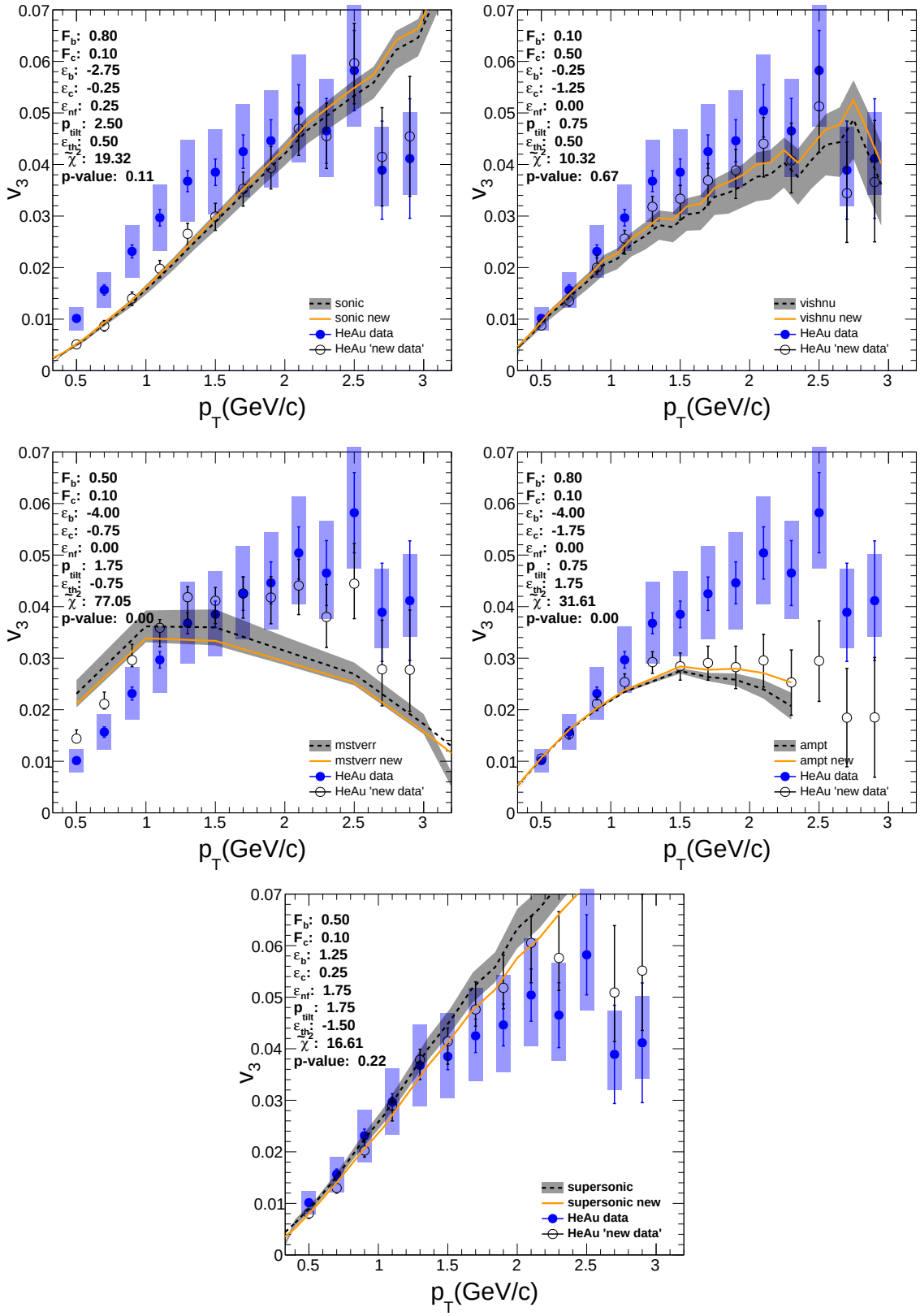

Figure A.6: Measurements and calculations of $v_3(p_T)$ in ^{3}He+Au collisions before and after $\tilde{\chi}^2$ minimization.

A.2 Parameter Tables Associated with $\tilde{\chi}^2$ Minimization

Taking a closer look at the specific values of the parameters that minimized $\tilde{\chi}^2$ can offer insight into how this specific choice of statistical analysis functions. First consider the top section of Table A.1 that shows parameters associated with the $\tilde{\chi}^2$ minimization of v_2 and v_3 data in p+Au collisions compared to the model SONIC. The values of ε_{nf} and ε_{th} which are associated with the individual minimization are 0.75 and 0.25, respectively, for both v_2 and v_3. As such, the correlations enforced in combined minimization are already achieved and all parameters associated with combined minimization are identical to those that achieved individual minimization. This is the only case in which the sum of the minimized $\tilde{\chi}^2$ for individual v_2 (5.12) and individual v_3 (7.79) minimization to be greater than the minimized $\tilde{\chi}^2$ for combined v_2 and v_3 (12.28), because everything is identical except that the penalties associated with ε_{nf} and ε_{th} were only added once in the combined case, whereas they were added once for each individual case, and therefore were added twice to the sum of the two individual cases. For all other results presented in these tables, ε_{nf} and/or ε_{th} differ in the individual minimization case, which means that the parameters associated with combined minimization must change for one or both harmonics. By definition, this means that the $\tilde{\chi}^2$ associated with that harmonic at minimization is larger than the value for individual minimization.

Compared to SONIC calculations												
System	Harmonic	Min $\tilde{\chi}^2$	NDF	p-value	F_a	F_b	F_c	p_{tilt}	ε_b	ε_c	ε_{nf}	ε_{th}
p+Au	v_2	5.12142	13	0.972422	0.3	0.6	0.1	1.75	0.75	-0.25	0.75	0.25
p+Au	v_3	7.78567	10	0.649763	0.1	0.8	0.1	1.75	1.25	0	0.75	0.25
p+Au	v_2&v_3	12.2821	23	0.965885								
	(associated v_2 pars)				0.3	0.6	0.1	1.75	0.75	-0.25	0.75	0.25
	(associated v_3 pars)				0.1	0.8	0.1	1.75	1.25	0	0.75	0.25
d+Au	v_2	7.03912	10	0.721747	0.1	0.8	0.1	2.5	-0.75	0	0.5	1.25
d+Au	v_3	8.37211	10	0.592539	0.1	0.8	0.1	0.75	1.25	0.25	1.25	-0.5
d+Au	v_2&v_3	16.44	20	0.688982								
	(associated v_2 pars)				0.1	0.8	0.1	1.75	1	0	1	0.25
	(associated v_3 pars)				0.4	0.1	0.5	1.75	0.25	1.25	1	0.25
^{3}He+Au	v_2	6.51958	13	0.925186	0.1	0.8	0.1	2	-1	0	0	0.25
^{3}He+Au	v_3	19.3182	13	0.113562	0.1	0.8	0.1	2.5	-2.75	-0.25	0.25	0.5
^{3}He+Au	v_2&v_3	25.965	26	0.465029								
	(associated v_2 pars)				0.1	0.8	0.1	2	-1	0	0	0.25
	(associated v_3 pars)				0.1	0.8	0.1	2.5	-2.75	-0.5	0	0.25
Combined	v_2	18.6801	36	0.992393								
Combined	v_3	35.476	33	0.352289								
Combined	v_2&v_3	54.6871	69	0.895578								

Table A.1: Minimized $\tilde{\chi}^2$ for v_2 and v_3 (independent & combined). This is the comparison to sonic and minimized over a granularity of 0.25 for ε_b and ε_c; 0.25 for ε_{nf}; 0.25 for ε_{th}; 0.1 for F_a, F_b, and F_c; and 0.25 for p_{tilt}.

Compared to superSONIC **calculations**												
System	Harmonic	Min $\tilde{\chi}^2$	NDF	p-value	F_a	F_b	F_c	p_{tilt}	ε_b	ε_c	ε_{nf}	ε_{th}
p+Au	v_2	7.20118	13	0.891488	0.1	0.8	0.1	1.75	-1.5	-0.25	0.25	-0.5
p+Au	v_3	13.7134	10	0.18647	0.1	0.1	0.8	2.75	0.25	1.5	2.25	-1
p+Au	v_2&v_3	27.3151	23	0.242792								
	(associated v_2 pars)				0.1	0.1	0.8	2.25	0.25	1.75	1.5	-2.75
	(associated v_3 pars)				0.1	0.1	0.8	2.75	0.25	2	1.5	-2.75
d+Au	v_2	3.22541	10	0.975611	0.1	0.8	0.1	1.75	-0.5	0	0	-0.25
d+Au	v_3	17.9247	10	0.0562477	0.1	0.1	0.8	0.75	0.25	2.75	1.75	-1
d+Au	v_2&v_3	23.5539	20	0.262422								
	(associated v_2 pars)				0.1	0.8	0.1	1.25	0.25	0	0.75	-1.75
	(associated v_3 pars)				0.1	0.1	0.8	0.75	0.25	3	0.75	-1.75
^{3}He+Au	v_2	7.37809	13	0.881631	0.1	0.2	0.7	1.75	0.25	0.75	0	-1.5
^{3}He+Au	v_3	16.6147	13	0.217522	0.4	0.5	0.1	1.75	1.25	0.25	1.75	-1.5
^{3}He+Au	v_2&v_3	24.469	26	0.549166								
	(associated v_2 pars)				0.1	0.8	0.1	1	0.25	0	0.25	-2.25
	(associated v_3 pars)				0.1	0.8	0.1	1.5	2	0	0.25	-2.25
Combined	v_2	17.8047	36	0.995222								
Combined	v_3	48.2528	33	0.0420836								
Combined	v_2&v_3	75.338	69	0.280886								

Table A.2: Minimized $\tilde{\chi}^2$ for v_2 and v_3 (independent & combined). This is the comparison to superSONIC and minimized over a granularity of 0.25 for ε_b and ε_c; 0.25 for ε_{nf}; 0.25 for ε_{th}; 0.1 for F_a, F_b, and F_c; and 0.25 for p_{tilt}.

Compared to iEBE-VISHNU calculations												
System	Harmonic	Min $\tilde{\chi}^2$	NDF	p-value	F_a	F_b	F_c	p_{tilt}	ε_b	ε_c	ε_{nf}	ε_{th}
p+Au	v_2	14.6391	13	0.330423	0.1	0.8	0.1	1.75	-3.25	-0.25	1	-0.75
p+Au	v_3	13.5592	10	0.194064	0.1	0.8	0.1	1.75	-2	0.25	0	0.5
p+Au	v_2&v_3	32.7107	23	0.0862416								
	(associated v_2 pars)				0.1	0.8	0.1	1.75	-3.75	0.25	0.25	1
	(associated v_3 pars)				0.1	0.8	0.1	1.75	-1.75	0.25	0.25	1
d+Au	v_2	15.4686	10	0.115889	0.1	0.8	0.1	1.75	-1.25	0	1.25	-0.25
d+Au	v_3	8.70257	10	0.560545	0.1	0.8	0.1	2	1.5	0.25	0.75	-0.75
d+Au	v_2&v_3	22.5173	20	0.313111								
	(associated v_2 pars)				0.1	0.8	0.1	1.75	-1.25	0	1.5	-0.5
	(associated v_3 pars)				0.1	0.8	0.1	1.75	-1.5	0	1.5	-0.5
^{3}He+Au	v_2	15.3483	13	0.286118	0.1	0.8	0.1	1.75	-1.25	0	0	0
^{3}He+Au	v_3	10.3161	13	0.667907	0.4	0.1	0.5	0.75	-0.25	-1.25	0	0.5
^{3}He+Au	v_2&v_3	26.5785	26	0.431687								
	(associated v_2 pars)				0.1	0.8	0.1	1.75	-1.25	0	0	0
	(associated v_3 pars)				0.4	0.1	0.5	1.75	-0.25	-1.75	0	0
Combined	v_2	45.4559	36	0.134238								
Combined	v_3	32.5778	33	0.488005								
Combined	v_2&v_3	81.8065	69	0.138927								

Table A.3: Minimized $\tilde{\chi}^2$ for v_2 and v_3 (independent & combined). This is the comparison to iEBE-VISHNU and minimized over a granularity of 0.25 for ε_b and ε_c; 0.25 for ε_{nf}; 0.25 for ε_{th}; 0.1 for F_a, F_b, and F_c; and 0.25 for p_{tilt}.

Compared to AMPT calculations												
System	Harmonic	Min $\tilde{\chi}^2$	NDF	p-value	F_a	F_b	F_c	p_{tilt}	ε_b	ε_c	ε_{nf}	ε_{th}
p+Au	v_2	59.906	13	5.46076e-08	0.1	0.8	0.1	1.75	-4	0.75	2.25	-0.5
p+Au	v_3	13.1586	10	0.214938	0.1	0.8	0.1	1.75	-2	0.25	0.75	0.25
p+Au	v_2&v_3	74.8922	23	2.08848e-07								
	(associated v_2 pars)				0.1	0.8	0.1	1.75	-3.5	-0.25	2	1.75
	(associated v_3 pars)				0.4	0.5	0.1	1.75	-0.75	0	2	1.75
d+Au	v_2	123.126	10	1.17311e-21	0.1	0.8	0.1	1.75	-4	1	2.5	2
d+Au	v_3	9.3338	10	0.500745	0.1	0.8	0.1	1.75	-1.75	0	0.25	1
d+Au	v_2&v_3	132.091	20	1.57774e-18								
	(associated v_2 pars)				0.1	0.8	0.1	1.75	-4	0.75	2.25	3.25
	(associated v_3 pars)				0.4	0.5	0.1	1.75	-1	0	2.25	3.25
^{3}He+Au	v_2	101.862	13	7.22277e-16	0.1	0.8	0.1	1.75	-4	0.25	2.75	3.5
^{3}He+Au	v_3	31.608	13	0.00274516	0.1	0.8	0.1	0.75	-4	-1.75	0	1.75
^{3}He+Au	v_2&v_3	166.946	26	1.55839e-22								
	(associated v_2 pars)				0.1	0.8	0.1	1.75	-4	-1	2.25	4
	(associated v_3 pars)				0.1	0.8	0.1	0.75	-4	-2	2.25	4
Combined	v_2	284.893	36	1.78622e-40								
Combined	v_3	54.1004	33	0.0117099								
Combined	v_2&v_3	373.93	69	1.94274e-43								

Table A.4: Minimized $\tilde{\chi}^2$ for v_2 and v_3 (independent & combined). This is the comparison to AMPT and minimized over a granularity of 0.25 for ε_b and ε_c; 0.25 for ε_{nf}; 0.25 for ε_{th}; 0.1 for F_a, F_b, and F_c; and 0.25 for p_{tilt}.

Compared to MSTV, PRL Erratum calculations												
System	Harmonic	Min $\tilde{\chi}^2$	NDF	p-value	F_a	F_b	F_c	p_{tilt}	ε_b	ε_c	ε_{nf}	ε_{th}
p+Au	v_2	815.1	13	8.006e-166	0.1	0.8	0.1	1.75	-4	4	1.75	-4
p+Au	v_3	117.3	10	1.758e-20	0.1	0.8	0.1	1.75	-4	0.75	4	-4
p+Au	v_2&v_3	930.4	23	8.331e-182								
	(associated v_2 pars)				0.1	0.8	0.1	1.75	-4	4	1.75	-4
	(associated v_3 pars)				0.1	0.1	0.8	2.75	1.25	4	1.75	-4
d+Au	v_2	415.7	10	4.311e-83	0.1	0.3	0.6	1.75	-4	-4	4	0.75
d+Au	v_3	65	10	4.057e-10	0.1	0.8	0.1	2	4	0.5	2.5	-4
d+Au	v_2&v_3	474.6	20	6.11e-88								
	(associated v_2 pars)				0.1	0.5	0.4	0.75	-4	-4	4	-3.75
	(associated v_3 pars)				0.1	0.8	0.1	1.75	-4	0.25	4	-3.75
^{3}He+Au	v_2	1235	13	6.135e-256	0.1	0.1	0.8	0.75	-4	-4	4	1.75
^{3}He+Au	v_3	77.05	13	3.946e-11	0.4	0.5	0.1	1.75	-4	-0.75	0	-0.75
^{3}He+Au	v_2&v_3	1408	26	6.419e-281								
	(associated v_2 pars)				0.1	0.1	0.8	0.75	-4	-4	4	-0.75
	(associated v_3 pars)				0.4	0.5	0.1	1.75	-4	0.25	4	-0.75
Combined	v_2	2465	36	0								
Combined	v_3	259.4	33	5.836e-37								
Combined	v_2&v_3	2813	69	0								

Table A.5: Minimized $\tilde{\chi}^2$ for v_2 and v_3 (independent & combined). This is the comparison to MSTV, PRL Erratum and minimized over a granularity of 0.25 for ε_b and ε_c; 0.25 for ε_{nf}; 0.25 for ε_{th}; 0.1 for F_a, F_b, and F_c; and 0.25 for p_{tilt}.

BIBLIOGRAPHY

[1] C. Patrignani et al. Review of Particle Physics. *Chin. Phys.*, C40(10):100001, 2016.

[2] A. Adare et al. Measurements of elliptic and triangular flow in high-multiplicity ^{3}He+Au collisions at $\sqrt{s_{NN}} = 200$ GeV. *Phys. Rev. Lett.*, 115(14):142301, 2015.

[3] C. Aidala et al. Measurement of long-range angular correlations and azimuthal anisotropies in high-multiplicity p+Au collisions at $\sqrt{s_{NN}} = 200$ GeV. *Phys. Rev. C*, 95(3):034910, 2017.

[4] A. Adare et al. Measurement of long-range angular correlation and quadrupole anisotropy of pions and (anti)protons in central d+Au collisions at $\sqrt{s_{NN}}$=200 GeV. *Phys. Rev. Lett.*, 114(19):192301, 2015.

[5] C. Aidala et al. Measurements of azimuthal anisotropy and charged-particle multiplicity in d+Au collisions at $\sqrt{s_{NN}}$ =200, 62.4, 39, and 19.6 GeV. *Phys. Rev. C*, 96(6):064905, 2017.

[6] C. Aidala et al. Creation of quark–gluon plasma droplets with three distinct geometries. *Nature Phys.*, 15(3):214–220, 2019.

[7] A. Adare et al. Centrality categorization for $R_{p(d)+A}$ in high-energy collisions. *Phys. Rev. C*, 90(3):034902, 2014.

[8] A. Adare et al. Measurements of directed, elliptic, and triangular flow in Cu+Au collisions at $\sqrt{s_{NN}} = 200$ GeV. *Phys. Rev.*, C94(5):054910, 2016.

[9] Christian Schmidt and Sayantan Sharma. The phase structure of QCD. *J. Phys.*, G44(10):104002, 2017.

[10] Francois Gelis and Bjoern Schenke. Initial State Quantum Fluctuations in the Little Bang. *Ann. Rev. Nucl. Part. Sci.*, 66:73–94, 2016.

[11] Serguei Chatrchyan et al. Measurement of the elliptic anisotropy of charged particles produced in PbPb collisions at $\sqrt{s}_{NN}$=2.76 TeV. *Phys. Rev.*, C87(1):014902, 2013.

[12] B. Alver et al. Importance of correlations and fluctuations on the initial source eccentricity in high-energy nucleus-nucleus collisions. *Phys. Rev.*, C77:014906, 2008.

[13] B. Alver and G. Roland. Collision geometry fluctuations and triangular flow in heavy-ion collisions. *Phys. Rev.*, C81:054905, 2010. [Erratum: Phys. Rev.C82,039903(2010)].

[14] Mark Mace, Vladimir V. Skokov, Prithwish Tribedy, and Raju Venugopalan. Hierarchy of azimuthal anisotropy harmonics in collisions of small systems from the Color Glass Condensate. *Phys. Rev. Lett.*, 121(5):052301, 2018. [Erratum: Phys. Rev. Lett.123,no.3,039901(2019)].

[15] A. Adare et al. Pseudorapidity Dependence of Particle Production and Elliptic Flow in Asymmetric Nuclear Collisions of p+Al, p+Au, d+Au, and ^{3}He+Au at $\sqrt{s_{NN}} = 200$ GeV. *Phys. Rev. Lett.*, 121(22):222301, 2018.

[16] R. Hagedorn. Statistical thermodynamics of strong interactions at high-energies. *Nuovo Cim. Suppl.*, 3:147–186, 1965.

[17] John C. Collins and M. J. Perry. Superdense Matter: Neutrons Or Asymptotically Free Quarks? *Phys. Rev. Lett.*, 34:1353, 1975.

[18] Charles Gale, Sangyong Jeon, and Bjoern Schenke. Hydrodynamic Modeling of Heavy-Ion Collisions. *Int. J. Mod. Phys.*, A28:1340011, 2013.

[19] M. Habich, J. L. Nagle, and P. Romatschke. Particle spectra and HBT radii for simulated central nuclear collisions of C + C, Al + Al, Cu + Cu, Au + Au, and Pb + Pb from $\sqrt{s} = 62.4$ - 2760 GeV. *Eur. Phys. J. C*, 75(1):15, 2015.

[20] Paul Romatschke. Light-Heavy Ion Collisions: A window into pre-equilibrium QCD dynamics? *Eur. Phys. J.*, C75(7):305, 2015.

[21] Chun Shen, Jean-Franois Paquet, Gabriel S. Denicol, Sangyong Jeon, and Charles Gale. Collectivity and electromagnetic radiation in small systems. *Phys. Rev.*, C95(1):014906, 2017.

[22] Zi-Wei Lin, Che Ming Ko, Bao-An Li, Bin Zhang, and Subrata Pal. A Multi-phase transport model for relativistic heavy ion collisions. *Phys. Rev. C*, 72:064901, 2005.

[23] Itzhak Tserruya. Relativistic heavy ion physics: Experimental overview. *Pramana*, 60:577–592, 2003.

[24] J. D. Bjorken. Highly Relativistic Nucleus-Nucleus Collisions: The Central Rapidity Region. *Phys. Rev.*, D27:140–151, 1983.

[25] Vardan Khachatryan et al. Observation of Long-Range Near-Side Angular Correlations in Proton-Proton Collisions at the LHC. *JHEP*, 09:091, 2010.

[26] Betty Abelev et al. Long-range angular correlations on the near and away side in p-Pb collisions at $\sqrt{s_{NN}} = 5.02$ TeV. *Phys. Lett.*, B719:29–41, 2013.

[27] Serguei Chatrchyan et al. Observation of long-range near-side angular correlations in proton-lead collisions at the LHC. *Phys. Lett.*, B718:795–814, 2013.

[28] Georges Aad et al. Observation of Associated Near-Side and Away-Side Long-Range Correlations in $\sqrt{s_{NN}}$=5.02TeV Proton-Lead Collisions with the ATLAS Detector. *Phys. Rev. Lett.*, 110(18):182302, 2013.

[29] Serguei Chatrchyan et al. Multiplicity and Transverse Momentum Dependence of Two- and Four-Particle Correlations in pPb and PbPb Collisions. *Phys. Lett.*, B724:213–240, 2013.

[30] Georges Aad et al. Measurement of long-range pseudorapidity correlations and azimuthal harmonics in $\sqrt{s_{NN}} = 5.02$ TeV proton-lead collisions with the ATLAS detector. *Phys. Rev.*, C90(4):044906, 2014.

[31] Betty Bezverkhny Abelev et al. Long-range angular correlations of π, K and p in p-Pb collisions at $\sqrt{s_{\rm NN}}$ = 5.02 TeV. *Phys. Lett.*, B726:164–177, 2013.

[32] A. Adare et al. Quadrupole Anisotropy in Dihadron Azimuthal Correlations in Central d+Au Collisions at $\sqrt{s_{NN}}$=200 GeV. *Phys. Rev. Lett.*, 111(21):212301, 2013.

[33] C. Aidala et al. Measurements of Multiparticle Correlations in $d+$Au Collisions at 200, 62.4, 39, and 19.6 GeV and $p+$Au Collisions at 200 GeV and Implications for Collective Behavior. *Phys. Rev. Lett.*, 120(6):062302, 2018.

[34] A. Adare et al. Measurements of mass-dependent azimuthal anisotropy in central p+Au, d+Au, and ^{3}He+Au collisions at $\sqrt{s_{NN}} = 200$ GeV. *Phys. Rev. C*, 97:064904, 2018.

[35] J. L. Nagle, A. Adare, S. Beckman, T. Koblesky, J. Orjuela Koop, D. McGlinchey, P. Romatschke, J. Carlson, J. E. Lynn, and M. McCumber. Exploiting Intrinsic Triangular Geometry in Relativistic He3+Au Collisions to Disentangle Medium Properties. *Phys. Rev. Lett.*, 113(11):112301, 2014.

[36] K. Adcox et al. PHENIX central arm tracking detectors. *Nucl. Instrum. Meth. A*, 499:489–507, 2003.

[37] C. Aidala et al. The PHENIX Forward Silicon Vertex Detector. *Nucl. Instrum. Meth. A*, 755:44–61, 2014.

[38] K. Adcox et al. PHENIX detector overview. *Nucl. Instrum. Meth. A*, 499:469–479, 2003.

[39] Ulrich Heinz and Raimond Snellings. Collective flow and viscosity in relativistic heavy-ion collisions. *Ann. Rev. Nucl. Part. Sci.*, 63:123–151, 2013.

[40] Arthur M. Poskanzer and S. A. Voloshin. Methods for analyzing anisotropic flow in relativistic nuclear collisions. *Phys. Rev. C*, 58:1671–1678, 1998.

[41] S. Voloshin and Y. Zhang. Flow study in relativistic nuclear collisions by Fourier expansion of Azimuthal particle distributions. *Z. Phys.*, C70:665–672, 1996.

[42] Qiao Xu. *Observation of Collective Behavior in High-Multiplicity Proton-Gold Collisions with PHENIX at RHIC*. PhD thesis, Vanderbilt U., 2018.

[43] Ryan D. Weller and Paul Romatschke. One fluid to rule them all: viscous hydrodynamic description of event-by-event central p+p, p+Pb and Pb+Pb collisions at $\sqrt{s} = 5.02$ TeV. *Phys. Lett.*, B774:351–356, 2017.

[44] P. Kovtun, Dan T. Son, and Andrei O. Starinets. Viscosity in strongly interacting quantum field theories from black hole physics. *Phys. Rev. Lett.*, 94:111601, 2005.

[45] J. L. Nagle and W. A. Zajc. Assessing saturation physics explanations of collectivity in small collision systems with the IP-Jazma model. 2018.

[46] J. D. Orjuela Koop, A. Adare, D. McGlinchey, and J. L. Nagle. Azimuthal anisotropy relative to the participant plane from a multiphase transport model in central p + Au , d + Au , and ^{3}He + Au collisions at $\sqrt{s_{NN}} = 200$ GeV. *Phys. Rev. C*, 92(5):054903, 2015.

[47] R. Brun and F. Rademakers. ROOT: An object oriented data analysis framework. *Nucl. Instrum. Meth.*, A389:81–86, 1997.

[48] Albert M Sirunyan et al. Multiparticle correlation studies in pPb collisions at $\sqrt{s_{\mathrm{NN}}} =$ 8.16 TeV. 2019.